Spectroscopy and Theory of *cis-trans* Isomerization in the S_1 State of Acetylene

by

P. Bryan Changala

Submitted to the Department of Chemistry
in partial fulfillment of the requirements for the degree of

Bachelor of Science in Chemistry and Physics

at the

MASSACHUSETTS INSTITUTE OF TECHNOLOGY

June 2013

ARCHIVES
MASSACHUSETTS INSTITUTE OF TECHNOLOGY
JUL 01 2013
LIBRARIES

© Massachusetts Institute of Technology 2013. All rights reserved.

Author .....
Department of Chemistry
May 10, 2013

Certified by .....
Robert W. Field
Haslam and Dewey Professor of Chemistry
Thesis Supervisor

Accepted by .....
Rick L. Danheiser
A. C. Cope Professor of Chemistry
Undergraduate Officer, Department of Chemistry

Spectroscopy and Theory of *cis-trans* Isomerization in the S_1 State of Acetylene

by

P. Bryan Changala

Submitted to the Department of Chemistry
on May 10, 2013, in partial fulfillment of the
requirements for the degree of
Bachelor of Science in Chemistry and Physics

Abstract

This thesis consists of parallel experimental and theoretical studies of the rovibrational structure and dynamics of the S_1 state of acetylene, C_2H_2. This small molecule is a prototypical system for the study of *cis-trans* isomerization, the barrier to which is moderately low in the S_1 state, presenting the opportunity to achieve a complete understanding of the global rovibrational dynamics of an isomerizing system.

Our analysis of the spectra of *ungerade* vibrational levels in the region 45800-46550 cm^{-1} extends the complete assignment of *trans* vibrational levels to 4300 cm^{-1} above the S_1 electronic origin. These exhaustive assignments have enabled the identification of two new *cis* vibrational states.

Reduced dimension rovibrational variational calculations have been carried out to aid in the characterization of spectroscopic signatures and patterns associated with the isomerization process. Such effects include the decoupling of the vibrational polyads that involve the low-energy bending modes ν_4 and ν_6 and the large cross-anharmonicity of modes ν_3 and ν_6, the combination bands of which follow the isomerization path toward the half-linear transition state. Additionally, we focus on predictions for the K-staggering observed in both *cis* and *trans* levels caused by tunneling through the isomerization barrier. The detailed patterns of these staggerings make possible a direct empirical distinction between different possible isomerization mechanisms.

We also present an empirical model which analyzes the vibrational level structure along the isomerization path. This model enables the direct spectroscopic characterization of the energy of the transition state, the qualitative structure and width of the isomerization barrier, and the curvature of the nuclear potential surface in directions orthogonal to the isomerization path. This type of analysis is generalizable to other systems, potential surfaces of which contain stationary points and thus provides a powerful new tool for studying transition states via frequency domain spectroscopy.

Thesis Supervisor: Robert W. Field
Title: Haslam and Dewey Professor of Chemistry

Acknowledgements

This work is the product of numerous direct and indirect contributions from many people. I would first like to thank my course and research advisor Bob Field, who has provided inexhaustible support and unflinching confidence in me since the day we met. I have accomplished more than otherwise possible for it. I hope I have acquired some of his inspiring enthusiasm for science and infectiously mystical approach to spectroscopy.

My daily lab work has been supervised by Josh Baraban. It has been a privilege working with and learning from him. I could not have asked for a better mentor and coworker. I am extremely grateful for his significant investments of time and energy in training and teaching me. His guidance has made for an extraordinary undergraduate research experience.

It has been a pleasure working with other members of the Field group, including Barratt Park, David Grimes, Yan Zhou, Kirill Kuyanov-Prozument, Rachel Shaver, Monica Ciuba, Professor John Muenter, Dr. Steve Coy, and, more recently, Jun Jiang and Peter Richter. I'm especially grateful to Tony Colombo for lessons learned. My fellow UROPs, Julia Berk and Ethan Klein, have provided a welcome dose of undergraduate camaraderie during my last year in the Field group.

This reseach would not have been possible without substantial collaborations with Professor Anthony Merer (UBC/IAMS)–a spectroscopist extraordinaire, as well as with Professor John Stanton (UT Austin) and Dr. Jon Hougen (NIST). I would also like to acknowledge support from the MIT Undergraduate Research Opportunities Program and project funding from the DOE.

Lastly, I thank my parents and family for their constant support, both personally and scholarly.

Contents

List of Figures

List of Tables

Chapter 1

Introduction

The power of small molecule spectroscopy is the ability to form a complete physical understanding of a fundamental chemical system. We can only do so, however, by attempting to solve the ultimate inverse problem. The central entities of interest, potential energy surfaces, dictate all chemical phenomena. Transitions between their eigenstates determine the observable spectra. Learning about potential surfaces requires deciphering spectra by finding order that, broadly speaking, reduces meaningless line lists into physical and chemical insight. This task of reverse engineering contains two chief challenges: (i) determining the energy level structure by assigning spectral lines to transitions between eigenstates with known quantum numbers and (ii) inferring as much as possible about the potential energy surface from the structure of the observed energy levels. These two tasks are generally approached by identifying patterns determined by spectroscopic selection rules and simple models that describe an approximate zero-order picture. Often, insight arises from finding where these patterns are broken and characterizing the new order which emerges in their place. This thesis will explore such new insights concerning high energy, large amplitude vibrations, in particular that of *cis-trans* isomerization, in the first excited singlet state (S_1) of acetylene.

1.1 A Brief Spectroscopic History of the S_1 State

Acetylene, C_2H_2, is one of the most extensively studied small polyatomic molecules. The earliest investigations of its UV absorption spectrum were completed a century ago in 1913 [1, 2]. The $\tilde{A}(S_1)$–$\tilde{X}(S_0)$ transition was revisited in the 1930s by several workers [3–7], but remained poorly understood and no significant assignments could be made of the observed bands. Not until the 1950s was a major advance achieved when Innes [8] and Ingold and King [9] independently demonstrated that the S_1 state must be *trans* bent (C_{2h} symmetry) as opposed to possessing the linear ($D_{\infty h}$) geometry of the electronic ground state, S_0. This was the first conclusive example of a qualitative change in equilibrium geometry upon electronic excitation and an early landmark for what would be a fruitful further fifty years of acetylene spectroscopy. An extensive series of absorption experiments carried out by Watson and coworkers [10–12] included detailed rotational analyses of the strongest bands in the $\tilde{A} - \tilde{X}$ system, namely those involving quanta of ν_2' (CC stretch) and ν_3' (*trans* bend) as well as hot bands from ν_4'' (*trans* bend), all which are strongly Franck-Condon active due to the large geometry change of the $\tilde{A} - \tilde{X}$ transition. Due to the shared center-of-symmetry of the linear ground state and the *trans* conformer, these absorption experiments could only investigate *gerade* vibrational modes of the *trans* conformer. In the 1990s, the Crim group performed IR-UV double resonance (DR) experiments with laser-induced fluorescence (LIF) detection, making the first measurements of the *ungerade* fundamental vibrationals of the *trans* conformer [13, 14]. Population-labeled LIF experiments in the Field group [15] resulted in the observation of the ν_1' fundamental, completing the assignment of all six *trans* normal mode fundamentals, a rare accomplishment for an excited electronic state of a polyatomic molecule. These fundamental frequencies are summarized in Figure 1-1.

The vast majority of spectroscopy on the S_1 state has focused on the *trans* conformer, which has ^1A_u electronic symmetry and therefore has electric dipole allowed transitions from the $^1\Sigma_g^+$ ground state. The *cis* conformer has $^1A_2$ symmetry and is thus spectroscopically dark; it can only be observed via tunneling into the *trans* well,

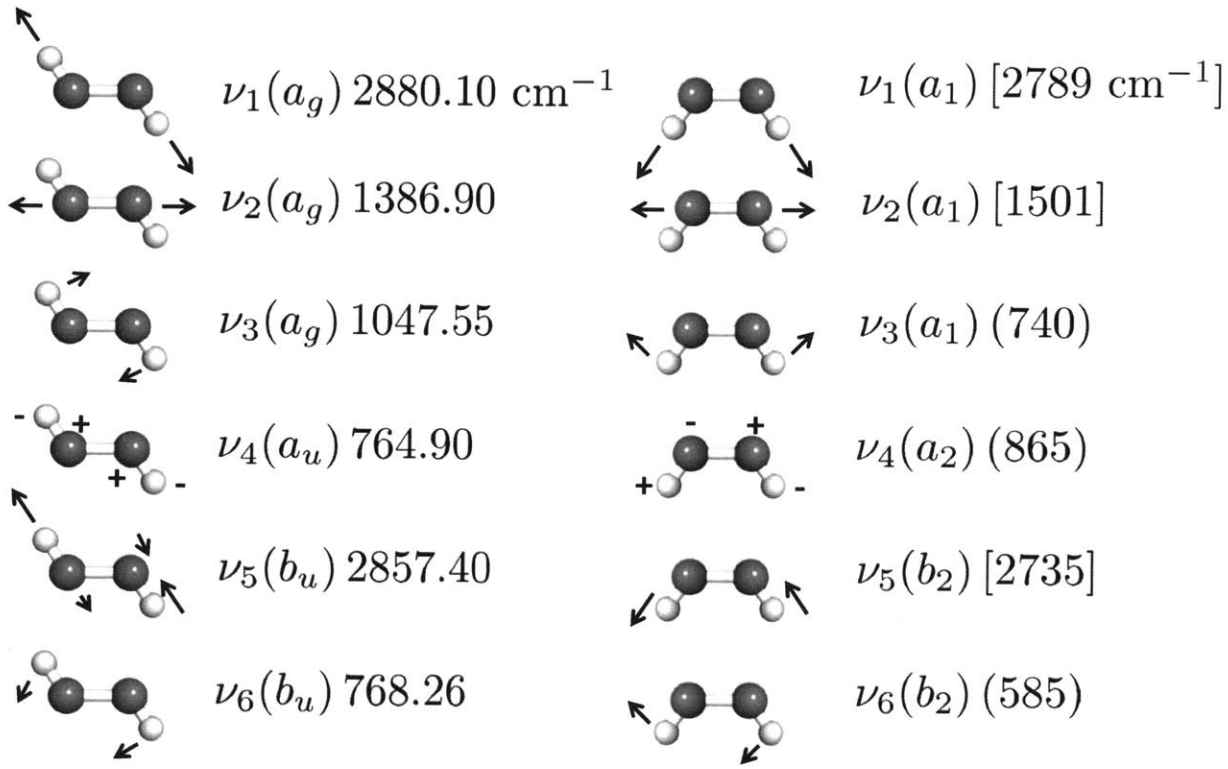

Figure 1-1: Normal modes of *trans* and *cis* S_1 acetylene. All six *trans* fundamental frequencies have been experimentally measured (see [16] and references therein). *cis* frequencies in square brackets are taken from recent *ab initio* VPT2 calculations [16]. Those in parentheses are approximate experimental measurements [17, 18].

thereby picking up some transition dipole. Additional factors, including relatively broad Franck-Condon access due to the large geometry change, have enabled a complete assignment of the *trans* vibrational states up to several thousand cm^{-1} above the *trans* origin (Chapter 2 contains new assignments of *ungerade* vibrational levels up to 4300 cm^{-1} above the *trans* zero-point).

Currently, the single most problematic factor in assigning the *trans* vibrational states is the strong interactions between ν_4 (torsion) and ν_6 (*cis* bend). These near-degenerate modes interact via a 2:2 Darling-Dennison resonance [19] as well as *a*- and *b*-axis Coriolis coupling. The result is a restructuring of the ν_4/ν_6 combination bands and overtones into *polyads*, groups of strongly interacting vibrational levels. An essential feature of polyads is that interaction matrix elements determinable from relatively simple low-energy polyads conform to known scaling and selection rules for higher-lying polyads. Such patterns have made it possible to assign and fit a significant portion of the pure bending overtones [14, 20] and stretch-bend [21] combination levels. Such comprehensive assignments have led to a state where the total absolute number of expected *trans* vibrational levels in particular regions have all been identified, but with the apparent problem that some weakly observed bands remain unaccounted for and without any possibility of being fitted into the *trans* manifold. The resolution to this problem was that these "extra" bands belonged to the first ever identified vibrational states of the *cis* conformer [17]. Reduced dimension DVR calculations [22] justify the nominally forbidden appearance of these bands in the spectra through tunnelling interactions and delocalization into the *trans* well of the potential surface.

1.2 Thesis Outline

This thesis picks up where our story drops off. Our general motivation is to understand the consequences of *cis-trans* isomerization on the spectra of the S_1 state and how we can extract the most fundamental and essential features of the isomerization process by identifying new patterns involved with these large amplitude motions. In

Chapter 2, we present high resolution IR-UV double resonance experiments investigating *ungerade* levels near the energy of the isomerization barrier. Extending the complete assignment of the *trans* level structure allows us to identify new vibrational levels of the *cis* conformer, as well as to track the evolution of the vibrational level structure for states along the isomerization path. In Chapter 3, we include reduced dimension rovibrational variational calculations motivated by the need to understand and predict the drastic qualitative changes in the rovibrational structure of vibrational states as they approach the barrier to isomerization. Such states have not only energies near that of the barrier, but also wavefunctions with considerable amplitude near the transition state. In Chapter 4, we consider an empirical model that enables direct extraction of the most critical information about the isomerization potential energy surface using traditional frequency domain spectroscopic measurements. In Chapter 5, we discuss planned and on-going experimental studies of *cis-trans* isomerization and the S_1 state.

Chapter 2

IR-UV Double Resonance Spectra of *ungerade* Polyads

2.1 Introduction

In this chapter[1], we present analyses of high resolution spectra of the S_1 state in the region 45800-46550 cm^{-1}. This study has two main motivations. The first is to track the evolution of isomerizing states (namely the combination bands 3^m6^n) as their energy approaches that of the isomerization barrier. The second is to establish assignments for all *trans* levels in this energy region, so that remaining states can be assigned to the *cis* conformer with certainty. The region studied corresponds to 3600-4300 cm^{-1} of internal energy in the S_1 state (the *trans* zero-point energy is at 46197.57 cm^{-1}), and contains 22 strongly interacting vibrational levels, most of which are members of bending polyads. Darling-Dennison and Fermi resonances, Coriolis coupling, and local triplet perturbations result in markedly complex spectra. Comprehensive band-by-band analyses, however, have made possible complete *trans* assignments and the identification of two new *cis* states.

[1]This chapter is adapted from work previously published in J.H. Baraban, *et al.*, *Mol. Phys.*, **110**, 2707 (2012). Text and figures have been reproduced with permission of the publisher.

2.2 Experimental details

The excitation schemes used to study the S_1 state are illustrated in Figure 2-1. Due to the $K' - \ell'' = \pm 1$ rotational selection rule of this c-type electronic transition, two sets of double resonance experiments must be performed to sample all $K' = 0 - 2$ states of each vibrational level (note, we will use K and K' interchangably, prefering the latter when clarity is needed). In the first scheme, individual J rotational states of ν_3'' (σ_u^+, antisymmetric CH stretch) are populated via P and R line pumping. From this $\ell'' = 0$ vibrational state, $K' = 1$ states of *ungerade* S_1 levels can be accessed by UV excitation. In the second scheme, $\nu_3'' + \nu_4''$ (Π_u) is pumped via its Q branch (populating several J-levels at once), enabling UV excitation to $K' = 0$ and 2 states. $\nu_1'' + \nu_5''$ can also be used as an alternate intermediate state to $\nu_3'' + \nu_4''$. The $\nu_3'' + \nu_4''$ and $\nu_1'' + \nu_5''$-pumped spectra analyzed in this chapter have been previously reported in Refs. [20] and [21]. The experimental details of those spectra can be found in those references.

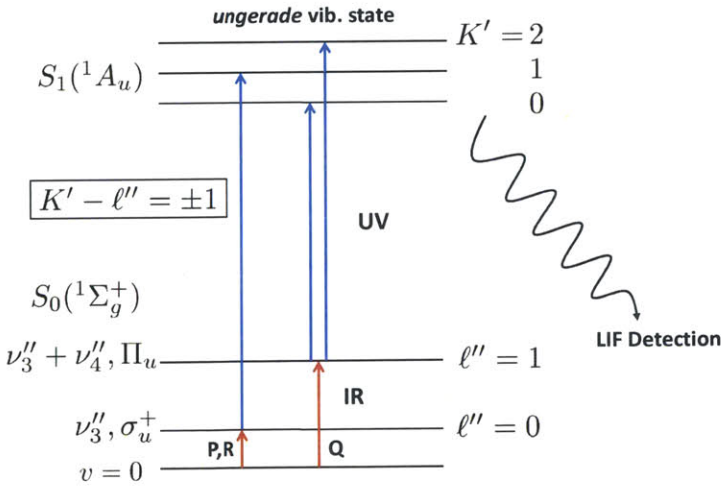

Figure 2-1: Double resonance schemes for S_1 acetylene. Sampling of $K' = 0 - 2$ states of *ungerade* levels requires two sets of double resonance experiments. IR pumping of $\nu_3'', \ell'' = 0$ allows UV excitation to $K' = 1$ states, whereas IR pumping of $\nu_3'' + \nu_4'', \ell'' = 1$ allows UV excitation to $K' = 0$ and 2 states. Resonant excitation is monitored by LIF detection.

The ν_3''-pumped spectra were newly obtained for the purposes of this analysis.

An injection-seeded Nd:YAG laser (Spectra-Physics PRO-270) pumped two tunable dye lasers used for IR and UV generation. The Nd:YAG second harmonic at 532 nm pumped the first dye laser (Lambda Physik FL2002) operating at 790 nm (LDS 798 dye). This output, along with the Nd:YAG fundamental at 1064 nm, pumped a $LiNbO_3$ crystal producing IR radiation via difference frequency generation (DFG). Approximately 1.5 mJ/pulse was achieved in the DFG output. To ensure the resonance of the IR frequency with transitions in the ν_3'' fundamental band [23], a photoacoustic cell with 15 torr of neat acetylene gas at room temperature was monitored before each IR-UV double resonance experiment. The grating-limited IR spectral width was approximately 0.10 cm^{-1}.

The Nd:YAG third harmonic at 355 nm pumped the second dye laser (Lambda Physik FL3002E) to produce laser radiation over the range 460-470 nm (Coumarin 460 dye). This output was frequency doubled with a β-barium borate crystal. A small portion of the fundamental was passed through a $^{130}Te_2$ absorption cell for frequency calibration. An intracavity etalon in the dye laser reduced the spectral bandwidth to 0.04 cm^{-1}, and after frequency doubling, the UV power was approximately 100-200 μJ/pulse. The IR and UV beams were recombined with a dichroic mirror before entering the molecular beam chamber. As a single Nd:YAG pump laser generated both pulses, their relative arrival times at the chamber could be controlled only through the addition of a delay line in the UV beam path. The length of the delay line was such that the UV pulse arrived 15 ns after the IR pulse.

The molecular beam chamber contained an unskimmed supersonic jet of neat acetylene expanded through one of two pulsed valves (Jordan PSV C-21, $d = 0.5$ mm or General Valve, Series 9, $d = 1.0$ mm). The latter achieved superior vibrational cooling, necessary when single-photon hot-bands obscured overlapping IR-UV double resonance features in the spectrum. In both cases, the jet was backed by a pressure of 1 atm and interacted with the IR-UV radiation about 2 cm from the nozzle. The chamber, pumped by an oil diffusion pump, achieved an ultimate pressure of 7×10^{-7} torr, while under gas load it rose to $(0.5 - 2) \times 10^{-5}$ torr.

A Hamamatsu R375 photomultiplier tube collected the laser-induced fluoresence

using $f/1.2$ collection optics and a UG-11 colored glass filter to block laser scatter. Additionally, optical baffles consisting of a set of 3.5 mm aperture irises placed 23 cm from the interaction region and a second set of 5.5 mm aperture irises placed 10 cm from the interaction region were installed in the entrance and exit window arms of the chamber, which significantly reduced laser scatter. The photomultiplier tube signal was split and one line was fed to the input of a 30 dB voltage amplifier (Femto DHPV A-200). This was necessary as the fluorescence intensity of levels in the studied energy region varied over several orders of magnitude. The time-dependent fluorescence signal was recorded for 2 μs after the UV pulse arrival time. For each frequency resolution element, the fluorescence signal was averaged for 20 laser shots. The integration gate of the time signal could be chosen depending on the fluoresence lifetime of the final state. Typically, the fluorescence signal over the first 0.4 μs after the UV laser pulse was integrated. However, for short-lived predissociated states this integration gate had to be moved earlier in time and included the UV laser pulse scatter. In this case, the laser scatter and power fluctuations were small enough not to contribute significantly to the integrated signal noise.

2.3 Results

The 45800-46500 cm^{-1} region consists of congested overlapping structure centered on the very intense $3^3 6^1$ band at 45938 cm^{-1}, with sparser structure to higher frequency. A stick diagram of the congested region is given in Figure 2-2. This regions contains 15 *trans* vibrational levels including $3^1 5^1$, $3^3 B^1$, $1^1 B^1$, $2^1 B^3$, and B^5, and two *cis* levels, including *cis* $3^1 6^1$ (previously reported in Ref. [17])[2]. Partial assignments of B^5 [17, 20], as well as $3^1 5^1$ [13] and $3^3 B^1$ [24] have been previously reported. The assignments of the remaining regions of the spectra, including the sparse higher frequency region containing $2^1 5^1$, $3^2 B^3$, $2^1 3^2 B^1$ and two new cis levels (see Figure 2-3) have not been previously attempted, understandably so, owing to their very complicated nature. In the remainder of this section, we will first comment on predictions

[2] B^n refers to the bending polyad containing the $n+1$ vibrational levels with $n = v_4 + v_6$

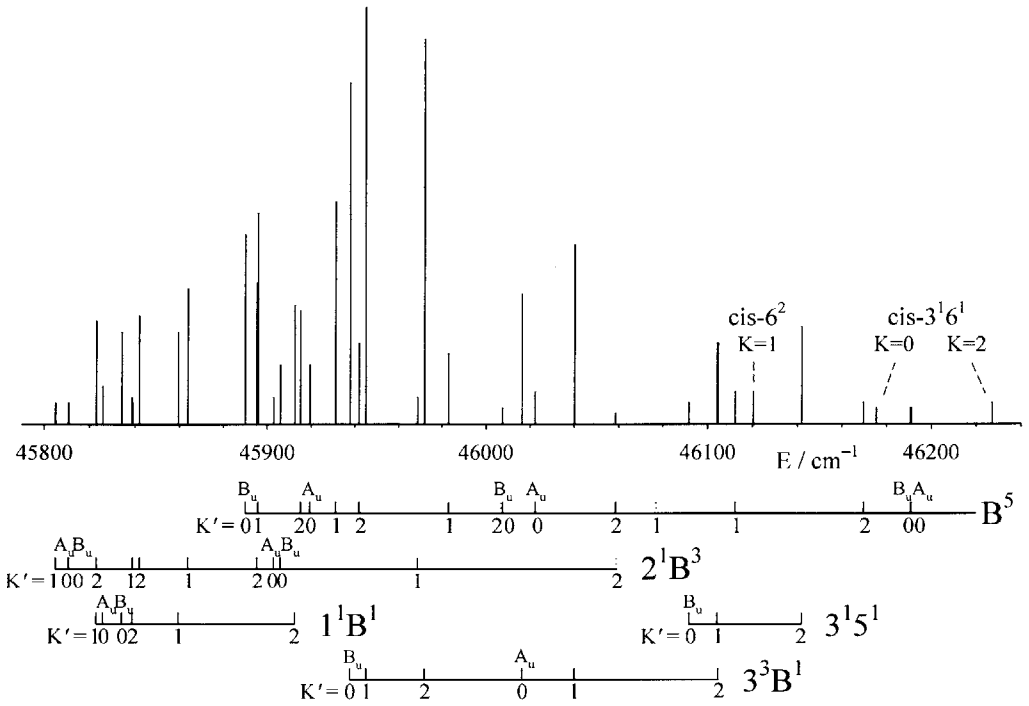

Figure 2-2: Stick diagram of $K' = 0 - 2$ states in the 45800-46240 cm^{-1} region, including both ν_3'' and $\nu_3'' + \nu_4''$-pumped spectra. Assignments are indicated below the stick diagram, with states which could not be found marked with dotted lines.

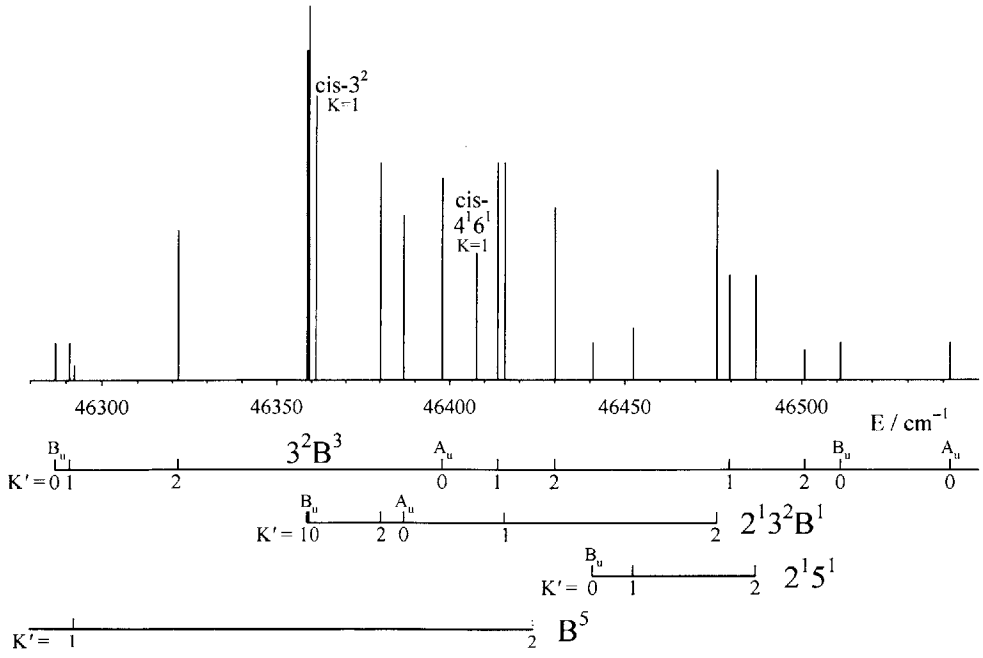

Figure 2-3: Stick diagram of $K' = 0 - 2$ states in the 46280-46550 cm^{-1} region, including both ν_3'' and $\nu_3'' + \nu_4''$-pumped spectra. Assignments are indicated below the stick diagram, with states which could not be found marked with dotted lines.

of the observed polyad structure based on lower energy observations and then present our analyses of each energy region in increasing order. A complete band-by-band rotational analysis of the *ungerade* states in this region can be found Table 1 of Ref. [18] and will not be reproduced here.[3]

2.3.1 Predictions of the polyad structures

Using constants derived from analyses of lower energy polyads [10, 20, 21, 24], the rotational and vibrational structure of higher energy polyads can be predicted by a matrix treatment of the rotational, Coriolis coupling, and Darling-Dennison resonances. The matrix elements for such a calculation are described in detail elsewhere [20], and not included here. Such predictions are essential for making definite assignments of observed levels.

The predictions for the $K = 0-2$ states of the pure bending polyad B^5 were found to be accurate within 7 cm^{-1}. A Fermi resonance of the type $\Delta v_2 = \pm 1, \Delta v_B = \mp 2$ prevents more accurate predictions. However, as this interaction generally leads to small shifts, the observed level structure is reproduced more or less faithfully, except in one instance. In this case, the lowest $K = 0$ a_u and b_u members of B^5 are pushed apart 9 cm^{-1} more than predicted due to a Fermi resonance with $K = 0$ states of 2^1B^3 which happen to lie in between the two B^5 states (see Figure 2-2). The structure of 3^2B^3, reproduced similarly from constants derived from 3^2, 3^2B^1, and 3^2B^2, is accurate to within 10 cm^{-1}. The poorer accuracy for 3^2B^3 are probably an indication that isomerization effects are already manifest in the unraveling of the polyad structure.

In addition to polyad constants, *ab initio* calculations [16] of the x_{14} and x_{16} anharmonicity constants have determined which polyad, 2^1B^3 or 1^1B^1, previously unassigned K states in the 45800 cm^{-1} region belong to (see Ref. [18] for details).

[3]Most of the rotational least-squares fitting and numerical polyad predictions presented in this chapter were performed by Anthony Merer, a coauthor of this work

2.3.2 $K = 0 - 2$ levels in the region 45800-45880 cm^{-1}

The 45800-45880 cm^{-1} region contains the lowest members of the 1^1B^1 and 2^1B^3 polyads. A reduced term value plot of this region's rotational levels is given in Figure 2-4. Several interactions are at play amongst these states. The Darling-Dennison

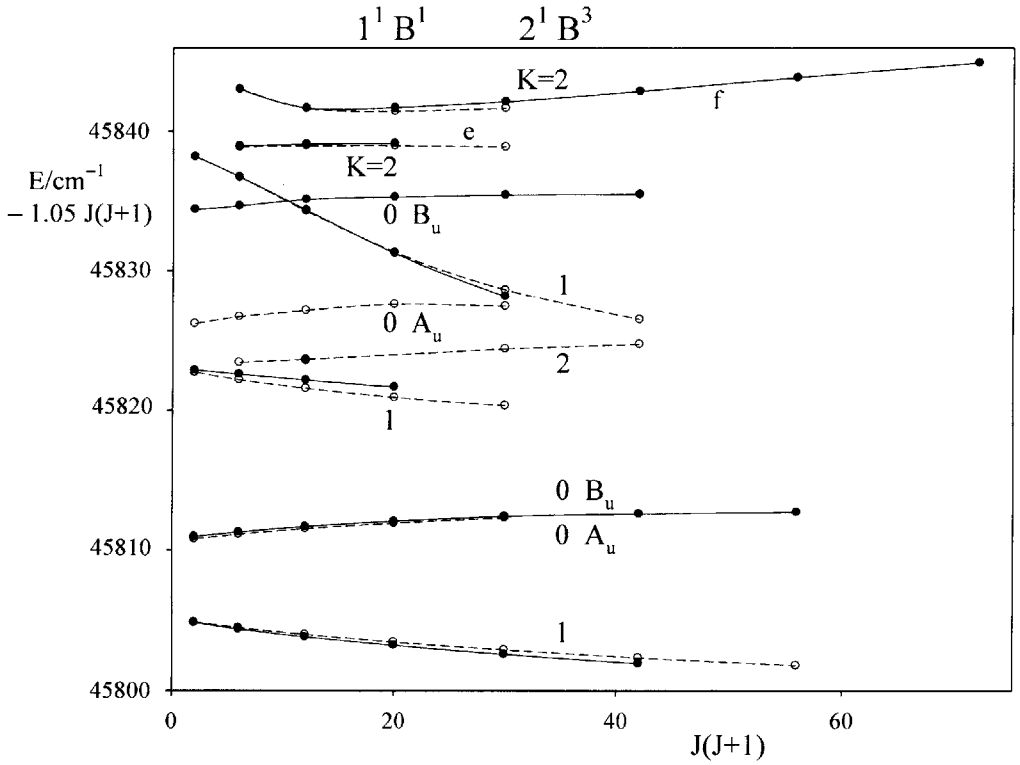

Figure 2-4: Rotational structure of low-energy members of 1^1B^1 and 2^1B^3. Rotational term values are plotted against $J(J+1)$. A quantity $1.05J(J+1)$ cm^{-1} has been substracted from each energy to calculate the reduced term value. States of e parity are plotted with open circles and connected with dashed lines. States of f parity are plotted with filled circles and solid lines. The K assignments are given in two columns, with 1^1B^1 on the right and 2^1B^3 on the left.

resonance in 2^1B^3 results in its two lowest $K = 0$ levels to be nearly degenerate (only 0.2 cm^{-1} apart). For each polyad, the strong a-axis Coriolis coupling pushes the lowest $K = 1$ state *below* the lowest $K = 0$ states. Strong b-axis Coriolis interactions are evident in the highest $K = 1$ and 2 states of 2^1B^3 included in Figure 2-4. These levels push each other apart more strongly with increasing J as is expected of b-axis interactions. The $K = 1$ state has such a low effective B rotational constant

(0.6 cm^{-1}) that its R branch forms a head at only $J'' = 1$ in the double resonance spectrum via ν_3'' (see Figure 2-5). The b-axis Coriolis coupling (with selection rule

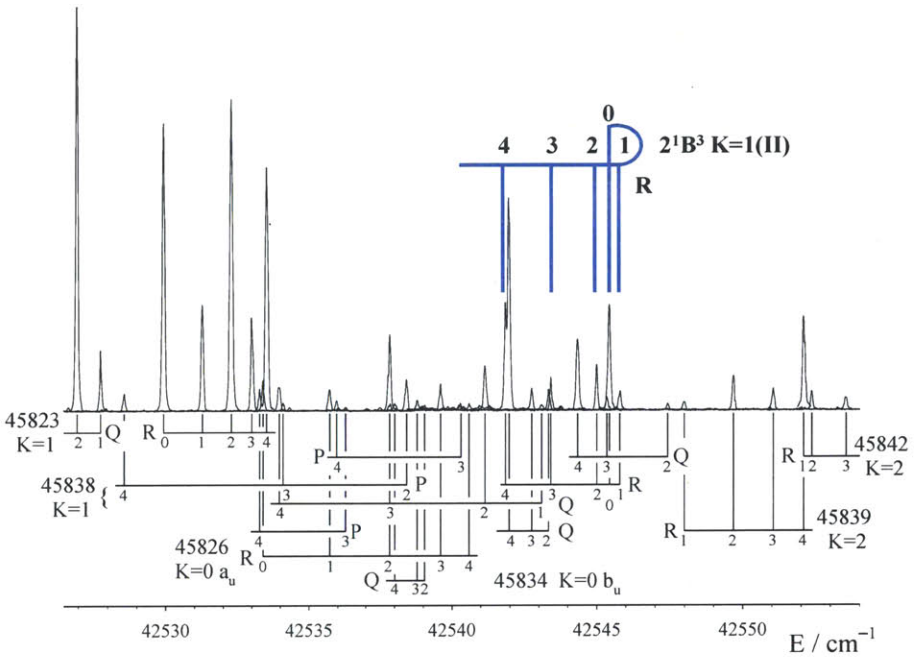

Figure 2-5: Double resonance spectrum of 2^1B^3 $K = 1$(II) via ν_3''. The R branch of this band forms a head at $J'' = 1$ due to the exceptionally strong b-axis coupling with the $K = 2$ state directly above. Despite the severe congestion of the bands in this small region, rotational assignments for every line can be made, as indicated in the bottom of the figure. Five different spectra (from each of $J'' = 0 - 4$ IR pumped experiments) are overlayed as one. The energy scale is the UV excitation energy.

$\Delta K = \pm 1$) is, in general, large enough amongst these states that almost every K state appears in both ν_3'' and $\nu_3'' + \nu_4''$-pumped excitation spectra, indicating that K is no longer is good quantum number and only retains use as a nominal state label.

With the observation of 1^1B^1, the first experimentally measured values for the x_{14} and x_{16} anharmonicities can be determined. Their values, as determined by least-squares fits, are -16.67 and -11.62 cm^{-1}, respectively. These values are necessary for predicting the locations of higher lying polyads with at least one quantum of excitation in ν_1.

2.3.3 $K = 0 - 2$ levels in the region 45890-45990 cm^{-1}

The region spanning 45890-45990 cm^{-1} is dominated by the very intense Franck-Condon active $3^3 6^1$ level. Anharmonic resonances transfer this intensity to all of the surrounding states (which include members of B^5, $2^1 B^3$ and $1^1 B^1$) so that all 15 $K = 0 - 2$ states expected in this region are observed. The level structure in this region is more or less well behaved except for the immediate vicinity of $3^3 6^1$ $K = 1$ which contains a complicated many-state interaction trainwreck. The IR-UV double resonance spectrum of $3^3 6^1$ $K = 1$ is reproduced in Figure 2-6. P/R pumping of ν_3''

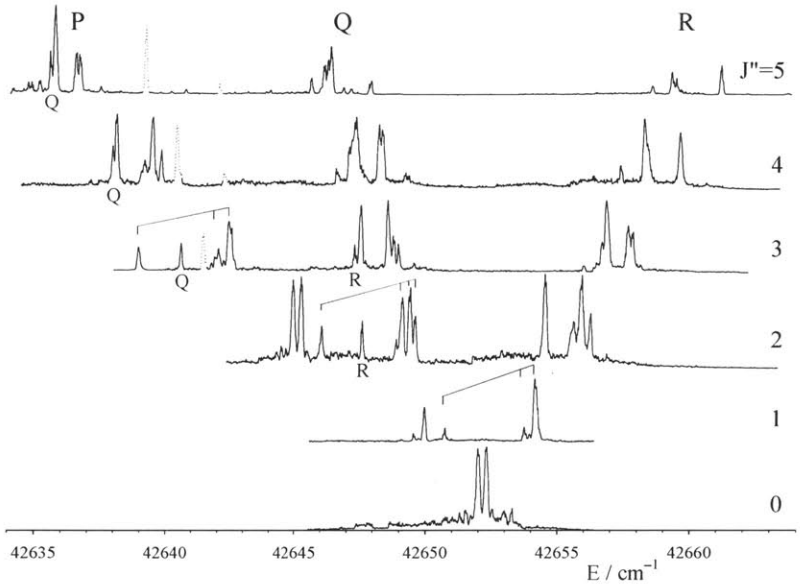

Figure 2-6: IR-UV double resonance spectrum of the $3^3 6^1$ $K = 1$ state via ν_3''. The spectrum is separated by J'' as ν_3'' double resonance spectra are pumped by individual P and R lines. The $J' = 2$ line pattern is indicated by tie-lines for its P, Q, and R lines. The stucture shows the $K = 2$ perturbing state (see text), as well as smaller splittings due to triplet perturbations. Lines from the neighboring $3^3 6^1$ $K = 0$ state are dashed. The energy scale is that of the UV photon, not total term energy.

enables the congested spectrum to be separated by J''. Lines in each of the P, Q, and R branches are split into several components due to perturbations by a dense background of triplet states. This is confirmed by observations of extremely long lifetimes and strong zero-field quantum beats typical of triplet perturbations [24]. A reduced term value plot of this state and neighboring levels is given in Figure 2-7.

The solid lines represent observed states. The dashed lines are calculated positions

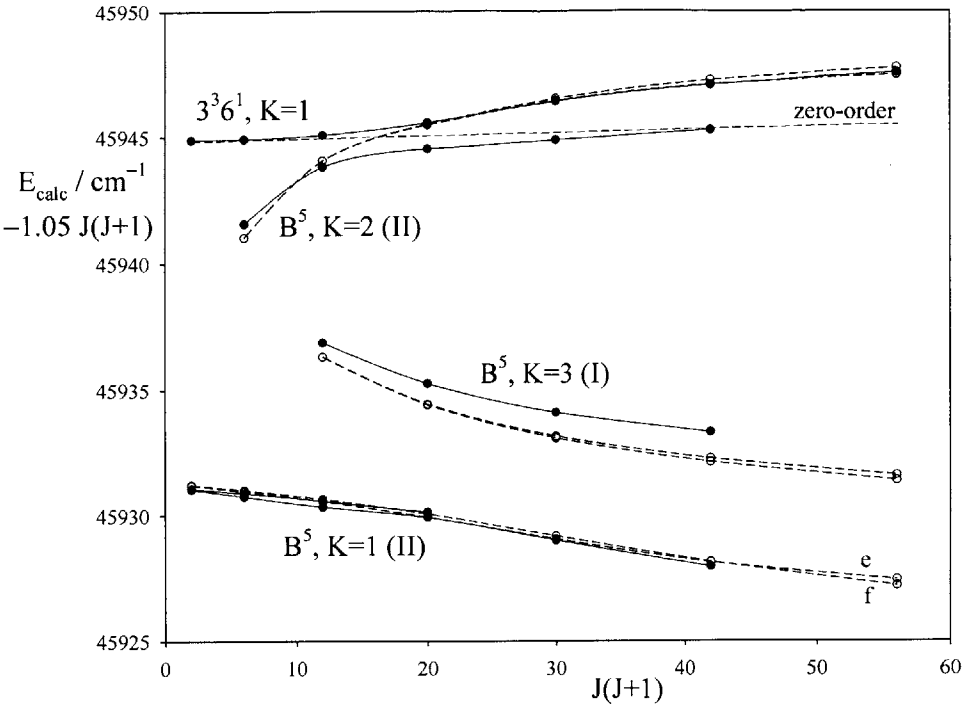

Figure 2-7: Rotational structure of states near 45940 cm^{-1}. Four different *trans* states interact in this region leading to very complicated spectra. Observed positions are shown with filled circles connected with solid lines. Predictions from polyad constants (corrected by an offset of 3 cm^{-1}) are shown with open circles connected by dashed lines. 3^36^1 $K = 1$ and B^5 $K = 2$(II) undergo an avoided crossing between $J = 3$ and 4. Additional interactions couple the states B^5 $K = 3$(I) and $K = 1$(II).

based on constants from lower energy polyads (an offset of 3 cm^{-1} has been added to compensate for inexact extrapolation of the polyad constants). Examination of the level patterns indicates that there are several interactions present. 3^36^1 $K = 1$ undergoes an avoided crossing with B^5 $K = 2$(II). This is consistent with the fact that the observed triplet perturbations switch from affecting the higher of the two states to the lower of the two states after the avoided crossing (i.e. the triplet interactions track the zero-order 3^36^1 vibrational character). B^5 $K = 2$(II) interacts via b-axis Coriolis coupling with B^5 $K = 3$(I), as well as B^5 $K = 1$(II), as is evident by the curvature of their reduced term value plots. The network of b-axis coupled states, as well as the appearance of $K = 2$ and 3 states in the ν_3''-pumped spectra demonstrate

how thorougly mixed the K character of these states is. We also note that the large 1-2 cm^{-1} splittings of the $J \geq 2$ levels of $3^3 6^1$ $K = 1$ reported in previous work [24, 25] are *not* the result of triplet interactions (which are much smaller in this band), but from the avoided crossing with B^5 $K = 2$(II).

Interactions between other states in this region are less drastic. A Fermi resonance between the near degenerate $2^1 B^3$ $K = 2$(III) and B^5 $K = 1$(I) states occurs near 45896 cm^{-1}. This same Fermi resonance is responsible for the interaction between the $K = 0$ states of $2^1 B^3$ and B^5 discussed in the previous section.

The $3^3 6^1$ $K = 2$ state also displays triplet perturbations, but is isolated from interactions with other singlet vibrational states. At low J, the nominal singlet lines split into a few well separated components, with typical spacings of around 0.2 cm^{-1}. With increasing J, the density of perturbing triplet levels increases, and the components coalesce into a single broad line. In $3^3 6^1$ $K = 2$, for example, the $J' = 2$ level has four distinguishable components. Each parity component has the same number of lines, but with different splitting patterns. The $J' = 3$ level has at least five poorly resolved components, and the $J' = 6$ components cannot be resolved and appear as a single line.

2.3.4 $K = 0 - 2$ levels in the region 46000-45250 cm^{-1}

The 46000-45250 cm^{-1} region contains the $K = 0 - 2$ states from $3^3 4^1$ [24] and $3^1 5^1$ [13], as well as eight states from the B^5 polyad. Bands from *cis* 6^2 and *cis* $3^1 6^1$ are also observed. The *cis* 6^2 $K = 0$ and *cis* $3^1 6^1$ bands have already been reported in Ref. [17], but *cis* 6^2 $K = 1$ is a new observation. In contrast to $3^3 6^1$, the $3^3 4^1$ vibrational level is less perturbed by triplet states, with extra lines appearing only at low J' for all three $K = 0 - 2$ states. $3^3 4^1$ $K = 2$ lies very close to $3^1 5^1$ $K = 1$. The $J = 5e$ level of the latter state is affected by triplet perturbations which split the line into at least four components over 0.7 cm^{-1}. This is the first example of triplet perturbations in a level involving ν_5.

The observation of *cis* 6^2 $K = 1$ is an exciting find because it provides the second example of K-staggering in isomerizing levels of S_1 (the first being *cis* $3^1 6^1$ [17]).

Because of the different selection rules for *cis* states, the *cis* 6^2 $K = 0$ state was observed in one-photon hot band spectra from ν_4'' (π_g) at 46114.0 cm^{-1} [17]. The $K = 1$ band, which appears at 46120.3 cm^{-1}, results in an apparent $A - \frac{1}{2}(B - C)$ rotational constant of 6.3 cm^{-1}. The discrepancy with the expected value of this quantity, about 13 cm^{-1}, indicates an even-odd K-staggering exists, resultant from tunneling through the isomerization barrier. Since the $K = 2$ state of *cis* 6^2 has yet to be observed, we can only report an approximate K-staggering measurement of $-(5 - 7)$ cm^{-1}.

Two $K = 2$ states, one from B^5 and another from 2^1B^3, are expected at 46059 cm^{-1}, but only one very weak band is found. It is provisionally assigned to B^5, since this polyad generally gives stronger bands than 2^1B^3. Of the 43 upper states with $K = 0-2$ expected in the 45800-46250 cm^{-1} region, all but three have been identified. The derived constants enable the positions of the remaining levels to be predicted to within a few cm^{-1}.

2.3.5 The 3^2B^3 and $2^13^2B^1$ polyads (46250-46550 cm^{-1})

The highest energy region of this study, 46250-46550 cm^{-1}, contains seven vibrational levels from the *trans* manifold and two identified *cis* levels. A Fermi resonance between 3^2B^3 and $2^13^2B^1$ complicates the structure of these overlapping bands. 2^15^1, high-lying members of B^5, *cis* 3^2, and *cis* 4^16^1 complete the rest of the observed levels. The overview stick diagram of this region has already been given in Figure 2-3. The large ν_3/ν_6 cross anharmonicity breaks up the 3^2B^3 polyad resulting in less severe Coriolis coupling amongst the zero-order states as compared to other polyads such as 1^1B^1 and 2^1B^3. The predicted positions of 3^2B^3 and $2^13^2B^1$ from lower energy polyad constants allowed fairly straightforward assignments for most of this region. One local region where several states interact strongly is near 46359 cm^{-1}. The reduced term value plot of these levels is given in Figure 2-8. The only expected levels at this energy are the $K = 0$ and 1 states of the nominal $2^13^26^1$ vibrational state. These levels are nearly degenerate at the zero-rotation limit. Via coupling to the nominal $2^13^24^1$ $K = 1$ level 28 cm^{-1} above, the f components interact strongly,

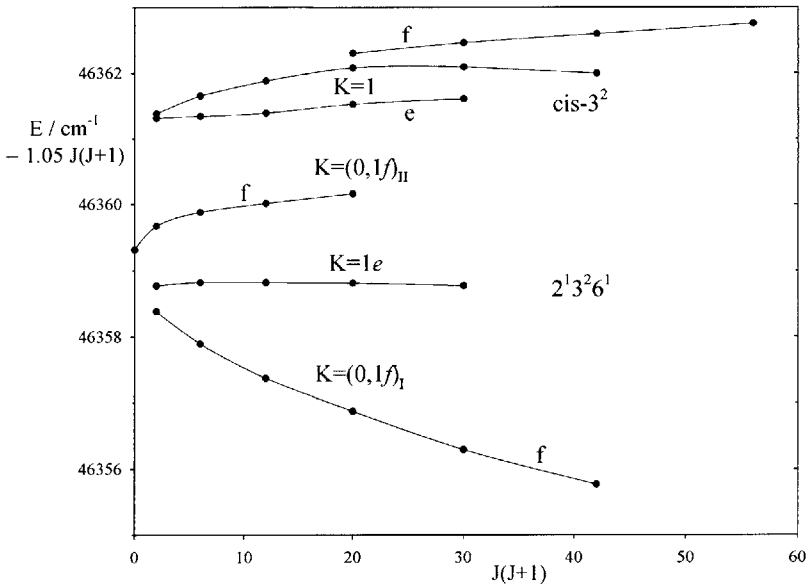

Figure 2-8: Rotational structure of states near 46360 cm^{-1}. The lowest three bands belong the $K = 0$ and 1 states of $2^1 3^2 6^1$. Strong b-axis Coriolis coupling mixes the $K = 0$ state with the f component of the $K = 1$ state. These states interact with another $K = 1$ state a few cm^{-1} higher, which cannot be accounted for by expected *trans* levels in this region, indicating that is must belong to the *cis* conformer. Its assignment as *cis* 3^2 is based on the observed vibrational symmetry and *ab initio* predictions of the level position [16]. An additional $K = 3$ state appears in the spectrum via interactions with the *cis* level.

resulting in a parabola shape typical of Coriolis coupling. The e levels of the $K = 1$ state are unaffected. The upper $K = 1$ level near 46361 cm^{-1} cannot be accounted for by expected levels within the *trans* manifold. Recent *ab initio* VPT2 calculations of the *cis* vibrational structure [16] offer two candidates that lie close to this energy with the correct symmetry: *cis* 2^1 and *cis* 3^2. 3D reduced dimension DVR calculations [22] predict that *cis* 3^2 should interact much more strongly with *trans* and therefore have greater intensity than *cis* 2^1. Therefore, this state is assigned as *cis* 3^2 $K = 1$. Additional *ab initio* variational results presented in the next chapter further support this assignment.

Approximately 50 cm^{-1} higher, three more $K = 1$ states are observed at 46408, 46414, and 46416 cm^{-1}. Two of these can be accounted for by predictions of 3^2B^3 and $2^13^2B^1$ K=1 states at 46411 and 46418 cm^{-1}. The predictions are not accurate enough to determine which state is which other than that the two strongest $K = 1$ states can securely be assigned to the *trans* manifold. The much weaker third $K = 1$ state is presumably *cis* and from the rotational selection rules must have B_1 vibrational symmetry. As B_1 levels must have odd quanta of both ν_4 (a_2) and ν_6 (b_2), the only logical assignment at this energy is *cis* 4^16^1.

2.4 Discussion

In this chapter, we have presented a detailed analysis of *ungerade* vibrational levels of *trans* S_1 acetylene as observed in IR-UV double resonance. The assignments in this region have established the complete vibrational level structure of this electronic state up to 4300 cm^{-1} of vibrational energy. Having accomplished the comprehensive assignment of all expected *trans* states in this region, two additional *cis* states have been identified, bringing the total number of secure *cis* levels to six.

The barrier to isomerization is calculated [22] to lie around 5000 cm^{-1} abouve the *trans* zero point. We expect that signatures of *cis-trans* isomerization should already be present in the observed levels. Indeed, K-staggerings have now been observed in the two *cis* levels for which both even and odd-K states have been observed. *cis*

3^16^1 was found [17] to have a staggering of $+3.9$ cm^{-1}, while this work shows that *cis* 6^2 appears to have a stagerring of about -5 cm^{-1}. K-staggerings in *trans* states in this energy region would unfortunately be obscured by the Coriolis and Darling-Dennison interactions between the bending modes. It may be, however, that the less accurate predictions of 3^2B^3's rovibrational structure is indicative that K-staggerings are appreciably affecting the level structure. The investigation of the magnitude and direction of K-staggerings for both *cis* and *trans* levels is thus a major motivation for *ab initio* rovibrational calcultions, presented in the next chapter.

Only about one bending quantum remains between the levels analyzed in this chapter and the expected transition state energy. Information gained from the analyis of 1^1B^1 and 2^1B^3 has already been useful in the analysis of unpublished one-photon spectra of *gerade* states, which contain additional *cis* levels and members of 3^36^2 and 3^46^2, levels which lie along the isomerization path. In the on-going analysis of these spectra, additional *ab initio* calculations will also prove a useful tool in predicting the patterns of rovibrational structure in barrier-proximal levels.

Chapter 3

Reduced Dimension Rovibrational Variational Calculations

3.1 Introduction

All analyses of molecular spectra rely on identifying patterns. In the simplest cases, we can understand rovibrational spectra by using only the most basic of models: the rigid rotor and harmonic oscillator. Effective Hamiltonians can model perturbative interactions between such states, and often reduce immense spectral complexity to only a handful of physical parameters. Such has been done successfully for much of the bending polyad structure of *trans* acetylene. In many cases, empirical polyad constants determined at low energies can predict higher lying structure to nearly experimental accuracy due to simple scaling relations of the polyad constants with rovibrational quantum numbers (see Chapter 2). In S_1 C_2H_2, however, the multi-well landscape and the presence of a transition state saddle point introduce severe anharmonicities and tunneling interactions, which challenge the applicability of effective Hamiltonians. Phenomena such as K-staggering, which is directly caused by the presence of multiple potential wells, are not easily accounted for in a global fashion with models like effective Hamiltonians that are suited to describe one isolated equilibrium geometry.

In order to develop an understanding of what new patterns and structures we

should expect in an isomerizing system with asymmetric wells, how to interpret these patterns, and what signatures they will leave in spectra, *ab initio* calculations of S_1 acetylene's rovibrational structure are required. Many theoretical contributions have already been made to understanding the rovibrational structure of the S_1 state, including recent 3D DVR [22] and anharmonic force field [16] calculations which have been used in the analysis of the *ungerade* IR-UV double resonance spectra. In this chapter, we present 4D variational calculations fully including the molecule's total angular momentum, J. This is the highest dimensionality of *ab initio* rovibrational variational calculations of the S_1 state of which the author is aware. A variational treatment is desireable because it includes few assumptions, predicts the entire global rovibrational structure, and can quite flexibly treat the large amplitude motions implicit in the isomerization process. The calculations presented here are still being refined, but have already proved successful at reproducing much of the bending, torsional, and rotational structure of the S_1 state and providing insights into the level structure of both low energy vibrational states and barrier-proximal regions.

3.2 Methodology

3.2.1 Coordinate Systems, Body-Fixed Frame, and Dimension Reduction

Our calculations make use of a multivalued coordinate system suitable for simultaneous treatment of *cis* and *trans* conformers. We follow the sequentially bonded internal coordinate conventions of Ref. [26], which are shown in Figure 3-1. These coordinates are multivalued, i.e. multiple choices of internal coordinates correspond to the same configuration in the lab frame. For example, the configurations $(\beta_1, \beta_2, \alpha, \chi)$, $(-\beta_1, -\beta_2, \alpha, \chi + \pi)$, and $(-\beta_1, -\beta_2, \alpha + \pi, \chi)$ yield identical positions for each atom in the lab frame. The consequence of such multivaluedness is that we must impose a requirement that the final (single-valued) rovibronic wavefunctions are symmetric with respect to transformations between these equivalent configurations. These

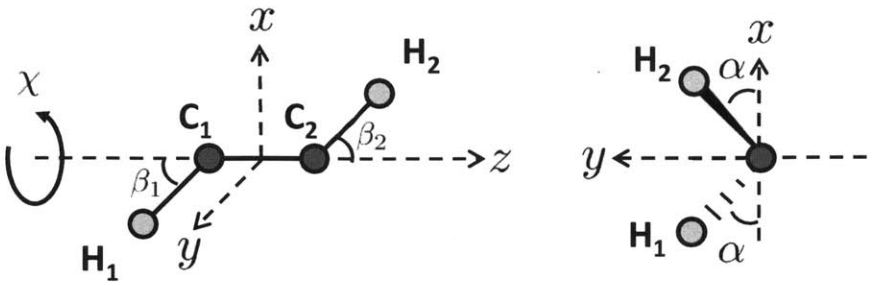

Figure 3-1: Sequentially bonded internal coordinate system. β_1 and β_2, the two CCH angles, span from $-\pi$ to π and α, the torsional angle, from 0 to 2π. The three Euler angles, θ, ϕ, and χ, relate the (xyz) body-fixed frame to the lab-fixed frame in the usual way [27]. The body-fixed origin is taken to be at the nuclear center of mass. The z-axis is parallel to the C-C axis and the y-axis bisects the two CCH planes. The three bond lengths r_1, r_2, and r_3 (not shown) are the C_1-H_1, C_2-H_2, and C_1-C_2 distances, respectively.

symmetry constraints are systematically treated using an extended complete nuclear permutation inversion (CNPI) symmetry group [27, 28]. The extended CNPI group appropriate for *cis-trans* isomerizing acetylene is the $G_4^{(8)}$ group, which is treated in full detail in Ref. [26]. All subsequent symmetry species will refer to the irreducible representations of $G_4^{(8)}$. For the transformation properties of the various coordinates under operations of $G_4^{(8)}$ and for the group's character table, the reader should refer to Tables 9 and 10 of Ref. [26]. The use of $G_4^{(8)}$ is discussed further below in the context of K-staggering.

In order to reduce the computational demands of a full dimensional rovibrational calculation, which would have $3N - 3 = 9$ degrees of freedom (including the three rotations), we will make the approximation of rigid CH bond lengths, leaving only 4 internal vibrational degrees of freedom (r_3, β_1, β_2, and α) and the 3 Euler angles. Freezing the CH bonds is a fairly good approximation as their motions are not significantly involved in the complicated bending-torsion-rotation dynamics. Additionally, the symmetric and anti-symmetric CH stretching modes (ν_1 and ν_5) have considerably higher frequencies than the remaining modes in either conformer and are approximately separable. The inclusion of the two bending and single torsional degrees of freedom is obviously necessary in order to study the level structure of *cis-*

trans isomerization (which in principle could occur through either an in-plane bending pathway or an out-of-plane torsional pathway). We include the CC stretch, r_3, as well because of its significant contribution to the symmetric bending normal mode, ν_3. With these degrees of freedom, the (4+3)D calculation will yield rovibrational wavefunctions and energies for states involving modes ν_2, ν_3, ν_4, and ν_6 of the the *cis* and *trans* conformers.

3.2.2 Basis Functions

It is computationally most efficient to solve for the complete rovibrational wavefunction, Ψ, as an expansion of direct products of one-dimensional functions of each internal coordinate and the symmetric top rotational wavefunctions,

$$\Psi = \sum \psi(r_3)\psi(\beta_1)\psi(\beta_2)\psi(\alpha)|J,k\rangle.$$

We will first consider the bending-torsion-rotation factor as it involves special treatment due to multivaluedness and divergent matrix elements.

A convenient set of one-dimensional basis functions for the bending angles is the associated Legendre polynomials with the customary argument of $\cos(\beta)$. In this form, the Legendre polynomials are typically defined only over $\beta = [0, \pi]$. Since our coordinate system extends β over $-\pi$ to π, we define an extended Legendre polynomial basis function as

$$\mathcal{L}_\ell^{m\pm}(\beta) \equiv \frac{\mathcal{N}_\ell^m}{\sqrt{2}} \begin{cases} P_\ell^m(\cos\beta) & 0 < \beta < \pi \\ \pm P_\ell^m(\cos\beta) & -\pi < \beta < 0 \end{cases} \tag{3.1}$$

where

$$\mathcal{N}_\ell^m = (-1)^m \sqrt{\frac{(\ell+1/2)(\ell-m)!}{(\ell+m)!}}, \tag{3.2}$$

such that the basis functions are normalized over $-\pi$ to π with volume element

$|\sin\beta|d\beta$:

$$\int_{-\pi}^{\pi}(\mathcal{L}_{\ell}^{m\pm})^2|\sin\beta|d\beta = 1. \tag{3.3}$$

ℓ and m are the usual polynomial degree and order. Legendre polynomials with the same value of m but different values of ℓ are orthogonal; however, functions with different values of m may be nonorthogonal. We will make use of the following shorthand notation for the product of two bending functions

$$(\ell_1^{s_1}\ell_2^{s_2}) = \mathcal{L}_{\ell_1}^{m_1 s_1}(\beta_1)\mathcal{L}_{\ell_2}^{m_2 s_2}(\beta_2), \tag{3.4}$$

where $s_{1,2} = +$ or $-$. The degree and order of the Legendre polynomials obey $\ell \geq m \geq 0$.

The torsional degree of freedom is expanded in a Fourier series. Its basis functions are

$$|n,\pm\rangle \equiv \mathcal{M}_n \begin{cases} \cos(n\alpha), & + \\ \sin(n\alpha), & - \end{cases} \tag{3.5}$$

where $n \geq 0$ and $\mathcal{M}_n$ is a suitable constant for normalization over $\alpha = [0, 2\pi]$.

For the rotational wavefunctions, we choose symmetrized symmetric top wavefunctions

$$|Jk,\pm\rangle \equiv \mathcal{N}_{Jk\pm}\frac{1}{\sqrt{2}}\left[|J,k\rangle^{CS} \pm |J,-k\rangle^{CS}\right] \tag{3.6}$$

where $\mathcal{N}_{Jk\pm} = i^{\frac{1}{2}[(-1)^k \pm (-1)^J]}$ (note that for $k = 0$, the factor $1/\sqrt{2}$ becomes $1/2$ and only a $+$ choice exists). The wavefunctions $|J,k\rangle^{CS}$ are signed-k symmetric top wavefunctions following the standard Condon-Shortley phase convention [29]. We take plus and minus linear combinations (a Wang transformation [30]) for symmetrization. The non-standard phase factor guarantees purely real matrix elements for rotational terms in the molecular kinetic energy operator, which will be discussed in more detail

below.

The $G_4^{(8)}$ symmetry species of the primitive bending, torsional, and rotational wavefunctions are summarized in Table 3.1. Symmetrized products of these primitive basis functions must be taken such that the total rovibronic wavefunction belongs to one of the single-valued irreducible representations of $G_4^{(8)}$ (A_{1g}^+, A_{2g}^-, B_{2u}^+, and B_{1u}^-). Following the assumptions in Ref. [26], we take the electronic symmetry of the S_1 state to be B_{1u}^-. As this species is single-valued, the bending-torsional-rotational wavefunction must itself be single-valued. The symmetrized bending-torsional-rotational wavefunctions are given in Table 3.2. The choice of m_1 and m_2 will be determined by consideration of divergences in the kinetic energy operator. A discussion of their derivation will be postponed until further, but we will anticipate the results now and quote them here:

$$m_1 = 0 \text{ if } k+n=0, \text{ otherwise } m_1 = \begin{cases} 1, & |k+n|/2 = odd \\ 2, & |k+n|/2 = even \end{cases}$$

$$m_2 = 0 \text{ if } k-n=0, \text{ otherwise } m_2 = \begin{cases} 1, & |k-n|/2 = odd \\ 2, & |k-n|/2 = even \end{cases}$$

The CC stretch factor is considerably simpler than the bending-torsional-rotational factor. The r_3 coordinate is totally symmetric, so a simple direct product between its primitive basis and symmetrized bending-torsional-rotational wavefunctions is sufficient to generate a 4D basis. Various stretching bases can used, such as Morse oscillator or harmonic oscillator wavefunctions. In this implementation, we use a harmonic oscillator DVR (HO-DVR) basis, which greatly simplifies integrals of the potential function in the r_3 dimension.

The number of basis functions required in each dimension in order to reach convergence varies with the type of coordinate. For the bending functions, Legendre polynomials with degrees such that $\ell_1 + \ell_2 \leq 30$ are sufficient. Similarly, the torsional basis functions, $|n, \pm\rangle$, can generally be restricted to values of $n \leq 60$. The stretch is more easily saturated, and a ten-point DVR is sufficient. A full (4+3)D calculation would then require $\sim (2J+1)10^{5-6}$ basis functions, which begins to push

Table 3.1: Symmetry species of bending, torsional, and rotational wavefunctions. The irreducible representations are those of $G_4^{(8)}$ [26]. The symmetry species of the rotational wavefunctions can be derived with standard methods [27] or used directly from Ref. [31]. ($'$) and ($''$) refer to components of E^+ degenerate pairs which are symmetric and antisymmetric, respectively, with respect to the ab symmetry operation. (g) and (u) refer to the symmetry of E_1 components with respect to bc . (1) and (2) refer to the symmetry of E_g components with respect to b. (ab, bc, and b are $G_4^{(8)}$ operators written in terms of the group's generators, see [26].)

Basis Function	Γ
$(\ell_1^+\ell_2^+) + (\ell_2^+\ell_1^+)$	A_{1g}^+
$(\ell_1^+\ell_2^+) - (\ell_2^+\ell_1^+)$	B_{2u}^+
$(\ell_1^-\ell_2^-) + (\ell_2^-\ell_1^-)$	B_{1g}^+
$(\ell_1^-\ell_2^-) - (\ell_2^-\ell_1^-)$	A_{2u}^+
$\{(\ell_1^+\ell_2^-), (\ell_2^-\ell_1^+)\}$	$E^+(''), E^+(')$
$\{(\ell_1^-\ell_2^+), (\ell_2^+\ell_1^-)\}$	$E^+('), E^+('')$
$\|4n, +\rangle$	A_{1g}^+
$\|4n+2, +\rangle$	B_{1g}^+
$\|4n, -\rangle$	B_{1u}^-
$\|4n+2, -\rangle$	A_{1u}^-
$\{\|4n+1, +\rangle, \|4n+1, -\rangle\}$	$E_1^{(u)}, E_1^{(g)}$
$\{\|4n+3, +\rangle, \|4n+3, -\rangle\}$	$E_1^{(u)}, E_1^{(g)}$
$\|J, 4k, +(-1)^J\rangle$	A_{1g}^+
$\|J, 4k+2, +(-1)^J\rangle$	B_{1g}^+
$\|J, 4k, -(-1)^J\rangle$	A_{2g}^-
$\|J, 4k+2, -(-1)^J\rangle$	B_{2g}^-
$\{\|J, 4k+1, +(-1)^J\rangle, \|J, 4k+1, -(-1)^J\rangle\}$	$E_g^{(1)}, E_g^{(2)}$
$\{\|J, 4k+3, +(-1)^J\rangle, \|J, 4k+3, -(-1)^J\rangle\}$	$E_g^{(1)}, E_g^{(2)}$

Table 3.2: Symmetrized bending-torsional-rotational product wavefunctions. These symmetrized linear combinations of primitive bending, torsional, and rotational product wavefunctions belong to the single-valued irreducible represenations of $G_4^{(8)}$. The $\pm$ in the center of each expression gives A_{1g}^+ and A_{2g}^- for $+$ and B_{2u}^+ and B_{1u}^- for $-$. See the text for the rules determining the values of m_1 and m_2. The symbols $S^\pm$ are an abbreviation for $\pm(-1)^J$.

Γ^{btr}	$\lvert\psi^{btr}\rangle = \mathcal{N}\left[(\ell_1^{s_1}\ell_2^{s_2})\{\lvert n,s_t\rangle\lvert Jk,s_k(-1)^J\rangle + s_ts_k\lvert n,-s_t\rangle\lvert Jk,-s_k(-1)^J\rangle\} \pm (\ell_2^{s_2}\ell_1^{s_1})\{\lvert n,s_t\rangle\lvert Jk,s_k(-1)^J\rangle - s_ts_k\lvert n,-s_t\rangle\lvert Jk,-s_k(-1)^J\rangle\}\right]$
$A_{1g}^+/$	$\mathcal{N}\left[(\ell_1^+\ell_2^+)\{\lvert 4n+0,+\rangle\lvert J,4k+0,S^+\rangle + \lvert 4n+0,-\rangle\lvert J,4k+0,S^-\rangle\} \pm (\ell_2^+\ell_1^+)\{\lvert 4n+0,+\rangle\lvert J,4k+0,S^+\rangle - \lvert 4n+0,-\rangle\lvert J,4k+0,S^-\rangle\}\right]$
B_{2u}^+	$\mathcal{N}\left[(\ell_1^-\ell_2^-)\{\lvert 4n+2,+\rangle\lvert J,4k+0,S^+\rangle + \lvert 4n+2,-\rangle\lvert J,4k+0,S^-\rangle\} \pm (\ell_2^-\ell_1^-)\{\lvert 4n+2,+\rangle\lvert J,4k+0,S^+\rangle - \lvert 4n+2,-\rangle\lvert J,4k+0,S^-\rangle\}\right]$
	$\mathcal{N}\left[(\ell_1^+\ell_2^+)\{\lvert 4n+2,+\rangle\lvert J,4k+2,S^+\rangle + \lvert 4n+2,-\rangle\lvert J,4k+2,S^-\rangle\} \pm (\ell_2^+\ell_1^+)\{\lvert 4n+2,+\rangle\lvert J,4k+2,S^+\rangle - \lvert 4n+2,-\rangle\lvert J,4k+2,S^-\rangle\}\right]$
	$\mathcal{N}\left[(\ell_1^-\ell_2^-)\{\lvert 4n+0,+\rangle\lvert J,4k+2,S^+\rangle + \lvert 4n+0,-\rangle\lvert J,4k+2,S^-\rangle\} \pm (\ell_2^-\ell_1^-)\{\lvert 4n+0,+\rangle\lvert J,4k+2,S^+\rangle - \lvert 4n+0,-\rangle\lvert J,4k+2,S^-\rangle\}\right]$
	$\mathcal{N}\left[(\ell_1^-\ell_2^+)\{\lvert 4n+1,+\rangle\lvert J,4k+1,S^-\rangle - \lvert 4n+1,-\rangle\lvert J,4k+1,S^+\rangle\} \pm (\ell_2^+\ell_1^-)\{\lvert 4n+1,+\rangle\lvert J,4k+1,S^-\rangle + \lvert 4n+1,-\rangle\lvert J,4k+1,S^+\rangle\}\right]$
	$\mathcal{N}\left[(\ell_1^+\ell_2^-)\{\lvert 4n+3,+\rangle\lvert J,4k+1,S^-\rangle - \lvert 4n+3,-\rangle\lvert J,4k+1,S^+\rangle\} \pm (\ell_2^-\ell_1^+)\{\lvert 4n+3,+\rangle\lvert J,4k+1,S^-\rangle + \lvert 4n+3,-\rangle\lvert J,4k+1,S^+\rangle\}\right]$
	$\mathcal{N}\left[(\ell_1^+\ell_2^-)\{\lvert 4n+1,+\rangle\lvert J,4k+3,S^-\rangle - \lvert 4n+1,-\rangle\lvert J,4k+3,S^+\rangle\} \pm (\ell_2^-\ell_1^+)\{\lvert 4n+1,+\rangle\lvert J,4k+3,S^-\rangle + \lvert 4n+1,-\rangle\lvert J,4k+3,S^+\rangle\}\right]$
	$\mathcal{N}\left[(\ell_1^-\ell_2^+)\{\lvert 4n+3,+\rangle\lvert J,4k+3,S^-\rangle - \lvert 4n+3,-\rangle\lvert J,4k+3,S^+\rangle\} \pm (\ell_2^+\ell_1^-)\{\lvert 4n+3,+\rangle\lvert J,4k+3,S^-\rangle + \lvert 4n+3,-\rangle\lvert J,4k+3,S^+\rangle\}\right]$
$A_{2g}^-/$	$\mathcal{N}\left[(\ell_1^+\ell_2^+)\{\lvert 4n+0,+\rangle\lvert J,4k+0,S^-\rangle - \lvert 4n+0,-\rangle\lvert J,4k+0,S^+\rangle\} \pm (\ell_2^+\ell_1^+)\{\lvert 4n+0,+\rangle\lvert J,4k+0,S^-\rangle + \lvert 4n+0,-\rangle\lvert J,4k+0,S^+\rangle\}\right]$
B_{1u}^-	$\mathcal{N}\left[(\ell_1^-\ell_2^-)\{\lvert 4n+2,+\rangle\lvert J,4k+0,S^-\rangle - \lvert 4n+2,-\rangle\lvert J,4k+0,S^+\rangle\} \pm (\ell_2^-\ell_1^-)\{\lvert 4n+2,+\rangle\lvert J,4k+0,S^-\rangle + \lvert 4n+2,-\rangle\lvert J,4k+0,S^+\rangle\}\right]$
	$\mathcal{N}\left[(\ell_1^+\ell_2^+)\{\lvert 4n+2,+\rangle\lvert J,4k+2,S^-\rangle - \lvert 4n+2,-\rangle\lvert J,4k+2,S^+\rangle\} \pm (\ell_2^+\ell_1^+)\{\lvert 4n+2,+\rangle\lvert J,4k+2,S^-\rangle + \lvert 4n+2,-\rangle\lvert J,4k+2,S^+\rangle\}\right]$
	$\mathcal{N}\left[(\ell_1^-\ell_2^-)\{\lvert 4n+0,+\rangle\lvert J,4k+2,S^-\rangle - \lvert 4n+0,-\rangle\lvert J,4k+2,S^+\rangle\} \pm (\ell_2^-\ell_1^-)\{\lvert 4n+0,+\rangle\lvert J,4k+2,S^-\rangle + \lvert 4n+0,-\rangle\lvert J,4k+2,S^+\rangle\}\right]$
	$\mathcal{N}\left[(\ell_1^-\ell_2^+)\{\lvert 4n+1,+\rangle\lvert J,4k+1,S^+\rangle + \lvert 4n+1,-\rangle\lvert J,4k+1,S^-\rangle\} \pm (\ell_2^+\ell_1^-)\{\lvert 4n+1,+\rangle\lvert J,4k+1,S^+\rangle - \lvert 4n+1,-\rangle\lvert J,4k+1,S^-\rangle\}\right]$
	$\mathcal{N}\left[(\ell_1^+\ell_2^-)\{\lvert 4n+3,+\rangle\lvert J,4k+1,S^+\rangle + \lvert 4n+3,-\rangle\lvert J,4k+1,S^-\rangle\} \pm (\ell_2^-\ell_1^+)\{\lvert 4n+3,+\rangle\lvert J,4k+1,S^+\rangle - \lvert 4n+3,-\rangle\lvert J,4k+1,S^-\rangle\}\right]$
	$\mathcal{N}\left[(\ell_1^+\ell_2^-)\{\lvert 4n+1,+\rangle\lvert J,4k+3,S^+\rangle + \lvert 4n+1,-\rangle\lvert J,4k+3,S^-\rangle\} \pm (\ell_2^-\ell_1^+)\{\lvert 4n+1,+\rangle\lvert J,4k+3,S^+\rangle - \lvert 4n+1,-\rangle\lvert J,4k+3,S^-\rangle\}\right]$
	$\mathcal{N}\left[(\ell_1^-\ell_2^+)\{\lvert 4n+3,+\rangle\lvert J,4k+3,S^+\rangle + \lvert 4n+3,-\rangle\lvert J,4k+3,S^-\rangle\} \pm (\ell_2^+\ell_1^-)\{\lvert 4n+3,+\rangle\lvert J,4k+3,S^+\rangle - \lvert 4n+3,-\rangle\lvert J,4k+3,S^-\rangle\}\right]$

the limits of easily available fast memory and computation time. To facilitate large basis set sizes on medium sized computers, a two-step basis set contraction scheme was used. In the first step a (3+3)D bending-torsion-rotation calculation was performed, excluding the r_3 stretch. The lowest eigenfunctions of this calculation are then used to perform a full (4+3)D calculation by forming a direct product basis of these bending-torsion-rotation functions and r_3 HO-DVR functions. This procedure reduces the largest required basis set size to only $\sim (2J+1)10^4$.

3.2.3 Potential Energy Operator

Calculating the nuclear potential energy operator requires two steps: (i) calculating a set of grid points of the potential energy surface (PES), $V(r_3, \beta_1, \beta_2, \alpha)$, and (ii) calculating integrals of this surface with the vibrational basis functions.

Our PES was generated by calculating the electronic and nuclear repulsion energy of the S_1 state over a domain of nuclear configurations spanning $r_3 = [1.30\ \text{Å} : 0.02\ \text{Å} : 1.40\ \text{Å}]$, $\beta_1, \beta_2 = [10° : 20° : 110°]$, and $\alpha = [0° : 10° : 90°]$. The quantum chemistry was performed at the EOM-CCSDT level of theory using the CFOUR package [32]. Such a high level of theory is necessary to generate accurate energies for non-planar geometries, where triple excitations become important. This coarsely sampled raw grid was then interpolated with cubic splines to create a 10° β_1, β_2 spacing and a 5° α spacing. From this surface, the β domains were extended from 110° to 180° with a linear interpolation to a sufficiently high energy arbitrarily assigned to the $\beta = 180°$ geometries (when the H atoms fold completely back onto the CC bond). This crude extrapolation has little effect on the rovibrational energies of the states of interest, as these high energy regions are completely inaccessible. For the initial (3+3)D bending-torsion-rotation calculation required for the basis set contraction, the minimum of this surface along r_3 at each $(\beta_1, \beta_2, \alpha)$ point was taken as an crudely adiabatically relaxed approximation. To generate the r_3 HO-DVR points for the full (4+3)D calculation, the r_3 dimension at each $(\beta_1, \beta_2, \alpha)$ point was fit to a Morse potential curve, which was evaluated at the r_3 HO-DVR grid points. The Morse potential fits were quite good, with residuals less than 1 cm^{-1} in the most accessible regions of the PES.

In order to calculate matrix element integrals of this surface, it is most convenient to represent it as an expansion in terms that are separable in the internal coordinates, so that only one-dimensional integrals need to be evaluated. Since the r_3 dimension is being represented by a DVR basis, its integrals are trivial (equaling the value of the PES at the DVR grid point), which leaves only $(\beta_1, \beta_2, \alpha)$ integrals to be performed over the 3D slice at each r_3 grid point. To calculate these integrals, each of these 3D surfaces is expanded with totally symmetric bending-torsion product functions as

$$V(r_3; \beta_1, \beta_2, \alpha) = \sum_{\ell_1, \ell_2, n} \left\{ c_{\ell_1 \ell_2, 4n} (\ell_1^+ \ell_2^+) \cos[4n\alpha] + c_{\ell_1 \ell_2, 4n+2} (\ell_1^- \ell_2^-) \cos[(4n+2)\alpha] \right\} \tag{3.7}$$

where $c_{\ell_1 \ell_2, n} = c_{\ell_2 \ell_1, n}$ by $\beta_1 \leftrightarrow \beta_2$ permutation symmetry. This expansion can be fit to the calculated grid via a linear least-squares procedure. Typically, the Legendre polynomial orders are chosen to be $m_1 = m_2 = 0$. The maximum values of ℓ_1, ℓ_2, and n are chosen to saturate the degrees of freedom in the fit (for example, if there are 19 points in each dimension, the fit would be performed with $\ell_1 = [0 : 1 : 18]$, $\ell_2 = [0 : 1 : 18]$, and $n = [0 : 1 : 18]$). It is important to note that if these 3D surfaces contain sharp gradients as a function of the bending or torsional coordinates, then the least squares fit might introduce detrimental ringing artifacts into the expansion. However, as the 3D surfaces corresponding to physical r_3 slices, they are generally quite smooth and lead to no such artifacts. This is one major advantage of an r_3 DVR basis, other than trivial potential surface integrals along that dimension.

Evaluation of potential surface integrals now requires summing these expansion coefficients with products of one-dimensional "triple product" integrals of the bending and torsional basis functions. The torsional integrals can be done trivially and analytically owing to simple trigonometric product rules. The triple Legendre integrals in some cases have analytic expressions, but often must be computed numerically. We generated pre-computed tables of such integrals to sufficient precision using Gauss-Legendre quadrature with the GNU Scientific Library (GSL) [33].

3.2.4 Kinetic Energy Operator

The kinetic energy operator (KEO) represents the most algebraically complicated aspect of rovibrational variational calculations. Its derivation often requires considerable effort in order to generate analytic expressions for the multitude of differential terms. The choice of internal coordinates, useful for compact descriptions of potential energy surfaces, complicates the transformation of the KEO from its trivial form in Cartesian coordinates. Accurate internal coordinate KEOs have been available for tetratomic molecules for over two decades [34, 35]. One complicating factor is that a new KEO must be derived for every choice of internal coordinates and body-fixed frame embedding. Valence bond internal coordinates are a common choice and the purely vibrational KEO terms in these coordinates are well known [36, 37]. The choice of body-fixed frames is, however, less standard and for every choice the rovibrational and rotational KEO terms must be rederived. Following the methods of Refs. [38] and [39], we have derived the vibrational, rovibrational, and rotational coupling coefficients necessary for the calculation of an analytic tetratomic KEO for our specific case of internal coordinates and body-fixed frame embedding. Tables of these coefficients are included for reference in Appendix A.

When carrying out reduced dimension variational calculations it is common practice to simply ignore terms in the full dimensional KEO that contain derivatives with respect to the constrained variables (which for this calculation are the two CH stretches). It is known, however, that this leads to the *incorrect* KEO for the constrained, reduced dimension problem [40, 41]. Following the methods of Ref. [40], we have derived the correct internal coordinate KEO suitable for two frozen CH bond lengths. We reproduce this KEO fully in Appendix A.

Matrix elements of the KEO are simplied by the fact that each term is separable in the internal coordinates so that, as with the potential energy operator, only one-dimensional integrals need be calculated. Those of the torsional and rotational degrees of freedom can be determined analytically with simple trigonometric and symmetric top algebra. The phase choice for the symmetrized rotational basis functions ensures

that their matrix elements are purely real (as opposed to the standard Condon-Shortley phase convention which results in complex-valued matrix elements). The bending integrals require more care. As with the triple Legendre integrals, analytic expressions exist for a subset of the KEO integrals. However, we took the approach of numerically calculating matrix elements of a handful of key primitive bending operators and deriving the rest from these based on well known recursion relations between associated Legendre polynomials and their first and second derivatives.

One subset of the bending KEO operators requires special discussion. Examination of the KEO will reveal that there exist some terms which may lead to divergent integrals. For example, one is proportional to $\csc^2\beta_1(\partial_\alpha - iJ_z/\hbar)^2$. The factor of $|\sin\beta_1|$ in the integration volume element is not sufficient to cancel the $\csc^2\beta_1$ divergence. For $m_1 > 0$ associated Legendre polynomials, the $\sin_1^m\beta_1$ factor in the basis function will take care of the remaining divergence, but for $m_1 = 0$ basis functions the integral will diverge unless the $(\partial_\alpha - iJ_z/\hbar)^2$ factor is itself zero. In fact, *every* divergent KEO term is paired with this or a similar torsion-rotation operator (either $(\partial_\alpha \pm iJ_z/\hbar)$ or $(\partial_\alpha \pm iJ_z/\hbar)^2$). This systematic association will form the basis of the rules cited above by which the appropriate values of m_1 and m_2 are determined based on the values of the torsional and rotational quantum numbers n and k. To be more explicit, let us consider the action of a divergent operator on a symmetrized bending-torsion-rotational basis function (i.e. those from Table 3.1). We first provide two useful relations involving the torsional and rotational basis functions:

$$\frac{i\hat{J}_z}{\hbar}|Jk,\pm(-1)^J\rangle = \mp k|Jk,\mp(-1)^J\rangle \tag{3.8}$$

$$\partial_\alpha|n,\pm\rangle = \mp n|n,\mp\rangle \tag{3.9}$$

From these we can derive the action of $(\partial_\alpha \pm iJ_z/\hbar)$ and $(\partial_\alpha \pm iJ_z/\hbar)^2$ on the general

symmetrized expression:

$$\left(\partial_\alpha \pm' \frac{i\hat{J}_z}{\hbar}\right)|\psi^{btr}\rangle =$$
$$+\mathcal{N}\left[(n \mp' k)(\ell_1^{s_1}\ell_2^{s_2})\{-s_t|n,-s_t\rangle|Jk,s_k(-1)^J\rangle + s_k|n,s_t\rangle|Jk,-s_k(-1)^J\rangle\}\right.$$
$$\left.\pm(n \pm' k)(\ell_2^{s_2}\ell_1^{s_1})\{-s_t|n,-s_t\rangle|Jk,s_k(-1)^J\rangle - s_k|n,s_t\rangle|Jk,-s_k(-1)^J\rangle\}\right] \quad (3.10)$$

$$\left(\partial_\alpha \pm' \frac{i\hat{J}_z}{\hbar}\right)^2|\psi^{btr}\rangle =$$
$$-\mathcal{N}\left[(n \mp' k)^2(\ell_1^{s_1}\ell_2^{s_2})\{|n,s_t\rangle|Jk,s_k(-1)^J\rangle + s_t s_k|n,-s_t\rangle|Jk,-s_k(-1)^J\rangle\}\right.$$
$$\left.\pm(n \pm' k)^2(\ell_2^{s_2}\ell_1^{s_1})\{|n,s_t\rangle|Jk,s_k(-1)^J\rangle - s_t s_k|n,-s_t\rangle|Jk,-s_k(-1)^J\rangle\}\right] \quad (3.11)$$

Inspection of divergent terms in the KEO shows that divergent integrands involving β_1 occur with $(\partial_\alpha - iJ_z/\hbar)$ or $(\partial_\alpha - iJ_z/\hbar)^2$, while divergent integrands involving β_2 occur with $(\partial_\alpha + iJ_z/\hbar)$ or $(\partial_\alpha + iJ_z/\hbar)^2$. Thus, owing to relations 3.10 and 3.11, every divergent integrand (be it with β_1 or β_2 operators) with an associated Legendre polynomial of order m_1 has a factor of $(k+n)$ or $(k+n)^2$ and every integrand with an associated Legendre polynomial of order m_2 has a factor of $(k-n)$ or $(k-n)^2$. Thus, we arrive at the previously quoted rules determining the appropriate values of m_1 and m_2:

$$m_1 = 0 \text{ if } k+n=0, \text{ otherwise } m_1 = \begin{cases} 1, & |k+n|/2 = odd \\ 2, & |k+n|/2 = even \end{cases} \quad (3.12)$$

$$m_2 = 0 \text{ if } k-n=0, \text{ otherwise } m_2 = \begin{cases} 1, & |k-n|/2 = odd \\ 2, & |k-n|/2 = even \end{cases} \quad (3.13)$$

Essentially equivalent rules have been derived previously for similar bending-torsion-rotation bases [35, 42] (for a mathematical discussion of the choices for nonzero values of $m_{1,2}$, see especially Ref. [42]). However, in those treatments, KEO divergences were typically viewed from a purely mathematical perspective.

There is, in fact, a simple physical picture behind the nature of these divergences. The astute reader will have noticed that our choice of bending-torsion-rotation basis functions can be directly related to spherical harmonic basis functions describing the local bending motions of each CCH bend (the associated Legendre polynomials of the bending angles form the azimuthal factors, while combinations of the torsional and χ factor of the symmetric top functions form the polar factors). The relation between m_1 and $(k+n)$ and that between m_2 and $(k-n)$ can now be seen as representing the local angular momentum of each CCH bond rotating about the CC bond axis. In fact the $(\partial_\alpha \pm iJ_z/\hbar)$ operators correspond *exactly* to local bend angular momentum operators (see Figure 3-2). Rotation of the entire molecule (quantized by k) generates

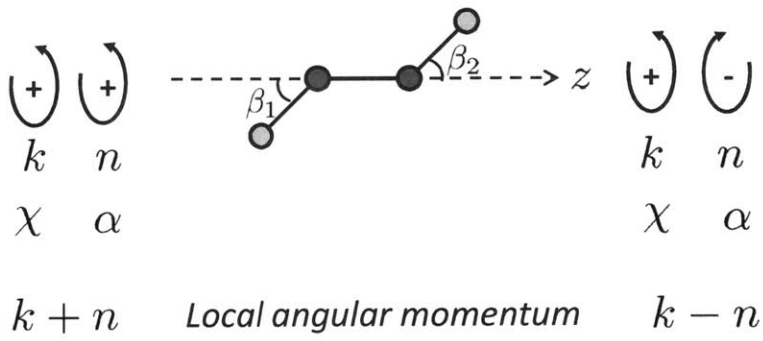

Figure 3-2: Local bond angular momentum. Body frame rotation (quantized by k) and torsional rotation (quantized by n) add constructively and destructively to generate local bond angular momentum for H_1 and H_2, respectively, about the molecular z-axis. The local bond picture provides a physical interpretation of the divergent KEO terms and the rules determining the values of the associated Legendre polynomial orders.

local bond angular momentum for both CCH bonds in the same direction. Torsional rotation (quantized by n) generates local angular momentum in opposite directions. Thus, the total local angular momentum for one CCH bond is $k+n$ and $k-n$ for the other. Just as in spherical harmonics, the quantum number m is zero when there is zero angular momentum about the z axis. This is exactly the case for our bending-torsion-rotation basis functions. Whether k and n add for one bond and subtract for the other or vice versa is a matter of phase convention implicit in the phases of the rotational and torsional wavefunctions (which can be determined by the action of ∂_α

and $iJ_z/\hbar$, see Eq. 3.8).

3.3 Results

3.3.1 Details of the Calculations

Before we examine the global structure and patterns of the calculated rovibrational levels, we will discuss various technical details including basis set sizes, level convergence, and accuracy benchmarks of each of the fundamental vibrations. The (4+3)D Hamiltonian is factored into blocks distinguished by their $G_4^{(8)}$ symmetry and total angular momentum J. For each block in the initial bending-torsion-rotation calculation, we used functions from Table 3.2 with $\ell_1 + \ell_2 \leq 30$, $n \leq 63$, and $k \leq J$ for $J = 0, 1, 2$. The corresponding total number of bending-torsional-rotation basis functions for each of these blocks is given in Table 3.3. The absolute convergence error of the lowest eigenvalues of these basis sets is < 0.1 cm^{-1}. Relative energies are converged to at least another order of magnitude. For the highest states of interest, lying around 5000 cm^{-1} above the *trans* zero-point energy, the absolute convergence errors are estimated to be on the order of 1 cm^{-1}.

Table 3.3: Bending-torsion-rotation basis set sizes. Each entry is the total number of basis functions for a given $G_4^{(8)}$ symmetry and J block. These basis sets correspond to the limits $\ell_1 + \ell_2 \leq 30$, $n \leq 63$, and $k \leq J$

J	A_{1g}^+	A_{2g}	B_{2u}^+	B_{1u}^-	Total
0	6 796	6 090	6 330	6 540	25 756
1	19 141	19 847	19 591	19 381	77 960
2	32 702	31 996	32 221	32 431	129 350
					233 066

As a means of evaluating the quality of our potential surface and the accuracy of our methods, we compare the observed and calculated fundamental frequencies for

Table 3.4: Observed and calculated *trans* and *cis* fundamental frequencies. All energies are in cm^{-1}. Three calculated columns are included: the initial 3D bending-torsion-rotation calculation (left), a full 4D calculation including r_3 using the full dimensional KEO (center), and a full 4D calculation using a correctly constrained KEO for frozen r_{CH} bond lengths (right).

Mode	Obs.	3D	4D w/ full dim. KEO	4D w/ constr. KEO
trans				
ν_2 (r_{CC} stretch)	1387 [10]	–	1443	1387
ν_3 (*trans* bend)	1048 [10]	1109	1074	1071
ν_4 (torsion)	765 [14]	764	762†	749
ν_6 (*cis* bend)	768 [14]	770	769†	774
cis				
ν_2 (r_{CC} stretch)	1503*	–	–	1514
ν_3 (*cis* bend)	740 ± 10 [17]	783	776	764
ν_4 (torsion)	865 ± 10 [17]	865	861†	844
ν_6 (*trans* bend)	585*	618	615†	593

* These fundamentals have not been observed. We instead quote recent VPT2 calculations [16] for comparison.

† These "4D" values for ν_4 and ν_6 were calculated on a 3D grid adiabatized along the r_3 coordinate.

the *trans* and *cis* conformers in Table 3.4. Only the modes spanned in our reduced dimensional internal coordinate space (ν_2, ν_3, ν_4, and ν_6 of each conformer) are included. Some fundamental frequencies of the *cis* conformer have yet to be observed. In these cases, we use calculated fundamentals from recent VPT2/anharmonic force field calculations [16] to provide some point of comparison. As that type of calculation is of quite a different nature than a variational approach, agreement would seem to indicate that the results are a faithful representation of the potential surface.

Examining the *trans* modes, for which all experimental fundamentals are known, it is clear that the 3D bending-torsion-rotation calculation is sufficient to describe the low frequency stretches, but fails to accurately reproduce the *trans* bending mode. The residual for this mode is significantly reduced by the addition of the r_3 stretch, which is consistent with normal mode analyses that show a non-negligible contribution of r_3 to the ν_3 mode. The CC stretching mode ν_2 treated with a full dimensional KEO shows a considerably large residual. This is at first unexpected as ν_2 is spanned almost exclusively by r_3 and therefore the current dimension reduction should treat this mode well.

The source of the discrepancy can be traced to the incorrect use of an unconstrained, full dimensional KEO. As is often done when using a full dimensional KEO in a reduced dimension calculation, the only change made to the KEO is to ignore terms with derivatives with respect to frozen coordinates. We expect the kinetic energy of the r_3 stretch to be determined by the KEO term involving its second derivative. In our case, this leaves the following term

$$\frac{-\hbar^2}{2\mu_{CC}}\frac{\partial^2}{\partial r_3^2}, \tag{3.14}$$

which indicates that the effective reduced mass of the r_3 stretch is equal to μ_{CC}, i.e. the KEO treats the r_3 stretch as occuring between two carbon atom masses, as opposed to two CH fragments which is intuitively what we would expect. In fact, replacing the carbor-carbon reduced mass, μ_{CC}, with a CH dimer reduced mass, $\mu_{CH,CH} = (m_C + m_H)/2 \approx (13/12)\mu_{CC}$, should lower the stretch frequency by $\sim$

$\sqrt{12/13}$. Scaling the calculated full dimensional KEO frequency of 1443 cm^{-1} by this ratio yields 1386 cm^{-1}, almost exactly the observed ν_2 frequency. This suggests that, indeed, the full dimensional KEO incorrectly treats reduced masses (amongst other details) when naïvely applied to reduced dimension systems. The corresponding second derivative term in the constrained KEO (see Appendix A) equals

$$\frac{-\hbar^2}{2}\left[\frac{1}{\mu_{CC}} - \frac{\mu_{CH}}{m_C^2}\left(\cos^2\beta_1 + \cos^2\beta_2\right)\right]\frac{\partial^2}{\partial r_3^2} \tag{3.15}$$

According to this expression, the effective r_3 stretching mass is geometry dependent. At linear geometries ($\beta_1 = \beta_2 = 0$), the mass factor is exactly the inverse CH dimer reduced mass, as expected. When $\beta_1 = \beta_2 = 90°$, both cosine terms are zero and the effective mass is that of two carbon atoms. At other geometries, the effective mass is at some intermediate value.

The calculated fundamental frequencies using the constrained KEO are shown in the right-most column of Table 3.4. The ν_2 frequency clearly improves, matching the observed value to within 1 cm^{-1}. The low frequency bends, ν_4 and ν_6, actually worsen. This is most likely due to the more sparsely sampled 4D PES grid. Ongoing calculations with improved sampling around the equilibrium geometries are expected to correct for this issue. It will be seen, however, that these small errors in the fundamental frequencies have relatively little effect on the calculated structure of high lying overtones and combination bands of ν_4 and ν_6.

3.3.2 Bending Polyads and the Onset of Isomerization

A complete, assigned $J = 0$ level list of predicted vibrational states from the *trans* origin to 5000 cm^{-1} of internal energy is included in Appendix B. It would be both tedious and mostly uninformative to compare the calculated structure to the observed levels state-by-state. We choose to focus mainly on the more complicated (read interesting) global aspects of the rovibrational structure, such as the bending polyads, and the effects due to the presence of the low barrier *cis-trans* isomerization pathway, like the decoupling of ν_3 and ν_6 combination levels from bending polyads and

K-staggerings caused by tunneling interactions. For some effects, we will examine specific, local representative cases.

An overview diagram of the observed and calculated *trans* and *cis* $J = 0$ level structure is shown in Figure 3-3. Apart from the slight overestimation of the ν_3 frequency, the overtones and combination bands involving ν_2 and ν_3 are reproduced quite well. These levels display very little interesting structure and conform to simple anharmonic oscillator energy level patterns.

The first challenge for *ab initio* calculations involves the overtones of modes ν_4 and ν_6. Errors in the calculated bending fundamental frequencies lead to some systematic offsets of the higher lying polyads. However, the *internal* structure of each polyad is reproduced with impressive accuracy. Figure 3-4 shows the observed and calculated $J = K = 0 - 2$ level structure of B^4, the polyad containing the zero-order $\{4^4, 4^3 6^1, 4^2 6^2, 4^1 6^3, 6^4\}$ vibrational states. The residuals of the calculated intrapolyad structures are about the same as experimental fits to effective Hamiltonians which include interaction parameters for Darling-Dennison resonances and a and b-axis Coriolis coupling between modes ν_4 and ν_6. Such empirical fit models are extremely useful in generating observed level patterns via physically meaningful parameters. One problem is that they often must be applied on a polyad by polyad basis, lacking a single global model. Our *ab initio* variational calculations are, in contrast, inherently global in nature and can also provide complementary physical insight into the polyad level structures. For example, one well-known result of polyad effective Hamiltonians in S_1 acetylene is that the polyad members possess approximate vibrational angular momentum. Inspection of the variational wavefunctions for the B^4 polyad clearly complements such an interpretation, as is illustrated in Figure 3-5.

In Chapter 2, it was seen that the polyad model was beginning to break down for $3^m 6^n$ combination bands due to a large ν_3/ν_6 cross anharmonicity associated with the onset of isomerization. Prior reduced dimension DVR vibrational calculations of the S_1 state [22] have shown that such levels have increasing delocalization over the *cis-trans* isomerization barrier. This thesis, by including the torsional degree of freedom, extends this result by enabling an examination of the wavefunctions for all members

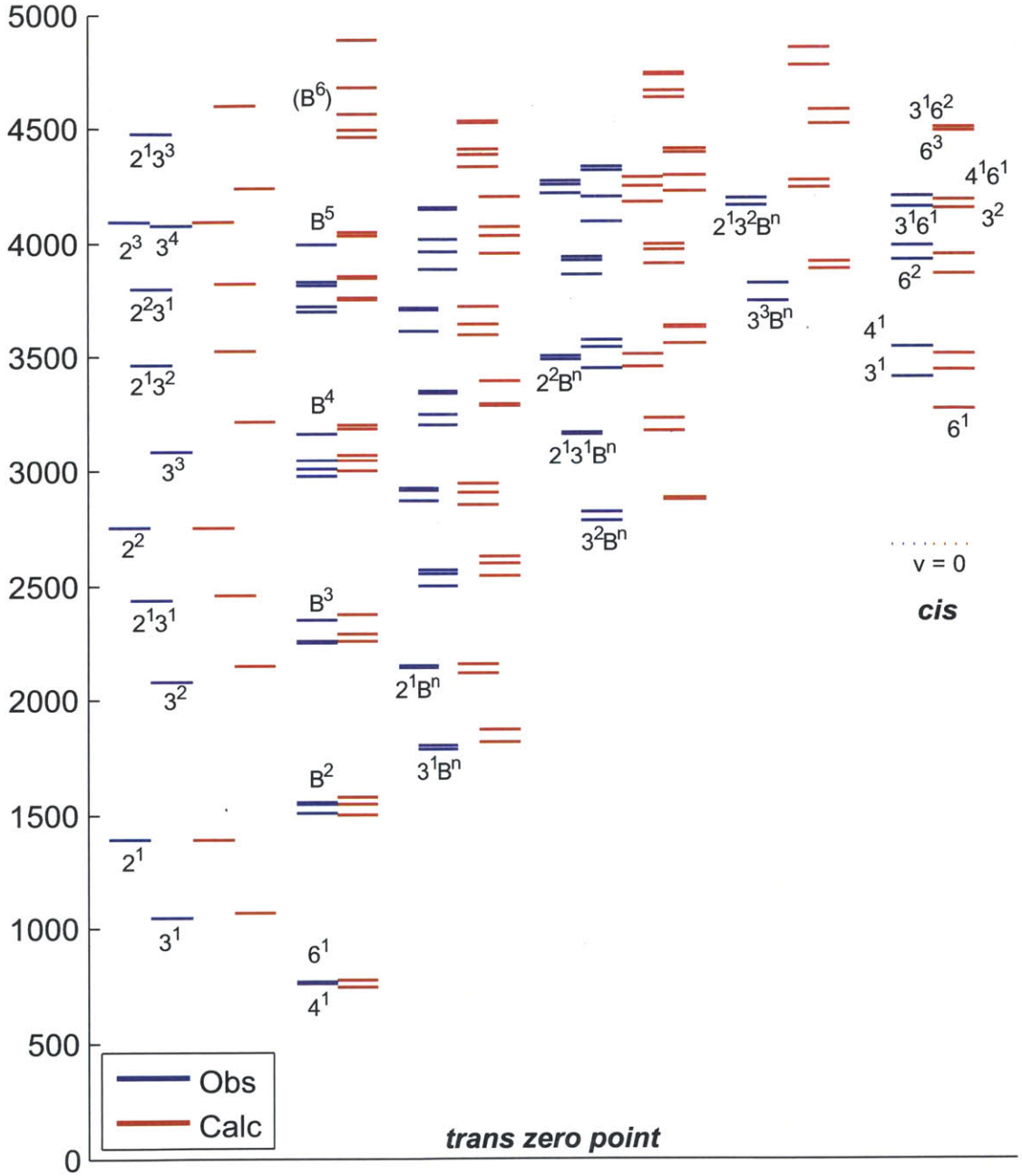

Figure 3-3: Observed and calculated S_1 vibrational levels. $J = 0$ vibrational energies are shown for almost all vibrational levels under 5000 cm^{-1} of internal energy. Assigned observed levels are shown in blue (left side of each stack). Calculated levels are in red (right side). An offset of 240 cm^{-1} was subtracted from the calculated *cis* levels such that the calculated and empirically estimated value of the *cis* $v = 0$ origin (2675 ± 10 cm^{-1} [16]) coincide.

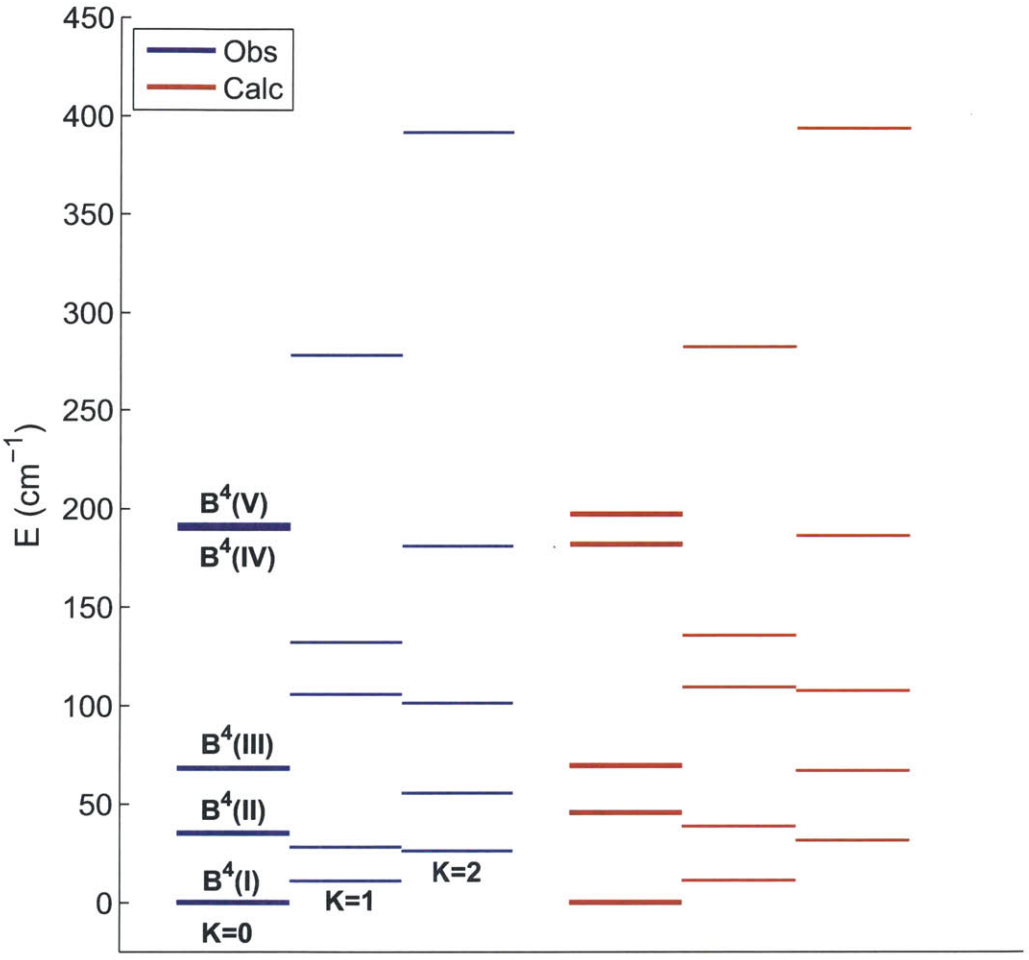

Figure 3-4: Observed (left) and calculated (right) $J = K = 0 - 2$ levels of the B^4 polyad. Not all observed levels of B^4 have been definitively assigned. In those cases, fitted values are compared [20]. The "center of gravity" of the polyad has been subtracted to compare only the *intrapolyad* structure, ignoring systematic offsets. Despite the fact that the $J = K = 0 - 2$ levels span 400 cm^{-1}, the calculated structure has an rms residual of only 4 cm^{-1}.

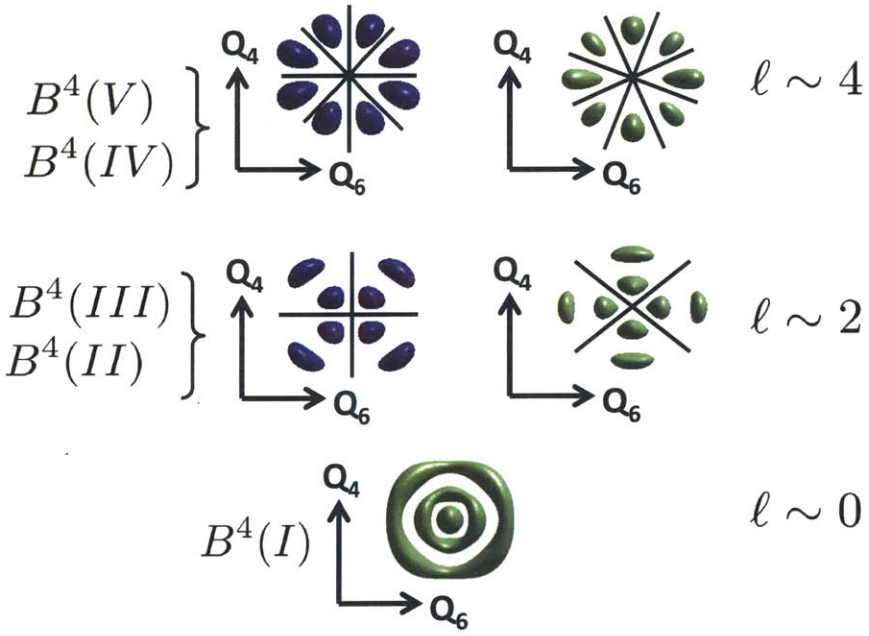

Figure 3-5: Variational wavefunctions of the B^4 polyad ($|\Psi|^2$ is plotted). The coupling between modes ν_4 and ν_6 is manifest. The angular nodal patterns (shown with solid lines) are consistent with the expected vibrational angular momentum generated in the bending polyads and allow the polyad members to be organized with an approximate vibrational angular momentum quantum number $\ell \approx 0, 2, 4$. Member states of B^4 are labeled in absolute energy order by Roman numerals.

of $3^m B^n$ polyads, among which isomerizing states are especially interesting members. Figure 3-6 compares the $\{\beta_1, \beta_2, \alpha\}$ projections of the B^4, 3^1B^4, and 3^2B^4 polyads. For the pure bending polyad, B^4, the coupled vibrational angular momentum structure is the same as that examined in Figure 3-5. The addition of one or two quanta of ν_3 begins to alter the polyad coupling patterns. The lowest member, nominally 3^n6^4, is decoupled from the remainder of the polyad. This incremental decoupling can be seen by the loss of vibrational angular momentum structure in the wavefunction and the onset of delocalization into the *cis* well, especially for 3^26^4 in the lower left plot of the figure. From the energy level patterns, this decoupling is associated with the large cross-anharmonicity of ν_3 and ν_6. The predicted size of this cross-anharmonicity is smaller than experimentally observed (for example, our predicted position for 3^16^1 is above that of 3^14^1); however, the global structure is still well reproduced.

3.3.3 *cis* Vibrational Manifold

The vibrational assignments of experimentally observed *cis* states [17, 18] have largely been guided by *ab initio* calculations [16, 22] of *cis* vibrational frequencies. To further support these assignments and establish them beyond reasonable doubt, we summarize in Table 3.5 the observed and calculated positions of the low energy *cis* manifold. Despite residuals of tens of cm^{-1} in the variational results, the level structure is sufficiently sparse to confirm the observed vibrational assignments with great certainty. It should be noted that the variational and VPT2 calculations are very different in nature. Their general agreement with one another indicates that neither set of results suffers from any significant errors. As mentioned above, the residuals in the variational predictions for the *cis* frequencies are expected to improve if a finer PES grid spacing is used around the equilibrium configuration. We also note that the variational predictions for *cis* 6^3 and *cis* 3^14^1 have led to very tentative assignments of these levels in not yet published spectra. The analysis of these spectra will be the topic of a future paper.

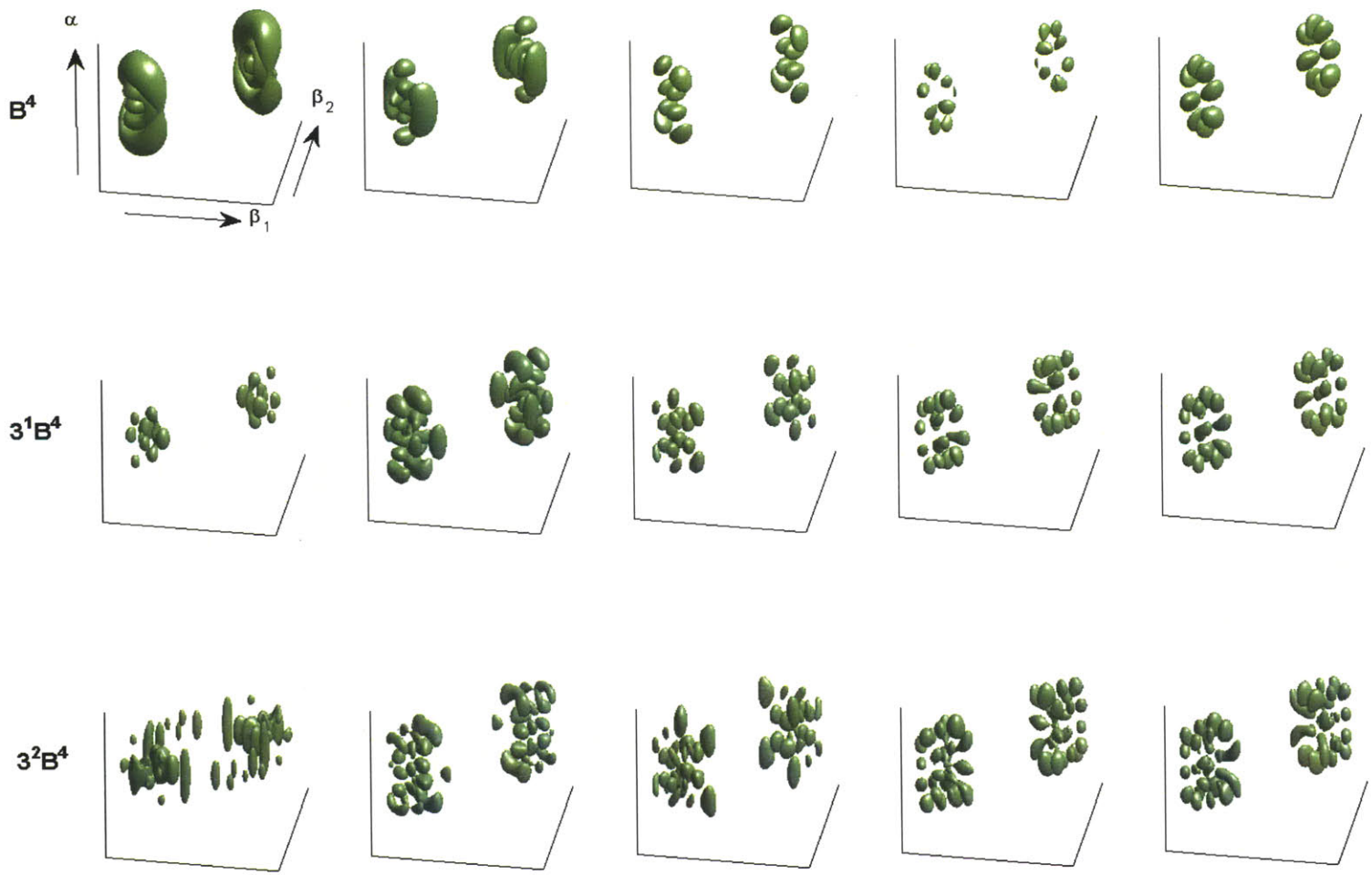

Figure 3-6: Decoupling of the $3^n B^4$ polyads. The 3D bending-torsion projection of wavefunctions for the B^4, 3^1B^4, and 3^2B^4 polyads are shown in the first, second, and third rows, respectively. The squared amplitude ($|\Psi|^2$) is plotted. Increasing quanta of ν_3 causes decoupling of the lowest member of the polyad, restoring its nominal 3^n6^4 character. 3^26^4 exhibits *cis-trans* delocalization and tunneling through the isomerization barrier.

Table 3.5: Observed and calculated positions of *cis* vibrational levels. Observed levels are reported in this work [18] and Ref. [17]. VPT2 [16] calculations are second-order vibrational perturbation theory results from a full dimensional anharmonic force field.

cis state	Obs.	Calc. (this work)	Calc. (VPT2)
$v = 0$	0	0	0*
6^1		593	607†
3^1	740	764	740*
4^1	865	834	865†
6^2	1244	1186	1244†
$3^1 6^1$	1305	1273	1294†
3^2	1477	1509	1476
2^1		1514	1503
$4^1 6^1$	1524	1467	1535†
$3^1 4^1$		1579	1572†
6^3		1815	

*The *cis* zero point has not been observed. Its value is taken to be 44870 cm^{-1} based on the VPT2 calculation of the ν_3 frequency.

†These values include a manual correction of the ν_4 and ν_6 frequencies (see Ref. [16] for details).

3.3.4 K-Staggering and Tunneling Interactions

For any molecule with low barriers between local equilibrium geometries, tunneling interactions will have an important qualitative impact on barrier-proximal states and their level structure. S_1 C_2H_2 is an especially interesting case in that there are both multiple asymmetric wells (*cis* and *trans* conformers) and multiple conceivable isomerization pathways between these wells (i.e. in-plane bending and out-of-plane torsion). Though such properties make *cis-trans* isomerization in acetylene a complicated problem, they will ultimately create patterns that reveal details about *cis-trans* interactions and the associated isomerization dynamics.

The energy regions where *cis-trans* tunneling is important can be divided into two segments. The lower energy part includes states where the tunneling interaction energies are smaller than the spacing between localized *cis* and *trans* vibrational levels. The upper energy part includes states near the top of the isomerization barrier where tunneling effects are no longer perturbative, and interactions between wells dominate the level structure. In reality, of course, there is a continuous distribution between these regimes, but this distinction will help frame the discussion of tunneling patterns.

The simplest tunneling case is a degenerate interaction between localized states in identical equilibrium wells. Figure 3-7a shows a 2D contour plot of the S_1 PES for planar geometries. The axes correspond to the two CCH bond angles $\beta_{1,2}$. The upper right and lower left quadrants contain two equivalent *cis* wells, while the upper left and lower right are *trans*. We consider localized wavefunctions in the two *cis* wells, which interact to form symmetrized tunneling components: a symmetric and antisymmetric linear combination. In Figure 3-7b, we show transformations which may be applied to such wavefunctions. For the symmetric tunneling component, moving from configuration (1) to (3) via in-plane bending (2) leaves the value of the wavefunction unchanged (with no phase change), while the antisymmetric component obtains a negative phase change. A 180° rotation about the body-fixed z-axis returns the molecule to the same space-fixed coordinates as (1), and therefore the

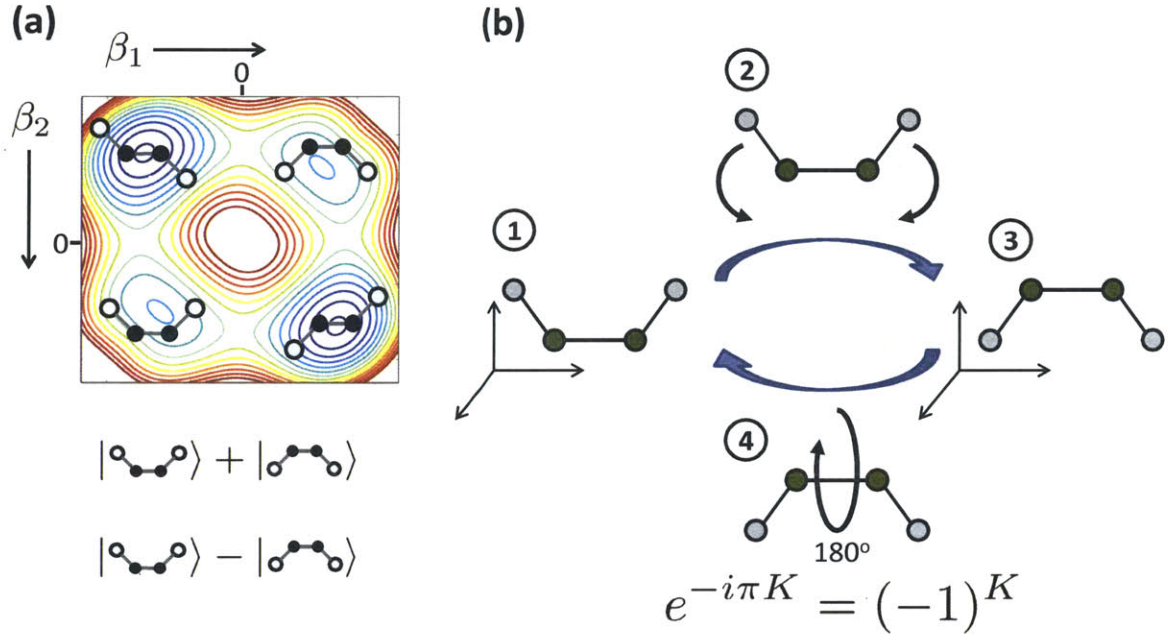

Figure 3-7: Tunneling in *cis* vibrational states. (a) 2D in-plane bending potential with two equivalent *cis* and *trans* wells. Degenerate localized wavefunctions in each equivalent well form symmetric and antisymmetric tunneling linear combinations. (b) A molecule in the lower left *cis* well (1) can isomerize via in-plane bending (2) to an equivalent *cis* well (3), which can be transformed back to the original orientation via a 180° rotation about the CC-axis (4). Requiring a single-valued wavefunction entails that symmetric tunneling components have only even K states and antisymmetric tunneling components have only odd K states.

wavefunction must return to its original value. This implies that the phase of the rotational factor of the total wavefunction must undergo no phase change for symmetric tunneling components and a negative phase change for antisymmetric components. The phase change of such a rotation about the z-axis is $\exp(-i\pi K) = (-1)^K$. Thus symmetric tunneling components can only have rotational factors with even K and antisymmetric tunneling components can only have rotational factors with odd K. Tunneling splittings (like those observed in ammonia inversion or methyl rotors) will only appear as a staggering between the even and odd K levels within a given vibrational state. Other operations that transform the molecule between equivalent wells (for example, changing the torsional coordinate $\alpha \rightarrow \alpha + \pi$) lead to additional and distinct K-staggering patterns.

The relevant extended complete nuclear permutation inversion (CNPI) group theory for treating isomerization in S_1 acetylene using the $G_4^{(8)}$ symmetry group is fully treated in Ref. [26]. It can be shown that nearest-neighbor tunneling interactions should lead to an even/odd K-staggering for in-plane isomerization. If torsional isomerization is feasible, then an additional staggering between $K = 4n$ and $K = 4n+2$ states should occur.

A summary of observed and calculated staggerings is given in Table 3.6. Because of the small number of observed *cis* levels and their respective K stacks, few K-staggering measurements have been reported. For the two experimental data points

Table 3.6: K-staggerings in *cis* vibrational states. Listed are the observed and calculated K-staggerings for several *cis* states. The limited characterization of the *cis* conformer leaves us with only two experimental measurements. The calculated values are taken from a 3D bending-torsion-rotation calculation.

State	Obs.	Calc.
cis $3^1 6^1$	+3.9 [17]	+1.6
cis 6^2	-5 ± 1 [18]	−3.0
cis $v = 0$		+0.03
cis $3^1 6^2$		+42
cis 6^3		−62

available, the predictions agree in the direction and approximate magnitude of the K-staggering. All the reported staggerings are between the even and odd K states, as no apparent staggering between $K = 0$ and 2 states has been observed (as mentioned above, this pattern would result from torsional tunneling). The K-staggering for the *cis* origin level is predicted to be quite small and we anticipate that it will not be distinguishable from other factors affecting the rotational structure. Only one bending quantum higher than the levels where staggerings have been observed, the staggerings are predicted to be an order of magnitude larger. There are two reasons this occurs. First, the simple degenerate tunneling interactions between vibrational states belonging to identical wells (i.e. *cis-cis* or *trans-trans*) become larger as the barrier width decreases. Second, resonant interactions between nearby *cis* and *trans* states emerge. These interactions are K-dependent due to the rotational dependence of the CNPI symmetry. The result is that even K and odd K components of *cis* and *trans* states interact with each other in different ways.

The patterns associated with this latter type of *cis-trans* staggering are expected to be less consistent, as the level shifts sensitively depend on the relative positions of near-resonant *cis* and *trans* states. The even and odd components essentially have to be treated as separate vibrational components (and in light of the above discussion, they in fact are separate tunneling components). When *cis-trans* interactions become important, the K-staggerings should be large enough to be noticeable in the already distorted rotational structure of *trans* vibrational states. From a perturbation theory perspective, *cis-cis* and *trans-trans* interactions between identical wells are a first-order effect, while near-resonant *cis-trans* interactions are a second-order effect.

As one example, $3^4 6^2$ is predicted to have a K-staggering of about -70 cm^{-1}. Figure 3-8 shows the vibrational wavefunctions for the $K = 0$ and 1 states. Both rotational components show extensive *cis-trans* delocalization. However, the $K = 0$ component interacts with *cis* $3^2 6^2$, and the $K = 1$ with *cis* $3^3 6^1$, leading to a large staggering between even and odd K states. These staggerings will make analysis of the near-barrier region extremely difficult, though *ab initio* predictions such as these should aid tremendously in sorting out the distorted spectral patterns.

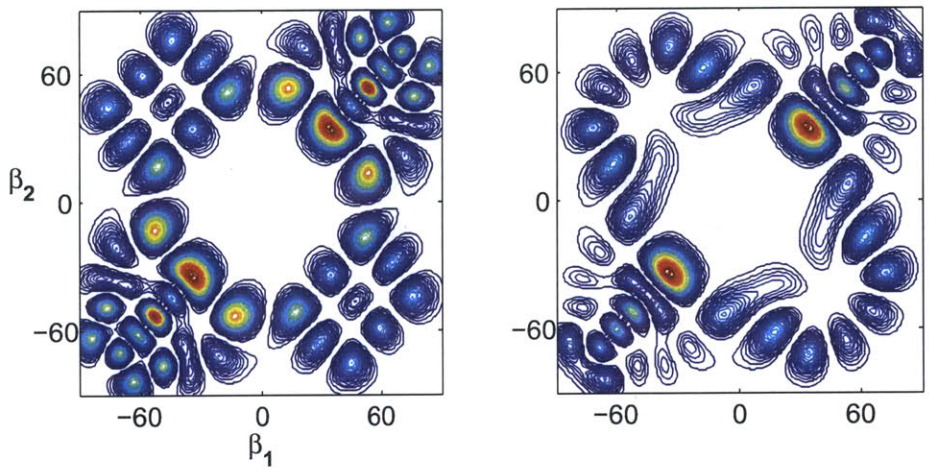

Figure 3-8: K-dependent *cis-trans* interactions in $3^4 6^2$. This figure shows the vibrational wavefunctions ($|\Psi|^2$) of the $K = 0$ (left) and $K = 1$ (right) states of $3^4 6^2$ in the $\alpha = 0$ plane (i.e. planar geometries). Both demonstrate significant *cis-trans* delocalization (the *trans* geometries are in the lower left and upper right quadrants and the *cis* geometries are in the upper left and lower right quadrants). The $K = 0$ component interacts with *cis* $3^2 6^2$, but the $K = 1$ component interacts with *cis* $3^3 6^1$. The K dependence of *cis-trans* tunneling leads to significant K-staggering for zero-order states with the same vibrational character.

3.4 Discussion

In this chapter, we have presented the highest dimension rovibrational variational calculations of S_1 acetylene to date. We have reproduced some of the most complicated aspects of this electronic state's rovibrational structure, which include the ν_4/ν_6 bending polyads, the effects of *cis-trans* isomerization on the level structure of 3^m6^n combination bands, and the presence of K-staggering in levels that tunnel through the barrier to isomerization. One strength of a variational treatment is that the entire global structure is generated with a single calculation, which allows patterns to be observed over large ranges of internal energy. Our prediction of very large K-staggerings in barrier-proximal *cis* and *trans* levels will be a significant factor in our experimental analysis and assignment of the last set of levels underneath and isoenergetic with the barrier to isomerization.

We are continuing to refine these calculations by generating a more densely sampled potential surface in the regions of configuration space containing the largest vibrational wavefunction amplitude. In addition, we are currently calculating a transition dipole surface of the $S_1 \leftarrow S_0$ transition in order to simulate excitation spectra of S_1 as well as stimulated emission [43] and dispersed fluorescence [44–46] spectra of S_0.

Exclusive attention has been paid in this chapter to the calculated rovibrational structure below and up to the barrier to isomerization. These calculations, of course, give predictions for the above-barrier rovibrational structure as well. This predicted structure, however, has yet to be analyzed. Qualitatively new level patterns will emerge resulting from unhindered large amplitude internal motions. One possiblity is the development of approximate vibrational angular momentum along the out-of-plane (c) axis. *Ab initio* calculations conducted in parallel with the analysis of high energy spectra will almost certainly prove necessary to understand the undoubtedly complicated level structure in those energy regions.

Chapter 4

Spectroscopic Characterization of Transition States

In the previous chapters, we have explored the details of *cis-trans* isomerization in S_1 acetylene from both spectroscopic and *ab initio* perspectives. We have seen that large-scale changes affect the energy level patterns of isomerizing states. Tunneling interactions lead to K-staggerings within vibrational levels and eventually K-dependent *cis-trans* interactions that can vastly distort the rovibrational structure of states along the isomerizaton path. These states also experience large anharmonicities and require models that can effectively treat large-amplitude motions and the presence of stationary points in the potential surface. In order to gain quantitative information regarding the isomerization process, we rely on spectroscopic patterns that are dependent on physically meaningful parameters. The failure of effective Hamiltonians in modeling the global *trans* manifold's level structure tells us that a qualitative change has occured and in doing so implicates the 3^n6^m levels, which are proximal to the isomerization path. Such complications, however, are an opportunity to recognize emergent spectrosopic patterns that provide quantitative information about the isomerization process. In this chapter, we propose a general empirical model that enables direct spectroscopic characterization of the essential aspects of isomerization: the energy of transition states and isomerization barriers and the topography and shape of isomerization paths.

4.1 Effective Frequency "Dips"

It has been mentioned several times that the 3^n6^m combination levels display an unusually large cross-anharmonicity related to the approach to the geometric structure of the half-linear isomerization transition state. To illustrate this point explicitly, we reproduce in Figure 4-1 the spectra of the the 3^nB^2 polyads, for $n = 0 - 3$. In a

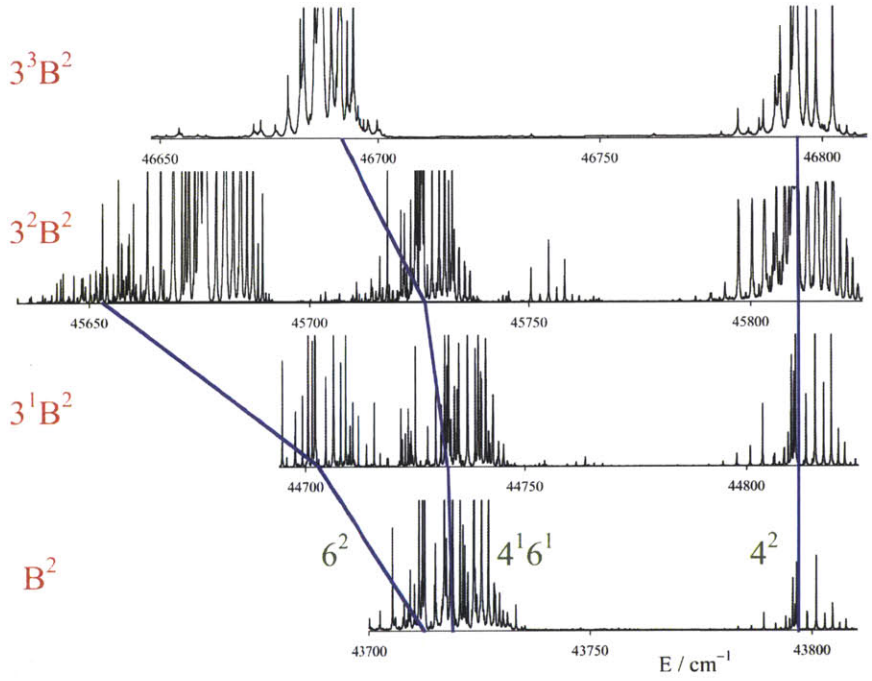

Figure 4-1: ν_3/ν_6 anharmonicity in the 3^nB^2 polyads (reproduced from Figure 13 of Ref. [21]). The intrapolyad structure of B^2 should normally be transplantable to higher combinations with ν_3. However, observed polyads show a drastic fallout of the lowest member (nominally 3^n6^2) associated with the approach to the isomerization half-linear transition state.

normal case, the B^2 polyad structure should be able to be transplanted directly to higher lying 3^nB^2 combination polyads. The observed structure, however, shows a drastic fallout of the lowest polyad member, which has nominal 3^n6^2 character. As seen in the previous chapter, this nominal character becomes quite dominant when both ν_3 and ν_6 are highly excited and the vibrational state approaches the shape of the half-linear transition state.

The nature of this fallout can be appreciated by considering semiclassically the

motion of a body in a potential that contains a stationary point (or transition state) between two wells. Such a 1D potential is given in Figure 4-2a. This toy potential

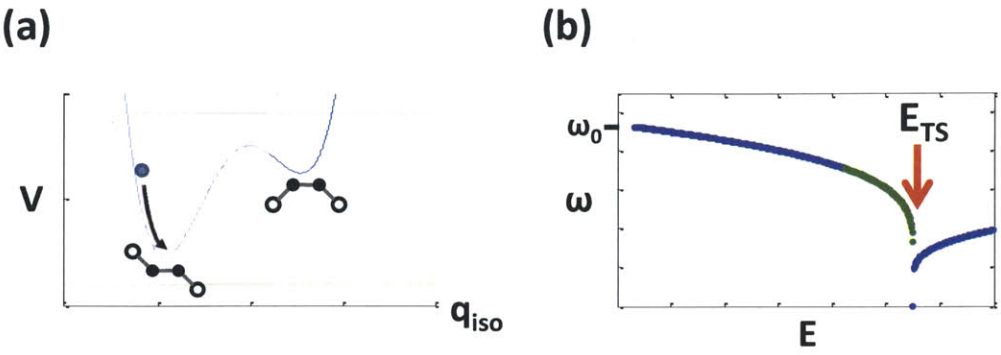

Figure 4-2: Classical frequency "dip" at a potential surface stationary point. (a) A 1D potential of *cis-trans* isomerization. The isomerization coordinate, q_{iso}, corresponds to a CCH bending angle. A stationary point on the potential surface occurs at the half linear transition state. The frequency of periodic motion of a classical body in the *trans* well is plotted in (b) as a function of the total energy. At low energies, the body oscillates with harmonic frequency ω_0 near the bottom of the well. When the body has total energy equal to the energy of the barrier, its classical frequency goes to zero because it must have zero kinetic energy when it reaches the transition state stationary point, thus stopping at that position. The classical frequency evolves smoothly from the zero-energy harmonic motion to zero-frequency motion at the stationary point, creating a "dip" in the classical frequency curve at exactly the barrier height. An identical dependence occurs for motion in the *cis* minimum.

corresponds to a 1D cut along the S_1 potential. The isomerization coordinate is the local CCH bending angle. A stationary point between the *trans* and *cis* minima occurs at the half-linear transition state. We consider the classical periodic trajectories of a body moving in this potential. Imagine letting a ball roll in the *trans* well with a given amount of total energy E and measuring its periodic frequency (as plotted in Figure 4-2b). At low energies, the ball will move harmonically with frequency ω_0, which depends on the curvature of the potential well. As the total energy increases, anharmonic effects will begin to decrease the frequency. When the ball's total energy is equal to that of the stationary point it will have zero kinetic energy when it reaches the transition state and stop at the top of the barrier. The classical frequency is thus zero at the energy of the barrier. The continuous classical frequency curve $\omega(E)$,

which begins at $\omega(0) = \omega_0$, will smoothly dip to $\omega(E_{ts}) = 0$. When the total energy increases above the energy of the barrier, the frequency will rise again. The shape of the rise depends on shape of the outer walls of the potential.

A result of semiclassical quantization is that classical frequencies correspond to quantized level spacings, i.e. $\omega(E) \sim \Delta E(E)$, where $\Delta E(E)$ is the *effective frequency* or energy spacing between consecutive energy levels at average energy E. As with classical motion, the effective frequency will dip at the energy of the stationary point. Due to finite sampling of a discretely quantized system, the dip cannot reach zero, but will tend to zero.

Such an effect is historically well-known in triatomic spectroscopic literature. Quasi-linear triatomics are bent molecules with a low barrier to linearity, where a saddle point occurs along the bending coordinate. Experimental spectra and model potentials of highly excited bent triatomics were analyzed nearly fifty years by Dixon [47], who showed that an effective frequency dip occurs at the energy of the barrier to linearity (see Figures 3 and 5 of Ref. [47]). However, it appears that the connection between the quantized effective frequency dip and classical motion with zero kinetic energy at the stationary point was not recognized. Such ideas have since not been widely applied to larger systems, if at all, perhaps due to the difficulty in generating comprehensive assignments of vibrationally excited regions. S_1 acetylene, where the *trans* vibrational manifold is completely assigned nearly to the predicted transition state energy, is an opportune test case for generalizing the effective frequency dip.

4.2 Fitting the Effective Frequency Curve

In Figure 4-3, we plot effective frequency dips for the quantized version of the *ab initio* 1D potential from Figure 4-2a as well as the experimental progression 3^n6^2 (where both the effective ν_3 and ν_6 frequencies are plotted). The experimental effective ν_3 and ν_6 frequency curves lie above and below the *ab initio* 1D curve, which is consistent with the 1D isomerization coordinate being a direct combination of the ν_3 and ν_6

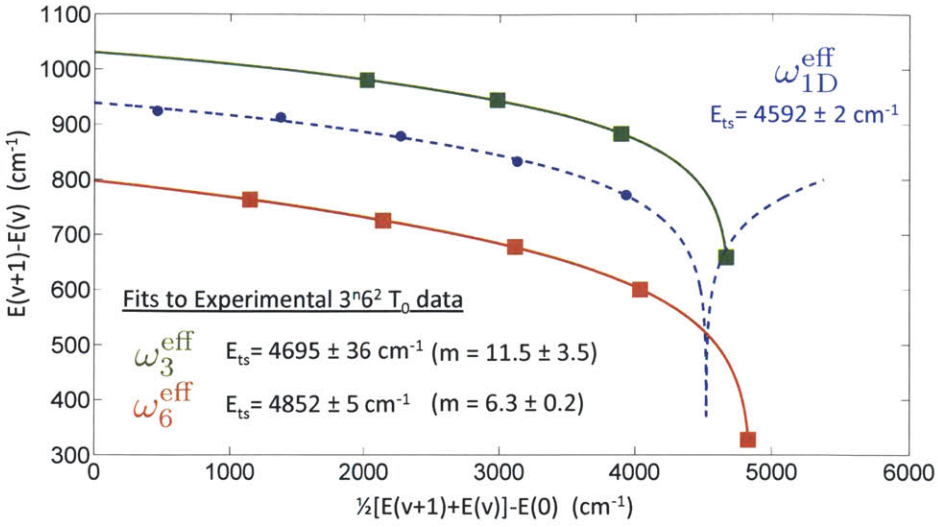

Figure 4-3: Effective frequency dips in isomerizing *trans* acetylene. The blue dashed line corresponds to a 1D CCH bending isomerization potential (as shown in Figure 4-2a). The solid curves are the effective ν_3 and ν_6 frequencies from experimental measurements of the 3^n6^2 progression. The model fit function, discussed in the text, directly predicts values for the height of the isomerization barrier E_{ts}.

normal modes. In order to determine the energy of the isomerization transition state from the experimental measurements, the effective frequency curves must be fit to an empirical model. We propose the following dependence of effective frequency with vibrational energy

$$\Delta E(E) = \omega_{eff}(E) = \omega_0 \left(1 - \frac{E}{E_{ts}}\right)^{1/m}, \tag{4.1}$$

where ω_0 is the zero-energy harmonic frequency, E_{ts} is the energy of the isomerization barrier, and m is a shape parameter. This expression is first and foremost an empirical model; however, it is motivated by having the correct physical limits. $\omega_{eff}(E = 0)$ evaluates to ω_0, the harmonic frequency, while $\omega_{eff}(E = E_{ts}) = 0$, in correspondence with the classical frequency dependence. These limits are unchanged by the value of the shape parameter m, which determines how steeply the effective frequency dips from ω_0 to zero. One desirable feature of the effective frequency dip expression is how simply and directly it depends on physical quantities of interest, like the equilibrium

harmonic frequency and the transition state energy. In fact, the m parameter encodes qualitative information about the isomerization path as well. In Figure 4-4a, we give the effective frequency dip curves for various values of m. Using standard RKR-type spectral inversion methods, we can invert the effective frequency curve to generate an equivalent 1D potential, shown in Figure 4-4b. The spectral inversion only generates the potential up to the energy of the barrier and only from the side of the barrier for which the effective frequency curve is taken.

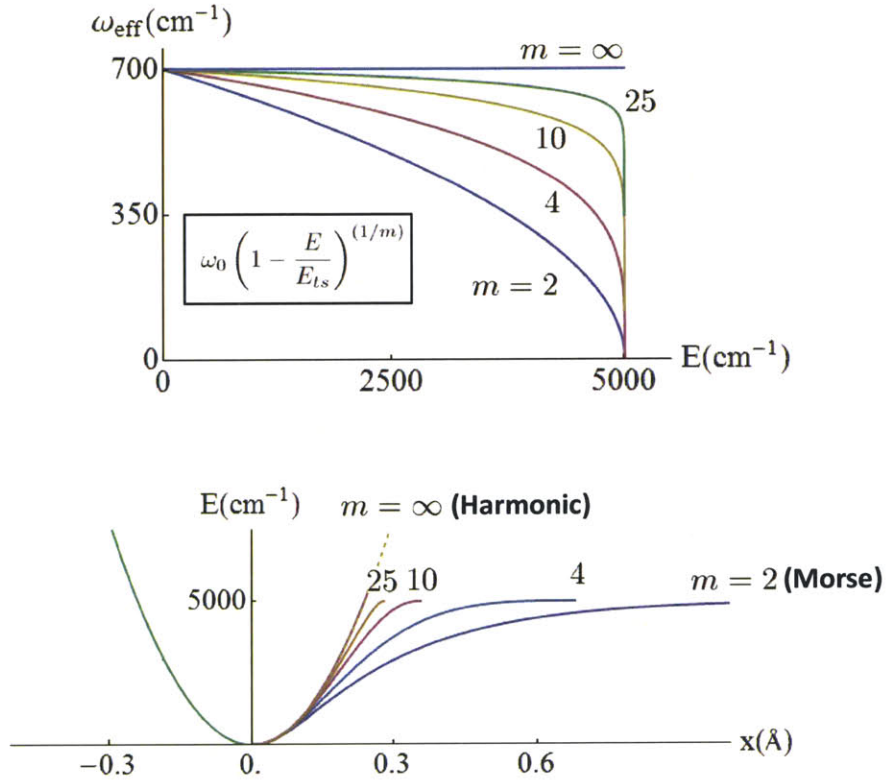

Figure 4-4: m dependence of the effective frequency dip. In (a) we give the model expression for the effective frequency dip with $m = 2, 4, 10, 25, \infty$. The values of ω_0 and E_{ts} are 700 and 5000 cm^{-1} respectively. The 1D potentials which would generate such effective frequency curves are given in (b). These effective 1D potentials are generated by RKR-type spectral inversion. We use an effective mass of 12 amu to generate potentials at a reasonable physical scale.

For each curve in Figure 4-4, the harmonic frequency and transition state energy are taken to be 700 cm^{-1} and 5000cm^{-1}, respectively. There are two interesting limiting cases for the dip expression and resulting 1D isomerization potentials. In the case $m \to \infty$, the effective frequency curve remains flat and constant at the

harmonic frequency. The potential for this curve is a harmonic parabola. In the other extreme, when $m = 2$, the effective frequency curve can be inverted analytically to the well known Morse potential with a dissociation energy equal to the value of E_{ts}. Intermediate values of m produce effective frequency curves and potentials that occur between these two extremes. Larger values of m produce a sharper decrease in the effective frequency. In the corresponding potential, this results in a steeper slope as the potential energy surface rises from the equilibrium well to the transition state barrier. By determining the value of m, experimental effective frequency fits of vibrational progressions along an isomerizing coordinate (or combination thereof) can provide direct qualitative information about the topography of the potential surface along the isomerization path. Comparing the fitted values of m from the 3^n6^2 data in Figure 4-3 (11.5 ± 3.5 and 6.3 ± 0.2 for the ν_3 and ν_6 effective frequency curves, respectively) to the inverted 1D potentials shows that the fits are at least physically reasonable, and probably indicates that the effective isomerization path is of an intermediate steepness with a moderately wide barrier. More refined treatments will require estimations of the effective mass of motion along the isomerization path.

As the existence of an effective frequency dip is intrinsically associated with approaching a transition state/stationary point on a PES, its observation (or lack thereof) is evidence for or against a possible isomerization pathway. In Figure 4-5, we compare the effective frequency curves for three progressions: 3^n, 3^n4^2, and 3^n6^2. The dip in the 3^n6^2 levels contrasts greatly with the curves for 3^n and 3^n4^2, which show no dip whatsoever. This indicates that these levels do not approach a stationary point on the potential surface. The lack of a dip for the progression involving quanta of ν_4, in particular, is further evidence that a torsional pathway does not contribute to *cis-trans* isomerization at these energies in S_1 acetylene. This is consistent with the other pieces of experimental and *ab initio* evidence presented in the two previous chapters, which also indicate that there is no active torsional isomerization mechanism at the energies so far sampled experimentally.

An effective frequency analysis also enables characterization of transition state vibrations. In Figure 4-6, we show an example that considers two vibrational pro-

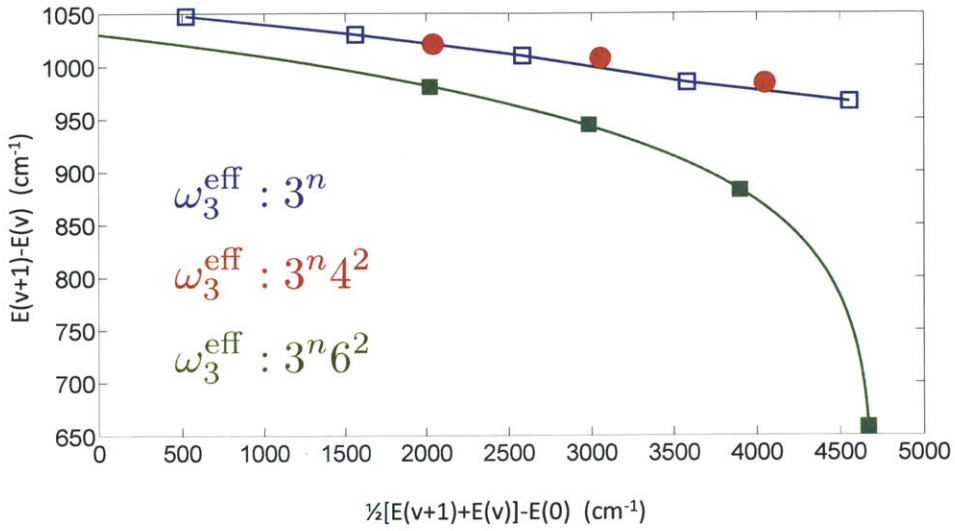

Figure 4-5: Spectator modes of *cis-trans* isomerization in S_1 acetylene. The effective ν_3 frequencies for the 3^n, 3^n4^2, and 3^n6^2 progressions are shown. As seen above, 3^n6^2 levels display a strong dip as they approach the isomerization transition state. The 3^n and 3^n4^2 progressions exhibit no dip. In particular, this suggests that there is not an accessible torsional transition state and that *cis-trans* isomerization occurs (at these energies) exclusively through an in-plane path.

gressions on a general potential surface with a well and transition state atop a barrier. The first progression consists of excited levels involving only the isomerizing mode, and the second contains the same levels including one additional quantum of a mode orthogonal to the isomerization path. The effective frequency dips for these two progressions are plotted on the right of the figure. The additional energy of the orthogonal mode shifts its effective frequency curve to the right. The magnitude of this shift, however, is not uniform. At low energy, the curve is shifted by the harmonic frequency of the orthogonal mode ω_0. The location of the dip is shifted by the frequency of the orthogonal mode at the isomerization transition state ω_{ts} which may differ from the low energy value. The change in orthogonal mode frequencies provides information on the relative curvature of the PES at the vicinity of the transition state. "Narrow" and "wide" isomerization channels correspond to increased and decreased orthogonal curvature, respectively. The current data set for S_1 acetylene is not quite complete enough to perform such an analysis. Vibrational levels up to and above the

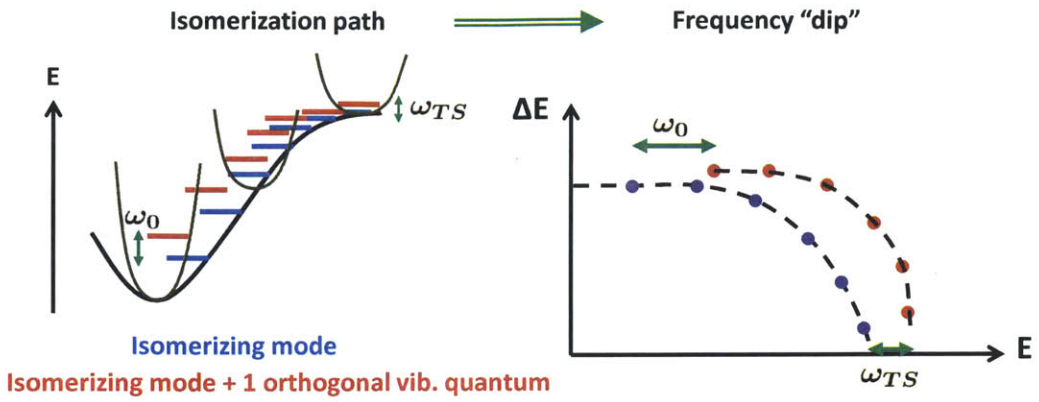

Figure 4-6: Characterization of transition state vibrations. On the left is a partial potential surface showing the approach to a transition state at the PES's stationary point. Vibrational levels with pure excitations in the isomerizing mode are given in blue. Their effective frequency dip is shown in the plot on the right. We compare this progression to one that has one additional quantum of excitation in a mode orthogonal to isomerization path (red). The horizontal displacement of the effective frequency curves for the two progressions gives information about the orthogonal mode's frequency at the equilibrium geometry (ω_0) and at the transition state (ω_{ts}). In this example, the curvature of the PES decreases in the orthogonal direction at the transition state, so that $\omega_{ts} < \omega_0$ for the orthogonal mode.

barrier will need to be measured and assigned. We discuss on-going experiments regarding these energy regions in the next chapter. In addition, we continue to consider what additional effects a mixed-mode isomerization coordinate (for example, in-plane *cis-trans* isomerization in S_1 acetylene requires combinations of both ν_3 and ν_6) has on the frequency dip patterns.

4.3 Discussion

We have proposed an empirical model to analyze the effective frequency patterns of isomerization active modes. This model provides information on the most relevant characteristics of an isomerizaton process: the heights of transition states and energy barriers, the qualitative shape and steepness of the isomerization path, and the relative curvature in orthogonal directions along the isomerization path. The preliminary analysis performed thus far on acetylene yields an observed transition state energy

of approximately 4500-5000 cm^{-1}, consistent with *ab initio* calculations [16, 22]. We anticipate being able to make more refined estimates when more complete vibrational data sets for the S_1 state are measured.

The frequency dip phenomenon is expected to be quite general. The models developed in this chapter are applicable not only to conformational changes, like *cis-trans* isomerization, but also to studies of reaction dynamics or *any* system which contains stationary points on its potential surface. Frequency domain spectroscopic characterization of the potential surface entails vastly more accurate experimental measurements than achievable by studies of kinetic rates, and the quantities extracted from an effective frequency model can be used directly as input to transition state theory calculations. Open questions remain, however. What is the expected structure of above-barrier vibrational levels? This will certainly be complicated and qualitatively different from the level structure that evolves up to the transition state energy. What does the above-barrier structure tell us about the barrier itself? Additionally, how can such empirical models, which require identification and measurement of vibrational states along an isomerization path, be applied to larger molecular systems where complete vibrational analyses are intractable? Spectroscopic techniques that are sensitive to large amplitude motions may be the answer (see for example recent work on HCN $\leftrightarrow$ HNC isomerization [48]). Lastly, how do we account for the higher dimensionality of multi-mode problems where more than one vibrational mode contributes to the isomerization path (as in S_1 acetylene)? Resolving these questions provides many interesting challenges and opportunities for further *ab initio* and experimental study.

Chapter 5

On-going and Future Work

5.1 IR-UV Double Resonance Spectra via Hot-Band Pumping

The spectroscopic double resonance schemes used in Chapter 2 are designed to access S_1 vibrational states with $K = 0, 1, 2$ (see Figure 2-1). It would be desirable, however, to access states with $K > 2$ in order to make more complete measurements of K-staggerings in tunneling vibrational states. In-plane bending isomerization causes a simple even/odd K-staggering pattern, but torsional tunneling would lead to a further staggering between $K = 4n$ and $K = 4n + 2$, levels. Though all current spectroscopic and *ab initio* evidence indicates that torsional tunneling does not occur, a measurement of the associated K-staggering would be the most direct and concrete experimental proof. As explained previously, K-staggerings are simplest to observe in *cis* vibrational states because their rotational structure is unperturbed by Coriolis coupling. Unfortunately, the experimental K coverage of observed *cis* states is scarce. Only for one level, *cis* $3^1 6^1$, have all three $K = 0 - 2$ states been observed. The only other level where at least both one even K and one odd K state have been observed is *cis* 6^2, for which the positions of the $K = 0$ and $K = 1$ state have provided an approximate measurement of the K-staggering (see Table 3.6). One experimental goal is to augment the $K = 0 - 2$ coverage of already identified *cis* levels, so as to learn

more about the vibrational character dependence of the K-staggerings. However, measurements of only $K = 0 - 2$ states are insufficient to characterize torsional staggerings, which require measurements of at least $K = 0 - 4$. The c-type $\tilde{A} - \tilde{X}$ transition carries a rotational selection rule of $K' - \ell'' = \pm 1$ (which is slightly broken by axis switching, but these effects are small). Therefore, access to $K = 3$ and 4 states requires UV excitation from initial levels in the $\tilde{X}$ state that have $\ell'' = 2$ and 3. One quantum of vibrational angular momentum can be prepared with an IR photon via a perpendicular transition, which leaves at least one or two units of vibrational angular momentum required in the IR transition's initial state. Current IR pumping schemes for double resonance spectroscopy of acetylene have used IR transitions beginning from the vibrationless ground state, which has $\ell'' = 0$. One of the strongest perpendicular bands is $\nu_3'' + \nu_4''$. The same transition occuring from vibrationally excited initial states can generate higher values of ℓ''. We propose to use IR hotbands such as $\nu_3''+2\nu_4''(\ell'' = 2) \leftarrow \nu_4''(\ell'' = 1)$, $\nu_3''+\nu_4''+\nu_5''(\ell'' = 2) \leftarrow \nu_5''(\ell'' = 1)$, and $\nu_3'' + 3\nu_4''(\ell'' = 3) \leftarrow 2\nu_4''(\ell'' = 2)$ to generate the required vibrational angular momentum to excite $K = 3$ and 4 states of S_1. The fact that there are both π_g and π_u degenerate bending modes in the ground state allows us to access all vibrational symmetries of the S_1 state via hot-band pumping.

The main experimental difficulty of performing hot-band pumped IR-UV double resonance is having sufficient population in vibrationally excited initial states that have one or two quanta of excitation in the low energy degenerate bending modes ν_4'' (*trans* bend, π_g) and ν_5'' (*cis* bend, π_u). Each quantum corresponds to approximately 1000 K of vibrational energy. In a supersonic molecular beam, where the vibrational temperature is mildly colder than room temperature, the population in the excited bending states is expected to be low. A heated supersonic molecular beam would provide simulataneous vibrational excitation, while maintaining a cold rotational temperature (which significantly decongests the excitation spectra). A crude harmonic oscillator vibrational partition function using the observed fundamental frequencies of the S_0 vibrational modes [49] can provide some reasonable expectations for the population enhancement from thermal excitation. Such a calculation

shows that one and two bending quanta levels achieve maximum population at 1100 K and 1600 K with population enhancement factors (compared to room temperature) of 2.5 and 5, respectively. These temperatures can be achieved by fitting a supersonic molecular beam valve with a SiC pyrolysis tube, which enables vibrational heating without compromising the rotational cooling in the molecular beam. Preliminary proof of principle experiments with such an apparatus confirm the predicted vibrational population enhancement factors and optimal heating temperatures. Early planned experiments include using these hot-band pumping schemes to measure additional K states of already identified *cis* levels, in particular *cis* $3^1 6^1$ and *cis* 6^2, for which the approximate positions of the higher-K states can be predicted from the known data. These spectra will provide the most direct experimental data yet acquired characterizing the extent of torsional tunneling in S_1 acetylene.

5.2 H-Atom Action Spectroscopy to Detect Predissociated States of S_1

Over the last several decades, acetylene has also been the subject of a number of photolysis studies investigating predissocation of the S_1 state to H+CCH fragments (see for example, Refs. [50–52] and references therein). A precise experimental measurement of the C−H bond dissociation energy places the threshold for photodissociation at 46074 ± 8 cm^{-1} [50]. As the transition state to *cis-trans* isomerization lies at approximately 47200 cm^{-1}, many states of interest to future studies of the near and above-barrier isomerization dynamics will be affected by predissociation. For such studies this poses a major spectroscopic detection problem. Fast photofragmentation results in excited state fluorescence lifetimes of at most only a few nanoseconds. As a result, fluoresence quantum efficiency is drastically reduced, making it increasingly difficult to observe LIF detected excitation spectra above 46000 cm^{-1}. To circumvent this problem, we have constructed an H-atom action spectroscopy apparatus which replaces LIF detection with H-atom detection. The H-atoms are first generated via

photodissociation by the scanned UV excitation pulse. They are subsequently ionized via 2+1 REMPI at 243 nm. The resulting protons are accelerated and focused by ion optics [53] onto a multi-channel array which records a TOF ion signal. The integrated TOF signal generates the UV excitation spectrum.

The construction and testing of this apparatus has recently been completed and is beginning to provide wide-range excitation spectra at significantly higher resolution (approximately $5-10$ times higher) than similar previous studies [52, 54]. In addition to extending our coverage of the S_1 vibrational manifold, these high resolution studies are expected to provide new insights into the predissociation mechanism and the nonadiabatic triplet interactions associated with it [51, 55].

Appendix A

Internal Coordinate Kinetic Energy Operator

This appendix contains the KEO coupling matrices Σ (Table A.1), Γ (Table A.2), and μ (Table A.3) as defined in Ref. [38]. They are appropriate for the internal coordinate system and body-fixed frame embedding convention defined in Figure 3-1. These matrices can be used directly to form a full dimensional non-constrained internal coordinate KEO from the following expression [38]:

$$\begin{aligned}\hat{T} = -\frac{\hbar^2}{2}\Bigg[&\Sigma^{ij}\partial_i\partial_j + \left\{\left(\partial_i\Sigma^{ij}\right) + \Sigma^{ij}f_i\right\}\partial_j + \\ &2\Gamma^{\alpha i}\partial_i\left(\frac{iJ_\alpha}{\hbar}\right) + \left\{\left(\partial_i\Gamma^{\alpha i}\right) + \Gamma^{\alpha i}f_i\right\}\left(\frac{iJ_\alpha}{\hbar}\right) + \\ &\mu^{\alpha\beta}\left(\frac{iJ_\alpha}{\hbar}\right)\left(\frac{iJ_\beta}{\hbar}\right) - \frac{1}{2}\left\{\frac{5}{8}\Sigma^{ij}\tilde{g}_i\tilde{g}_j + \frac{1}{2}\Sigma^{ij}f_if_j \right. \\ &\left. - \frac{1}{2}(\partial_i\Sigma^{ij})\tilde{g}_j - (\partial_i\Sigma^{ij})f_j - \frac{1}{2}\Sigma^{ij}G_{ij} - \Sigma^{ij}F_{ij}\right\}\Bigg] \end{aligned} \tag{A.1}$$

where i and j sum over the vibrational internal coordinates and α and β (not to be confused with the angles α and $\beta_{1,2}$) sum over the body-fixed axes x, y, and z. A few

definitions are required to use this expression. First, $\tilde{g}$ is the matrix determinant

$$\tilde{g} = \begin{vmatrix} \Sigma & \Gamma^T \\ \Gamma & \mu \end{vmatrix} \tag{A.2}$$

For our coordinate system and body-fixed frame, $\tilde{g} = (r_1^2 r_2^2 r_3^2 \sin\beta_1 \sin\beta_2)^{-2}$. f is the arbitrary internal coordinate normalization volume element. This can be any convenient expression. For this KEO, we choose $f = \sin\beta_1 \sin\beta_2$ (so that integrals are taken as $\int |f| dq$). $\tilde{g}_i$ and f_i are the logarithmic derivatives of $\tilde{g}$ and f with respect to internal coordinate i. G_{ij} and F_{ij} are the logarithmic second derivatives of $\tilde{g}$ and f.

Following the methods of Ref. [40], these matrices may be used to calculate the effective coupling matrices for reduced dimension constrained KEOs. The complete rovibrational KEO of such a reduction for acetylene with two frozen CH bonds is included in Table A.4.

In the subsequent tables the following definitions are also assumed:

$$\frac{1}{\mu_{CC}} = \frac{2}{m_C}$$
$$\frac{1}{\mu_{CH}} = \frac{1}{m_C} + \frac{1}{m_H}$$

Table A.1: Σ matrix for C_2H_2 internal coordinate KEO. As the matrix is symmetric, only the diagonal and upper triangle are given.

	r_3	r_1	r_2	β_1	β_2	α
r_3	$\frac{1}{\mu_{CC}}$	$-\frac{\cos\beta_1}{m_C}$	$-\frac{\cos\beta_2}{m_C}$	$\frac{\sin\beta_1}{m_C r_1}$	$\frac{\sin\beta_2}{m_C r_2}$	0
r_1		$\frac{1}{\mu_{CH}}$	0	$\frac{\sin\beta_1}{m_C r_3}$	$\frac{\cos 2\alpha \sin\beta_1}{m_C r_3}$	$-\frac{\sin 2\alpha \sin\beta_1 \cot\beta_2}{2m_C r_3}$
r_2			$\frac{1}{\mu_{CH}}$	$\frac{\cos 2\alpha \sin\beta_2}{m_C r_3}$	$\frac{\sin\beta_2}{m_C r_3}$	$-\frac{\sin 2\alpha \cot\beta_1 \sin\beta_2}{2m_C r_3}$
β_1				$\frac{1}{\mu_{CH} r_1^2} + \frac{1}{\mu_{CC} r_3^2} + \frac{2\cos\beta_1}{m_C r_1 r_3}$	$\cos 2\alpha \left(\frac{1}{\mu_{CC} r_3^2} + \frac{\cos\beta_1}{m_C r_1 r_3} + \frac{\cos\beta_2}{m_C r_2 r_3} \right)$	$-\frac{\sin 2\alpha}{2} \left(\frac{\csc\beta_2}{m_C r_2 r_3} + \frac{\cos\beta_1 \cot\beta_2}{m_C r_1 r_3} + \frac{\cot\beta_2}{\mu_{CC} r_3^2} \right)$
β_2					$\frac{1}{\mu_{CH} r_2^2} + \frac{1}{\mu_{CC} r_3^2} + \frac{2\cos\beta_2}{m_C r_2 r_3}$	$-\frac{\sin 2\alpha}{2} \left(\frac{\csc\beta_1}{m_C r_1 r_3} + \frac{\cos\beta_2 \cot\beta_1}{m_C r_2 r_3} + \frac{\cot\beta_1}{\mu_{CC} r_3^2} \right)$
α						$\Sigma^{\alpha\alpha}$

$$\Sigma^{\alpha\alpha} = -\frac{1}{2\mu_{CC} r_3^2} - \frac{\cos 2\alpha \cot\beta_1 \cot\beta_2}{2\mu_{CC} r_3^2} - \frac{\cos 2\alpha \csc\beta_1 \cot\beta_2}{2m_C r_1 r_3} - \frac{\cos 2\alpha \cot\beta_1 \csc\beta_2}{2m_C r_2 r_3} + \frac{\cot\beta_1 \csc\beta_1}{2m_C r_1 r_3} + \frac{\cot\beta_2 \csc\beta_2}{2m_C r_2 r_3}$$
$$+ \frac{\csc^2\beta_1}{4} \left(\frac{1}{\mu_{CC} r_3^2} + \frac{1}{\mu_{CH} r_1^2} \right) + \frac{\csc^2\beta_2}{4} \left(\frac{1}{\mu_{CC} r_3^2} + \frac{1}{\mu_{CH} r_2^2} \right)$$

Table A.2: Γ matrix for C_2H_2 internal coordinate KEO.

	r_3	r_1	r_2	β_1	β_2	α
x	0	$-\frac{\sin\alpha\sin\beta_1}{m_C r_3}$	$\frac{\sin\alpha\sin\beta_2}{m_C r_3}$	$-\frac{\sin\alpha}{\mu_{CC}r_3^2}-\frac{\sin\alpha\cos\beta_1}{m_C r_1 r_3}$	$\frac{\sin\alpha}{\mu_{CC}r_3^2}+\frac{\sin\alpha\cos\beta_2}{m_C r_2 r_3}$	$\Gamma^{x\alpha}$
y	0	$-\frac{\cos\alpha\sin\beta_1}{m_C r_3}$	$-\frac{\cos\alpha\sin\beta_2}{m_C r_3}$	$-\frac{\cos\alpha}{\mu_{CC}r_3^2}-\frac{\cos\alpha\cos\beta_1}{m_C r_1 r_3}$	$-\frac{\cos\alpha}{\mu_{CC}r_3^2}-\frac{\cos\alpha\cos\beta_2}{m_C r_2 r_3}$	$\Gamma^{y\alpha}$
z	0	$-\frac{\sin 2\alpha\sin\beta_1\cot\beta_2}{2m_C r_3}$	$\frac{\sin 2\alpha\cot\beta_1\sin\beta_2}{2m_C r_3}$	$-\frac{\sin 2\alpha}{2}\left(\frac{\cot\beta_2}{\mu_{CC}r_3^2}+\frac{\cos\beta_1\cot\beta_2}{m_C r_1 r_3}+\frac{\csc\beta_2}{m_C r_2 r_3}\right)$	$\frac{\sin 2\alpha}{2}\left(\frac{\cot\beta_1}{\mu_{CC}r_3^2}+\frac{\cos\beta_2\cot\beta_1}{m_C r_2 r_3}+\frac{\csc\beta_1}{m_C r_1 r_3}\right)$	$\Gamma^{z\alpha}$

$$\Gamma^{x\alpha}=\frac{\cos\alpha}{2}\left(-\frac{\cot\beta_1}{\mu_{CC}r_3^2}+\frac{\cot\beta_2}{\mu_{CC}r_3^2}-\frac{\csc\beta_1}{m_C r_1 r_3}+\frac{\csc\beta_2}{m_C r_2 r_3}\right)$$

$$\Gamma^{y\alpha}=\frac{\sin\alpha}{2}\left(+\frac{\cot\beta_1}{\mu_{CC}r_3^2}+\frac{\cot\beta_2}{\mu_{CC}r_3^2}+\frac{\csc\beta_1}{m_C r_1 r_3}+\frac{\csc\beta_2}{m_C r_2 r_3}\right)$$

$$\Gamma^{z\alpha}=-\frac{\cot\beta_1\csc\beta_1}{2m_C r_1 r_3}+\frac{\cot\beta_2\csc\beta_2}{2m_C r_2 r_3}-\frac{\csc^2\beta_1}{4}\left(\frac{1}{\mu_{CC}r_3^2}+\frac{1}{\mu_{CH}r_1^2}\right)+\frac{\csc^2\beta_2}{4}\left(\frac{1}{\mu_{CC}r_3^2}+\frac{1}{\mu_{CH}r_2^2}\right)$$

Table A.3: μ matrix for C_2H_2 internal coordinate KEO. As with Σ, this matrix is symmetric and only the diagonal and upper triangle are given.

	x	y	z
x	$\frac{1}{\mu_{CC}r_3^2}$	0	$\frac{\cos\alpha}{2}\left(+\frac{\cot\beta_1}{\mu_{CC}r_3^2}+\frac{\cot\beta_2}{\mu_{CC}r_3^2}+\frac{\csc\beta_1}{m_Cr_1r_3}+\frac{\csc\beta_2}{m_Cr_2r_3}\right)$
y		$\frac{1}{\mu_{CC}r_3^2}$	$\frac{\sin\alpha}{2}\left(-\frac{\cot\beta_1}{\mu_{CC}r_3^2}+\frac{\cot\beta_2}{\mu_{CC}r_3^2}-\frac{\csc\beta_1}{m_Cr_1r_3}+\frac{\csc\beta_2}{m_Cr_2r_3}\right)$
z			$-\frac{1}{2\mu_{CC}r_3^2}+\frac{\cos2\alpha\cot\beta_1\cot\beta_2}{2\mu_{CC}r_3^2}+\frac{\cos2\alpha\csc\beta_1\cot\beta_2}{2m_Cr_1r_3}$ $+\frac{\cos2\alpha\cot\beta_1\csc\beta_2}{2m_Cr_2r_3}+\frac{\cot\beta_1\csc\beta_1}{2m_Cr_1r_3}+\frac{\cot\beta_2\csc\beta_1}{2m_Cr_2r_3}$ $+\frac{\csc^2\beta_1}{4}\left(\frac{1}{\mu_{CC}r_3^2}+\frac{1}{\mu_{CH}r_1^2}\right)+\frac{\csc^2\beta_2}{4}\left(\frac{1}{\mu_{CC}r_3^2}+\frac{1}{\mu_{CH}r_2^2}\right)$

Table A.4: Constrained rovibrational KEO for frozen r_{CH} bonds. Multiply by $-\hbar^2/2$. The anti-Hermitian operator $\mathcal{D}_r$ is defined as $\mathcal{D}_r \equiv \frac{1}{r}\partial_r - \frac{1}{2r^2}$. Each row in the table is an individual separable term. The "Coeff." column gives the coefficient for each term, followed by the primitive operators for each internal coordinate or component of the body-fixed angular momentum. A blank entry indicates identity.

	Coeff.	r_3	β_1	β_2	α	$\vec{J}$
1	$-\frac{\mu_{CH}}{2m_C^2}$	$\frac{1}{r_3^2}$				
	$-\frac{2}{m_C r_1}$	$\frac{1}{r_3}$	$\cos\beta_1$			
	$-\frac{2}{m_C r_2}$	$\frac{1}{r_3}$		$\cos\beta_2$		
	$-\frac{3\mu_{CH}}{4m_C^2}$	$\frac{1}{r_3^2}$	$\cos 2\beta_1$			
	$-\frac{3\mu_{CH}}{4m_C^2}$	$\frac{1}{r_3^2}$		$\cos 2\beta_2$		
2	$\frac{\mu_{CH}}{m_C^2}$	$\mathcal{D}_{r_3}$				
	$\frac{2}{m_C r_1}$	∂_{r_3}	$\cos\beta_1$			
	$\frac{2}{m_C r_2}$	∂_{r_3}		$\cos\beta_2$		
	$\frac{3\mu_{CH}}{2m_C^2}$	$\mathcal{D}_{r_3}$	$\cos 2\beta_1$			
	$\frac{3\mu_{CH}}{2m_C^2}$	$\mathcal{D}_{r_3}$		$\cos 2\beta_2$		
3	$\frac{1}{\mu_{CC}}$	$\frac{1}{r_3^2}$	$\cot\beta_1\partial_{\beta_1}$			
	$\frac{1}{\mu_{CH}r_1^2}$		$\cot\beta_1\partial_{\beta_1}$			
	$\frac{2}{m_C r_1}$	$\frac{1}{r_3}$	$\cos\beta_1\cot\beta_1\partial_{\beta_1}$			
	$-\frac{2}{m_C r_1}$	$\frac{1}{r_3}$	$\sin\beta_1\partial_{\beta_1}$			
	$-\frac{3\mu_{CH}}{2m_C^2}$	$\frac{1}{r_3^2}$	$\sin 2\beta_1\partial_{\beta_1}$			
	$-\frac{2}{m_C r_2}$	$\frac{1}{r_3}$	∂_{β_1}	$\sin\beta_2$	$\cos 2\alpha$	
	$-\frac{3\mu_{CH}}{2m_C^2}$	$\frac{1}{r_3^2}$	∂_{β_1}	$\sin 2\beta_2$	$\cos 2\alpha$	
	$-\frac{\mu_{CH}}{m_C^2}$	$\frac{1}{r_3^2}$	$\cot\beta_1\partial_{\beta_1}$	$\sin^2\beta_2$	$\sin^2 2\alpha$	
4	$\frac{1}{\mu_{CC}}$	$\frac{1}{r_3^2}$		$\cot\beta_2\partial_{\beta_2}$		
	$\frac{1}{\mu_{CH}r_2^2}$			$\cot\beta_2\partial_{\beta_2}$		
	$\frac{2}{m_C r_2}$	$\frac{1}{r_3}$		$\cos\beta_2\cot\beta_2\partial_{\beta_2}$		
	$-\frac{2}{m_C r_2}$	$\frac{1}{r_3}$		$\sin\beta_2\partial_{\beta_2}$		
	$-\frac{3\mu_{CH}}{2m_C^2}$	$\frac{1}{r_3^2}$		$\sin 2\beta_2\partial_{\beta_2}$		

	$-\frac{2}{m_C r_1}$	$\frac{1}{r_3}$	$\sin\beta_1$	∂_{β_2}	$\cos 2\alpha$
	$-\frac{3\mu_{CH}}{2m_C^2}$	$\frac{1}{r_3^2}$	$\sin 2\beta_1$	∂_{β_2}	$\cos 2\alpha$
	$-\frac{\mu_{CH}}{m_C^2}$	$\frac{1}{r_3^2}$	$\sin^2\beta_1$	$\cot\beta_2\partial_{\beta_2}$	$\sin^2 2\alpha$
5	$-\frac{1}{2m_C r_1}$	$\frac{1}{r_3}$	$\cos\beta_1\cot\beta_1$	$\cot\beta_2$	$\sin 2\alpha\partial_\alpha$
	$-\frac{1}{2m_C r_2}$	$\frac{1}{r_3}$	$\cot\beta_1$	$\cos\beta_2\cot\beta_2$	$\sin 2\alpha\partial_\alpha$
	$\frac{1}{2m_C r_1}$	$\frac{1}{r_3}$	$\csc\beta_1$	$\cot\beta_2$	$\sin 2\alpha\partial_\alpha$
	$\frac{1}{2m_C r_2}$	$\frac{1}{r_3}$	$\cot\beta_1$	$\csc\beta_2$	$\sin 2\alpha\partial_\alpha$
	$\frac{1}{2m_C r_1}$	$\frac{1}{r_3}$	$\sin\beta_1$	$\cot\beta_2$	$\sin 2\alpha\partial_\alpha$
	$\frac{1}{2m_C r_2}$	$\frac{1}{r_3}$	$\cot\beta_1$	$\sin\beta_2$	$\sin 2\alpha\partial_\alpha$
	$\frac{3\mu_{CH}}{4m_C^2}$	$\frac{1}{r_3^2}$	$\sin 2\beta_1$	$\cot\beta_2$	$\sin 2\alpha\partial_\alpha$
	$\frac{3\mu_{CH}}{4m_C^2}$	$\frac{1}{r_3^2}$	$\cot\beta_1$	$\sin 2\beta_2$	$\sin 2\alpha\partial_\alpha$
6	$\frac{1}{\mu_{CC}}$	$\partial_{r_3}^2$			
	$-\frac{\mu_{CH}}{m_C^2}$	$\partial_{r_3}^2$	$\cos^2\beta_1$		
	$-\frac{\mu_{CH}}{m_C^2}$	$\partial_{r_3}^2$		$\cos^2\beta_2$	
7	$\frac{1}{\mu_{CH} r_1^2}$		$\partial_{\beta_1}^2$		
	$\frac{1}{\mu_{CC}}$	$\frac{1}{r_3^2}$	$\partial_{\beta_1}^2$		
	$\frac{2}{m_C r_1}$	$\frac{1}{r_3}$	$\cos\beta_1\partial_{\beta_1}^2$		
	$-\frac{\mu_{CH}}{m_C^2}$	$\frac{1}{r_3^2}$	$\sin^2\beta_1\partial_{\beta_1}^2$		
	$-\frac{\mu_{CH}}{m_C^2}$	$\frac{1}{r_3^2}$	$\partial_{\beta_1}^2$	$\sin^2\beta_2$	$\cos^2 2\alpha$
8	$\frac{1}{\mu_{CH} r_2^2}$			$\partial_{\beta_2}^2$	
	$\frac{1}{\mu_{CC}}$	$\frac{1}{r_3^2}$		$\partial_{\beta_2}^2$	
	$\frac{2}{m_C r_2}$	$\frac{1}{r_3}$		$\cos\beta_2\partial_{\beta_2}^2$	
	$-\frac{\mu_{CH}}{m_C^2}$	$\frac{1}{r_3^2}$		$\sin^2\beta_2\partial_{\beta_2}^2$	
	$-\frac{\mu_{CH}}{m_C^2}$	$\frac{1}{r_3^2}$	$\sin^2\beta_1$	$\partial_{\beta_2}^2$	$\cos^2 2\alpha$
9	$-\frac{1}{2\mu_{CC}}$	$\frac{1}{r_3^2}$			∂_α^2
	$-\frac{1}{2\mu_{CC}}$	$\frac{1}{r_3^2}$	$\cot\beta_1$	$\cot\beta_2$	$\cos 2\alpha\partial_\alpha^2$
	$-\frac{1}{2m_C r_1}$	$\frac{1}{r_3}$	$\csc\beta_1$	$\cot\beta_2$	$\cos 2\alpha\partial_\alpha^2$
	$-\frac{1}{2m_C r_2}$	$\frac{1}{r_3}$	$\cot\beta_1$	$\csc\beta_2$	$\cos 2\alpha\partial_\alpha^2$
10	$\frac{2}{m_C r_1}$	∂_{r_3}	$\sin\beta_1\partial_{\beta_1}$		

	$\frac{\mu_{CH}}{m_C^2}$	$\mathcal{D}_{r_3}$	$\sin 2\beta_1 \partial_{\beta_1}$			
	$\frac{\mu_{CH}}{m_C^2}$	$\mathcal{D}_{r_3}$	∂_{β_1}	$\sin 2\beta_2$	$\cos 2\alpha$	
11	$\frac{2}{m_C r_2}$	∂_{r_3}		$\sin \beta_2 \partial_{\beta_2}$		
	$\frac{\mu_{CH}}{m_C^2}$	$\mathcal{D}_{r_3}$		$\sin 2\beta_2 \partial_{\beta_2}$		
	$\frac{\mu_{CH}}{m_C^2}$	$\mathcal{D}_{r_3}$	$\sin 2\beta_1$	∂_{β_2}	$\cos 2\alpha$	
12	$-\frac{\mu_{CH}}{2m_C^2}$	$\mathcal{D}_{r_3}$	$\sin 2\beta_1$	$\cot \beta_2$	$\sin 2\alpha \partial_\alpha$	
	$-\frac{\mu_{CH}}{2m_C^2}$	$\mathcal{D}_{r_3}$	$\cot \beta_1$	$\sin 2\beta_2$	$\sin 2\alpha \partial_\alpha$	
13	$\frac{2}{\mu_{CC}}$	$\frac{1}{r_3^2}$	∂_{β_1}	∂_{β_2}	$\cos 2\alpha$	
	$\frac{2}{m_C r_1}$	$\frac{1}{r_3}$	$\cos \beta_1 \partial_{\beta_1}$	∂_{β_2}	$\cos 2\alpha$	
	$\frac{2}{m_C r_2}$	$\frac{1}{r_3}$	∂_{β_1}	$\cos \beta_2 \partial_{\beta_2}$	$\cos 2\alpha$	
	$-\frac{2\mu_{CH}}{m_C^2}$	$\frac{1}{r_3^2}$	$\sin^2 \beta_1 \partial_{\beta_1}$	∂_{β_2}	$\cos 2\alpha$	
	$-\frac{2\mu_{CH}}{m_C^2}$	$\frac{1}{r_3^2}$	∂_{β_1}	$\sin^2 \beta_2 \partial_{\beta_2}$	$\cos 2\alpha$	
14	$-\frac{1}{\mu_{CC}}$	$\frac{1}{r_3^2}$	∂_{β_1}	$\cot \beta_2$	$\sin 2\alpha \partial_\alpha$	
	$-\frac{1}{m_C r_1}$	$\frac{1}{r_3}$	$\cos \beta_1 \partial_{\beta_1}$	$\cot \beta_2$	$\sin 2\alpha \partial_\alpha$	
	$-\frac{1}{m_C r_2}$	$\frac{1}{r_3}$	∂_{β_1}	$\csc \beta_2$	$\sin 2\alpha \partial_\alpha$	
	$\frac{\mu_{CH}}{m_C^2}$	$\frac{1}{r_3^2}$	$\sin^2 \beta_1 \partial_{\beta_1}$	$\cot \beta_2$	$\sin 2\alpha \partial_\alpha$	
	$\frac{\mu_{CH}}{2m_C^2}$	$\frac{1}{r_3^2}$	$\cot \beta_1 \partial_{\beta_1}$	$\sin^2 \beta_2$	$\sin 4\alpha \partial_\alpha$	
15	$-\frac{1}{\mu_{CC}}$	$\frac{1}{r_3^2}$	$\cot \beta_1$	∂_{β_2}	$\sin 2\alpha \partial_\alpha$	
	$-\frac{1}{m_C r_2}$	$\frac{1}{r_3}$	$\cot \beta_1$	$\cos \beta_2 \partial_{\beta_2}$	$\sin 2\alpha \partial_\alpha$	
	$-\frac{1}{m_C r_1}$	$\frac{1}{r_3}$	$\csc \beta_1$	∂_{β_2}	$\sin 2\alpha \partial_\alpha$	
	$\frac{\mu_{CH}}{m_C^2}$	$\frac{1}{r_3^2}$	$\cot \beta_1$	$\sin^2 \beta_2 \partial_{\beta_2}$	$\sin 2\alpha \partial_\alpha$	
	$\frac{\mu_{CH}}{2m_C^2}$	$\frac{1}{r_3^2}$	$\sin^2 \beta_1$	$\cot \beta_2 \partial_{\beta_2}$	$\sin 4\alpha \partial_\alpha$	
16	$-\frac{\mu_{CH}}{m_C^2}$	$\mathcal{D}_{r_3}$	$\sin 2\beta_1$		$\sin \alpha$	$iJ_x/\hbar$
	$\frac{\mu_{CH}}{m_C^2}$	$\mathcal{D}_{r_3}$		$\sin 2\beta_2$	$\sin \alpha$	$iJ_x/\hbar$
17	$-\frac{\mu_{CH}}{m_C^2}$	$\mathcal{D}_{r_3}$	$\sin 2\beta_1$		$\cos \alpha$	$iJ_y/\hbar$
	$-\frac{\mu_{CH}}{m_C^2}$	$\mathcal{D}_{r_3}$		$\sin 2\beta_2$	$\cos \alpha$	$iJ_y/\hbar$
18	$-\frac{\mu_{CH}}{2m_C^2}$	$\mathcal{D}_{r_3}$	$\sin 2\beta_1$	$\cot \beta_2$	$\sin 2\alpha$	$iJ_z/\hbar$
	$\frac{\mu_{CH}}{2m_C^2}$	$\mathcal{D}_{r_3}$	$\cot \beta_1$	$\sin 2\beta_2$	$\sin 2\alpha$	$iJ_z/\hbar$
19	$-\frac{2}{\mu_{CC}}$	$\frac{1}{r_3^2}$	∂_{β_1}		$\sin \alpha$	$iJ_x/\hbar$

	$-\frac{2}{m_C r_1}$	$\frac{1}{r_3}$	$\cos\beta_1\partial_{\beta_1}$		$\sin\alpha$	$iJ_x/\hbar$
	$\frac{2\mu_{CH}}{m_C^2}$	$\frac{1}{r_3^2}$	$\sin^2\beta_1\partial_{\beta_1}$		$\sin\alpha$	$iJ_x/\hbar$
	$-\frac{2\mu_{CH}}{m_C^2}$	$\frac{1}{r_3^2}$	∂_{β_1}	$\sin^2\beta_2$	$\cos 2\alpha\sin\alpha$	$iJ_x/\hbar$
20	$-\frac{2}{\mu_{CC}}$	$\frac{1}{r_3^2}$	∂_{β_1}		$\cos\alpha$	$iJ_y/\hbar$
	$-\frac{2}{m_C r_1}$	$\frac{1}{r_3}$	$\cos\beta_1\partial_{\beta_1}$		$\cos\alpha$	$iJ_y/\hbar$
	$\frac{2\mu_{CH}}{m_C^2}$	$\frac{1}{r_3^2}$	$\sin^2\beta_1\partial_{\beta_1}$		$\cos\alpha$	$iJ_y/\hbar$
	$+\frac{2\mu_{CH}}{m_C^2}$	$\frac{1}{r_3^2}$	∂_{β_1}	$\sin^2\beta_2$	$\cos 2\alpha\cos\alpha$	$iJ_y/\hbar$
21	$\frac{\mu_{CH}}{m_C^2}$	$\frac{1}{r_3^2}$	$\sin^2\beta_1\partial_{\beta_1}$	$\cot\beta_2$	$\sin 2\alpha$	$iJ_z/\hbar$
	$-\frac{\mu_{CH}}{2m_C^2}$	$\frac{1}{r_3^2}$	$\cot\beta_1\partial_{\beta_1}$	$\sin^2\beta_2$	$\sin 4\alpha$	$iJ_z/\hbar$
	$-\frac{1}{\mu_{CC}}$	$\frac{1}{r_3^2}$	∂_{β_1}	$\cot\beta_2$	$\sin 2\alpha$	$iJ_z/\hbar$
	$-\frac{1}{m_C r_1}$	$\frac{1}{r_3}$	$\cos\beta_1\partial_{\beta_1}$	$\cot\beta_2$	$\sin 2\alpha$	$iJ_z/\hbar$
	$-\frac{1}{m_C r_2}$	$\frac{1}{r_3}$	∂_{β_1}	$\csc\beta_2$	$\sin 2\alpha$	$iJ_z/\hbar$
22	$\frac{2}{\mu_{CC}}$	$\frac{1}{r_3^2}$		∂_{β_2}	$\sin\alpha$	$iJ_x/\hbar$
	$\frac{2}{m_C r_2}$	$\frac{1}{r_3}$		$\cos\beta_2\partial_{\beta_2}$	$\sin\alpha$	$iJ_x/\hbar$
	$-\frac{2\mu_{CH}}{m_C^2}$	$\frac{1}{r_3^2}$		$\sin^2\beta_2\partial_{\beta_2}$	$\sin\alpha$	$iJ_x/\hbar$
	$\frac{2\mu_{CH}}{m_C^2}$	$\frac{1}{r_3^2}$	$\sin^2\beta_1$	∂_{β_2}	$\cos 2\alpha\sin\alpha$	$iJ_x/\hbar$
23	$-\frac{2}{\mu_{CC}}$	$\frac{1}{r_3^2}$		∂_{β_2}	$\cos\alpha$	$iJ_y/\hbar$
	$-\frac{2}{m_C r_2}$	$\frac{1}{r_3}$		$\cos\beta_2\partial_{\beta_2}$	$\cos\alpha$	$iJ_y/\hbar$
	$\frac{2\mu_{CH}}{m_C^2}$	$\frac{1}{r_3^2}$		$\sin^2\beta_2\partial_{\beta_2}$	$\cos\alpha$	$iJ_y/\hbar$
	$+\frac{2\mu_{CH}}{m_C^2}$	$\frac{1}{r_3^2}$	$\sin^2\beta_1$	∂_{β_2}	$\cos 2\alpha\cos\alpha$	$iJ_y/\hbar$
24	$-\frac{\mu_{CH}}{m_C^2}$	$\frac{1}{r_3^2}$	$\cot\beta_1$	$\sin^2\beta_2\partial_{\beta_2}$	$\sin 2\alpha$	$iJ_z/\hbar$
	$\frac{\mu_{CH}}{2m_C^2}$	$\frac{1}{r_3^2}$	$\sin^2\beta_1$	$\cot\beta_2\partial_{\beta_2}$	$\sin 4\alpha$	$iJ_z/\hbar$
	$\frac{1}{\mu_{CC}}$	$\frac{1}{r_3^2}$	$\cot\beta_1$	∂_{β_2}	$\sin 2\alpha$	$iJ_z/\hbar$
	$\frac{1}{m_C r_2}$	$\frac{1}{r_3}$	$\cot\beta_1$	$\cos\beta_2\partial_{\beta_2}$	$\sin 2\alpha$	$iJ_z/\hbar$
	$\frac{1}{m_C r_1}$	$\frac{1}{r_3}$	$\csc\beta_1$	∂_{β_2}	$\sin 2\alpha$	$iJ_z/\hbar$
25	$-\frac{1}{\mu_{CC}}$	$\frac{1}{r_3^2}$	$\cot\beta_1$		$\cos\alpha\partial_\alpha$	$iJ_x/\hbar$
	$\frac{1}{\mu_{CC}}$	$\frac{1}{r_3^2}$		$\cot\beta_2$	$\cos\alpha\partial_\alpha$	$iJ_x/\hbar$
	$-\frac{1}{m_C r_1}$	$\frac{1}{r_3}$	$\csc\beta_1$		$\cos\alpha\partial_\alpha$	$iJ_x/\hbar$
	$\frac{1}{m_C r_2}$	$\frac{1}{r_3}$		$\csc\beta_2$	$\cos\alpha\partial_\alpha$	$iJ_x/\hbar$

	$-\frac{\mu_{CH}}{m_C^2}$	$\frac{1}{r_3^2}$	$\sin^2\beta_1$	$\cot\beta_2$	$\sin\alpha\sin 2\alpha\partial_\alpha$	$iJ_x/\hbar$
	$\frac{\mu_{CH}}{m_C^2}$	$\frac{1}{r_3^2}$	$\cot\beta_1$	$\sin^2\beta_2$	$\sin\alpha\sin 2\alpha\partial_\alpha$	$iJ_x/\hbar$
26	$\frac{1}{\mu_{CC}}$	$\frac{1}{r_3^2}$	$\cot\beta_1$		$\sin\alpha\partial_\alpha$	$iJ_y/\hbar$
	$\frac{1}{\mu_{CC}}$	$\frac{1}{r_3^2}$		$\cot\beta_2$	$\sin\alpha\partial_\alpha$	$iJ_y/\hbar$
	$\frac{1}{m_C r_1}$	$\frac{1}{r_3}$	$\csc\beta_1$		$\sin\alpha\partial_\alpha$	$iJ_y/\hbar$
	$\frac{1}{m_C r_2}$	$\frac{1}{r_3}$		$\csc\beta_2$	$\sin\alpha\partial_\alpha$	$iJ_y/\hbar$
	$-\frac{\mu_{CH}}{m_C^2}$	$\frac{1}{r_3^2}$	$\sin^2\beta_1$	$\cot\beta_2$	$\cos\alpha\sin 2\alpha\partial_\alpha$	$iJ_y/\hbar$
	$-\frac{\mu_{CH}}{m_C^2}$	$\frac{1}{r_3^2}$	$\cot\beta_1$	$\sin^2\beta_2$	$\cos\alpha\sin 2\alpha\partial_\alpha$	$iJ_y/\hbar$
27	$-\frac{1}{2\mu_{CC}}$	$\frac{1}{r_3^2}$	$\cot\beta_1$		$\sin\alpha$	$iJ_x/\hbar$
	$-\frac{1}{m_C r_1}$	$\frac{1}{r_3}$	$\cos\beta_1\cot\beta_1$		$\sin\alpha$	$iJ_x/\hbar$
	$\frac{1}{2\mu_{CC}}$	$\frac{1}{r_3^2}$		$\cot\beta_2$	$\sin\alpha$	$iJ_x/\hbar$
	$\frac{1}{m_C r_2}$	$\frac{1}{r_3}$		$\cos\beta_2\cot\beta_2$	$\sin\alpha$	$iJ_x/\hbar$
	$\frac{1}{2m_C r_1}$	$\frac{1}{r_3}$	$\csc\beta_1$		$\sin\alpha$	$iJ_x/\hbar$
	$-\frac{1}{2m_C r_2}$	$\frac{1}{r_3}$		$\csc\beta_2$	$\sin\alpha$	$iJ_x/\hbar$
	$\frac{1}{m_C r_1}$	$\frac{1}{r_3}$	$\sin\beta_1$		$\sin\alpha$	$iJ_x/\hbar$
	$\frac{3\mu_{CH}}{2m_C^2}$	$\frac{1}{r_3^2}$	$\sin 2\beta_1$		$\sin\alpha$	$iJ_x/\hbar$
	$-\frac{\mu_{CH}}{m_C^2}$	$\frac{1}{r_3^2}$	$\sin^2\beta_1$	$\cot\beta_2$	$\sin\alpha\cos^2\alpha$	$iJ_x/\hbar$
	$-\frac{1}{m_C r_2}$	$\frac{1}{r_3}$		$\sin\beta_2$	$\sin\alpha$	$iJ_x/\hbar$
	$-\frac{3\mu_{CH}}{2m_C^2}$	$\frac{1}{r_3^2}$		$\sin 2\beta_2$	$\sin\alpha$	$iJ_x/\hbar$
	$\frac{\mu_{CH}}{m_C^2}$	$\frac{1}{r_3^2}$	$\cot\beta_1$	$\sin^2\beta_2$	$\sin\alpha\cos^2\alpha$	$iJ_x/\hbar$
28	$-\frac{1}{2\mu_{CC}}$	$\frac{1}{r_3^2}$	$\cot\beta_1$		$\cos\alpha$	$iJ_y/\hbar$
	$-\frac{1}{m_C r_1}$	$\frac{1}{r_3}$	$\cos\beta_1\cot\beta_1$		$\cos\alpha$	$iJ_y/\hbar$
	$-\frac{1}{2\mu_{CC}}$	$\frac{1}{r_3^2}$		$\cot\beta_2$	$\cos\alpha$	$iJ_y/\hbar$
	$-\frac{1}{m_C r_2}$	$\frac{1}{r_3}$		$\cos\beta_2\cot\beta_2$	$\cos\alpha$	$iJ_y/\hbar$
	$\frac{1}{2m_C r_1}$	$\frac{1}{r_3}$	$\csc\beta_1$		$\cos\alpha$	$iJ_y/\hbar$
	$\frac{1}{2m_C r_2}$	$\frac{1}{r_3}$		$\csc\beta_2$	$\cos\alpha$	$iJ_y/\hbar$
	$\frac{1}{m_C r_1}$	$\frac{1}{r_3}$	$\sin\beta_1$		$\cos\alpha$	$iJ_y/\hbar$
	$\frac{3\mu_{CH}}{2m_C^2}$	$\frac{1}{r_3^2}$	$\sin 2\beta_1$		$\cos\alpha$	$iJ_y/\hbar$
	$\frac{\mu_{CH}}{m_C^2}$	$\frac{1}{r_3^2}$	$\sin^2\beta_1$	$\cot\beta_2$	$\cos\alpha\sin^2\alpha$	$iJ_y/\hbar$

	$\frac{1}{m_C r_2}$	$\frac{1}{r_3}$		$\sin\beta_2$	$\cos\alpha$	$iJ_y/\hbar$
	$\frac{3\mu_{CH}}{2m_C^2}$	$\frac{1}{r_3^2}$		$\sin 2\beta_2$	$\cos\alpha$	$iJ_y/\hbar$
	$\frac{\mu_{CH}}{m_C^2}$	$\frac{1}{r_3^2}$	$\cot\beta_1$	$\sin^2\beta_2$	$\cos\alpha\sin^2\alpha$	$iJ_y/\hbar$
29	$-\frac{1}{2m_C r_1}$	$\frac{1}{r_3}$	$\cos\beta_1\cot\beta_1$	$\cot\beta_2$	$\sin 2\alpha$	$iJ_z/\hbar$
	$\frac{1}{2m_C r_2}$	$\frac{1}{r_3}$	$\cot\beta_1$	$\cos\beta_2\cot\beta_2$	$\sin 2\alpha$	$iJ_z/\hbar$
	$\frac{1}{2m_C r_1}$	$\frac{1}{r_3}$	$\csc\beta_1$	$\cot\beta_2$	$\sin 2\alpha$	$iJ_z/\hbar$
	$-\frac{1}{2m_C r_2}$	$\frac{1}{r_3}$	$\cot\beta_1$	$\csc\beta_2$	$\sin 2\alpha$	$iJ_z/\hbar$
	$\frac{1}{2m_C r_1}$	$\frac{1}{r_3}$	$\sin\beta_1$	$\cot\beta_2$	$\sin 2\alpha$	$iJ_z/\hbar$
	$-\frac{1}{2m_C r_2}$	$\frac{1}{r_3}$	$\cot\beta_1$	$\sin\beta_2$	$\sin 2\alpha$	$iJ_z/\hbar$
	$\frac{3\mu_{CH}}{4m_C^2}$	$\frac{1}{r_3^2}$	$\sin 2\beta_1$	$\cot\beta_2$	$\sin 2\alpha$	$iJ_z/\hbar$
	$-\frac{3\mu_{CH}}{4m_C^2}$	$\frac{1}{r_3^2}$	$\cot\beta_1$	$\sin 2\beta_2$	$\sin 2\alpha$	$iJ_z/\hbar$
30	$-\frac{1}{\mu_{CC}}$	$\frac{1}{r_3^2}$				$J_x^2/\hbar^2$
	$\frac{\mu_{CH}}{m_C^2}$	$\frac{1}{r_3^2}$	$\sin^2\beta_1$		$\sin^2\alpha$	$J_x^2/\hbar^2$
	$\frac{\mu_{CH}}{m_C^2}$	$\frac{1}{r_3^2}$		$\sin^2\beta_2$	$\sin^2\alpha$	$J_x^2/\hbar^2$
31	$-\frac{1}{\mu_{CC}}$	$\frac{1}{r_3^2}$				$J_x^2/\hbar^2$
	$\frac{\mu_{CH}}{m_C^2}$	$\frac{1}{r_3^2}$	$\sin^2\beta_1$		$\cos^2\alpha$	$J_y^2/\hbar^2$
	$\frac{\mu_{CH}}{m_C^2}$	$\frac{1}{r_3^2}$		$\sin^2\beta_2$	$\cos^2\alpha$	$J_y^2/\hbar^2$
32	$\frac{1}{2\mu_{CC}}$	$\frac{1}{r_3^2}$				$J_z^2/\hbar^2$
	$-\frac{1}{2\mu_{CC}}$	$\frac{1}{r_3^2}$	$\cot\beta_1$	$\cot\beta_2$	$\cos 2\alpha$	$J_z^2/\hbar^2$
	$-\frac{1}{2m_C r_1}$	$\frac{1}{r_3}$	$\csc\beta_1$	$\cot\beta_2$	$\cos 2\alpha$	$J_z^2/\hbar^2$
	$-\frac{1}{2m_C r_2}$	$\frac{1}{r_3}$	$\cot\beta_1$	$\csc\beta_2$	$\cos 2\alpha$	$J_z^2/\hbar^2$
33	$\frac{\mu_{CH}}{2m_C^2}$	$\frac{1}{r_3^2}$	$\sin^2\beta_1$		$\sin 2\alpha$	$[J_x, J_y]_+/\hbar^2$
	$-\frac{\mu_{CH}}{2m_C^2}$	$\frac{1}{r_3^2}$		$\sin^2\beta_2$	$\sin 2\alpha$	$[J_x, J_y]_+/\hbar^2$
34	$-\frac{1}{2m_C r_1}$	$\frac{1}{r_3}$	$\csc\beta_1$		$\cos\alpha$	$[J_x, J_z]_+/\hbar^2$
	$-\frac{1}{2m_C r_2}$	$\frac{1}{r_3}$		$\csc\beta_2$	$\cos\alpha$	$[J_x, J_z]_+/\hbar^2$
	$\frac{\mu_{CH}}{m_C^2}$	$\frac{1}{r_3^2}$	$\sin^2\beta_1$	$\cot\beta_2$	$\cos\alpha\sin^2\alpha$	$[J_x, J_z]_+/\hbar^2$
	$\frac{\mu_{CH}}{m_C^2}$	$\frac{1}{r_3^2}$	$\cot\beta_1$	$\sin^2\beta_2$	$\cos\alpha\sin^2\alpha$	$[J_x, J_z]_+/\hbar^2$
	$-\frac{1}{2\mu_{CC}}$	$\frac{1}{r_3^2}$	$\cot\beta_1$		$\cos\alpha$	$[J_x, J_z]_+/\hbar^2$
	$-\frac{1}{2\mu_{CC}}$	$\frac{1}{r_3^2}$		$\cot\beta_2$	$\cos\alpha$	$[J_x, J_z]_+/\hbar^2$

35	$\frac{1}{2m_C r_1}$	$\frac{1}{r_3}$	$\csc\beta_1$		$\sin\alpha$	$[J_y, J_z]_+/\hbar^2$
	$-\frac{1}{2m_C r_2}$	$\frac{1}{r_3}$		$\csc\beta_2$	$\sin\alpha$	$[J_y, J_z]_+/\hbar^2$
	$\frac{\mu_{CH}}{m_C^2}$	$\frac{1}{r_3^2}$	$\sin^2\beta_1$	$\cot\beta_2$	$\sin\alpha\cos^2\alpha$	$[J_y, J_z]_+/\hbar^2$
	$-\frac{\mu_{CH}}{m_C^2}$	$\frac{1}{r_3^2}$	$\cot\beta_1$	$\sin^2\beta_2$	$\sin\alpha\cos^2\alpha$	$[J_y, J_z]_+/\hbar^2$
	$\frac{1}{2\mu_{CC}}$	$\frac{1}{r_3^2}$	$\cot\beta_1$		$\sin\alpha$	$[J_y, J_z]_+/\hbar^2$
	$-\frac{1}{2\mu_{CC}}$	$\frac{1}{r_3^2}$		$\cot\beta_2$	$\sin\alpha$	$[J_y, J_z]_+/\hbar^2$
36	$-\frac{\mu_{CH}}{4m_C^2}$	$\frac{1}{r_3^2}$	$\cot^2\beta_1$	$\sin^2\beta_2$	$\sin 4\alpha$	$(\partial_\alpha - \frac{iJ_z}{\hbar})$
	$-\frac{\mu_{CH}}{4m_C^2}$	$\frac{1}{r_3^2}$	$\csc^2\beta_1$	$\sin^2\beta_2$	$\sin 4\alpha$	$(\partial_\alpha - \frac{iJ_z}{\hbar})$
	$-\frac{\mu_{CH}}{4m_C^2}$	$\frac{1}{r_3^2}$	$\sin^2\beta_1$	$\cot^2\beta_2$	$\sin 4\alpha$	$(\partial_\alpha + \frac{iJ_z}{\hbar})$
	$-\frac{\mu_{CH}}{4m_C^2}$	$\frac{1}{r_3^2}$	$\sin^2\beta_1$	$\csc^2\beta_2$	$\sin 4\alpha$	$(\partial_\alpha + \frac{iJ_z}{\hbar})$
	$\frac{1}{2m_C r_1}$	$\frac{1}{r_3}$	$\cot\beta_1\csc\beta_1$			$(\partial_\alpha - \frac{iJ_z}{\hbar})^2$
	$\frac{1}{4\mu_{CC}}$	$\frac{1}{r_3^2}$	$\csc^2\beta_1$			$(\partial_\alpha - \frac{iJ_z}{\hbar})^2$
	$\frac{1}{4\mu_{CH}r_1^2}$		$\csc^2\beta_1$			$(\partial_\alpha - \frac{iJ_z}{\hbar})^2$
	$-\frac{\mu_{CH}}{4m_C^2}$	$\frac{1}{r_3^2}$	$\cot^2\beta_1$	$\sin^2\beta_2$	$\sin^2 2\alpha$	$(\partial_\alpha - \frac{iJ_z}{\hbar})^2$
	$\frac{1}{2m_C r_2}$	$\frac{1}{r_3}$		$\cot\beta_2\csc\beta_2$		$(\partial_\alpha + \frac{iJ_z}{\hbar})^2$
	$\frac{1}{4\mu_{CC}}$	$\frac{1}{r_3^2}$		$\csc^2\beta_2$		$(\partial_\alpha + \frac{iJ_z}{\hbar})^2$
	$\frac{1}{4\mu_{CH}r_2^2}$			$\csc^2\beta_2$		$(\partial_\alpha + \frac{iJ_z}{\hbar})^2$
	$-\frac{\mu_{CH}}{4m_C^2}$	$\frac{1}{r_3^2}$	$\sin^2\beta_1$	$\cot^2\beta_2$	$\sin^2 2\alpha$	$(\partial_\alpha + \frac{iJ_z}{\hbar})^2$

Appendix B

Calculated J=0 Level List

Table B.1: Calculated $J = 0$ level list. Assignments for all vibrational states up to 5000 cm^{-1} above the *trans* zero point are included. States are organized by their $G_4^{(8)}$ symmetry. *trans* states are labeled by quantum numbers only. *cis* states are prefixed explicitly by "*cis*". Local interactions which mix zero-order states of the same symmetry are indicated by superscript letters prefixed to the vibrational assignment. For correlations of $G_4^{(8)}$ symmetry species to those of the C_{2v} and C_{2h} point groups, which describe the *cis* and *trans* equilibrium geometries, see Ref. [26].

	A_{1g}^+		A_{2g}^-		B_{2u}^+		B_{1u}^-	
0	0	0.000	$4^1 6^1$	1546.190	6^1	774.087	4^1	748.972
1	3^1	1070.776	$3^1 4^1 6^1$	2624.276	$3^1 6^1$	1871.176	$3^1 4^1$	1813.488
2	2^1	1386.935	$2^1 4^1 6^1$	2907.211	$2^1 6^1$	2155.751	$2^1 4^1$	2113.802
3	$B^2(4^2)$	1496.216	B^4	3046.354	B^3	2286.898	B^3	2253.305
4	$B^2(6^2)$	1573.437	B^4	3197.974	B^3	2373.155	B^3	2370.655
5	3^2	2150.114	$3^2 4^1 6^1$	3625.150	$3^2 6^1$	2880.419	$3^2 4^1$	2875.804
6	$2^1 3^1$	2459.348	$2^1 3^1 4^1 6^1$	3967.769	$2^1 3^1 6^1$	3233.536	$2^1 3^1 4^1$	3179.374
7	$3^1 B^2$	2545.400	$3^1 B^4$	4027.964	$3^1 6^3$	3283.891	$3^1 B^3$	3290.462
8	$3^1 B^2$	2600.272	$3^1 B^4$	4197.186	$3^1 B^3$	3397.171	$3^1 B^3$	3390.403
9	2^2	2749.267	$2^2 4^1 6^1$	4242.738	$cis 6^1$	3506.727	$2^2 4^1$	3453.282
10	$2^1 4^2$	2849.488	$^a cis\, 4^1 6^1$	4380.575	$2^2 6^1$	3512.657	$2^1 B^3$	3591.764
11	$cis\, 0$	2913.603	$^a 2^1 B^4$	4382.426	$2^1 B^3$	3638.571	$2^1 B^3$	3716.241
12	$2^1 6^2$	2942.205	B^6	4495.158	$2^1 B^3$	3721.625	$cis\, 4^1$	3747.777
13	B^4	3000.878	$2^1 B^4$	4535.566	B^5	3761.452	B^5	3752.188
14	B^4	3070.299	$3^3 4^1 6^1$	4605.019	$^a B^5$	3844.902	B^5	3849.977

15	B^4	3182.692	B^6	4679.541	$^a3^36^1$	3882.260	3^34^1	3914.903
16	3^3	3219.905	B^6	4888.737	B^5	4032.311	B^5	4041.770
17	$^a2^13^2$	3526.528	3^2B^4	4947.392	$^b cis\,3^16^1$	4186.718	$2^13^24^1$	4234.222
18	$^a3^26^2$	3557.865	$2^13^24^16^1$	4994.302	$^b3^26^3$	4223.249	3^2B^3	4289.494
19	3^24^2	3631.286	$cis\,3^14^16^1$	5078.797	$2^13^26^1$	4272.160	3^2B^3	4404.902
20	$cis\,3^1$	3677.482	3^2B^4	5188.374	3^2B^3	4395.006	$cis\,3^14^1$	4492.842
21	2^23^1	3822.057	$^b2^23^14^16^1$	5289.706	$2^23^16^1$	4576.649	$2^23^14^1$	4519.321
22	$2^13^14^2$	3903.132	$^b2^13^1B^4$	5361.199	$^c3^1B^5$	4615.540	$2^13^1B^3$	4632.681
23	$^b3^1B^4$	3949.312	$^b3^1B^6$	5403.682	$^c2^13^16^3$	4662.041	3^1B^5	4709.051
24	$^b2^13^16^2$	3986.884	$2^13^1B^4$	5524.929	$cis\,6^3$	4729.097	$2^13^1B^3$	4740.926
25	3^1B^4	4064.047	$2^34^16^1$	5555.472	$2^13^1B^3$	4736.278	2^34^1	4769.802
26	2^3	4087.331	$3^44^16^1$	5561.245	$^d3^46^1$	4806.953	3^1B^5	4851.845
27	$cis\,6^2$	4099.394	$^d3^1B^6$	5604.622	$^d3^1B^5$	4824.154	2^2B^3	4905.418
28	2^24^2	4178.966	$^d cis\,4^16^3$	5647.290	2^36^1	4845.775	3^44^1	4933.373
29	3^1B^4	4196.799	2^2B^4	5692.860	$cis\,3^26^1$	4914.631	$cis\,4^16^2$	5007.470
30	3^4	4238.469	$cis\,3^24^16^1$	5765.880	2^2B^3	4965.660	3^1B^5	5023.834
31	2^26^2	4286.130	2^1B^6	5812.286	$cis\,2^16^1$	5001.845		5038.916
32	2^1B^4	4330.680	2^2B^4	5848.320	3^1B^5	5019.101		5070.587
33	2^1B^4	4405.469	$cis\,2^14^16^1$	5849.811	2^2B^3	5049.488		5161.822
34	$cis\,3^2$	4422.134	3^1B^6	5870.068		5079.659		5195.072
35	$cis\,2^1$	4427.577		5900.103		5103.546		5222.683
36	B^6	4460.850		5943.805		5190.127		5234.761
37	$^c3^36^2$	4500.656		5967.844		5207.753		5253.869
38	$^c2^1B^4$	4523.688		6008.429		5258.506		5278.967
39	B^6	4562.393		6116.252		5281.146		5340.651
40	2^13^3	4604.597		6146.192		5303.949		5371.979
41	$cis\,4^2$	4631.747		6191.554		5347.931		5393.805
42	3^34^2	4641.684		6198.328		5358.627		5506.149
43	B^6	4675.332		6238.396		5392.043		5528.228
44	$cis\,3^16^2$	4739.798		6284.169		5512.369		5560.690
45	$^d2^23^2$	4876.914		6346.790		5552.030		5569.917
46	B^6	4888.964		6365.483		5575.132		5645.486
47	$^d3^2B^4$	4899.278		6395.413		5591.149		5733.545
48	$^d2^13^2B^2$	4941.710		6419.677		5641.904		5741.453
49	$^d2^13^2B^2$	4985.308		6513.885		5696.065		5755.534
50	3^2B^4	5048.903		6521.398		5721.317		5826.315

Bibliography

[1] V. Henri and M. Landau, "Absorption of Ultra-violet Light by Acetylene," *Comptes Rendus*, vol. 156, p. 697, 1913.

[2] Stark and Lipp, "Die ultravioletten Absorptionsbanden der wechselseitigen Bindung von Kohlenstoffatomen. 2. Azetylenbindung," *Zeit. f. phys. Chem.*, vol. 86, p. 36, 1913.

[3] G. B. Kistiakowsky, "On the Ultraviolet Absorption Spectrum of Acetylene," *Phys. Rev.*, vol. 37, p. 276, 1931.

[4] M. A. Ionesco *Comptes Rendus*, vol. 199, p. 710, 1934.

[5] M. A. Ionesco, "Sur la structure des bandes d'absorption de l'acetylene dans l'ultraviolet," *Comptes Rendus*, vol. 200, p. 817, 1935.

[6] H. Hese, A. Rose, and R. Gräfin Zu Dohna, "Untersuchungen im Schumanngebiet," *Zeit. f. Phys.*, vol. 81, p. 745, 1933.

[7] S.-C. Woo, T.-K. Liu, T. C. Chu, and W. Chih, "The Near Ultraviolet Bands of Acetylene," *J. Chem. Phys.*, vol. 6, p. 240, 1938.

[8] K. K. Innes, "Analysis of the Near Ultraviolet Absorption Spectrum of Acetylene," *J. Chem. Phys.*, vol. 22, p. 863, 1954.

[9] C. K. Ingold and G. W. King, "Excited States of Acetylene," *J. Chem. Soc.*, vol. 1953, p. 2702, 1953.

[10] J. K. G. Watson, M. Herman, J. C. V. Craen, and R. Colin, "The $\tilde{A} - \tilde{X}$ Band System of Acetylene," *J. Mol. Spectrosc.*, vol. 95, pp. 101–132, 1982.

[11] J. C. Van Craen, M. Herman, R. Colin, and J. K. G. Watson, "The $\tilde{A} - \tilde{X}$ Band System of Acetylene," *J. Mol. Spectrosc.*, vol. 111, pp. 185–197, 1985.

[12] J. C. Van Craen, M. Herman, R. Colin, and J. K. G. Watson, "The $\tilde{A} - \tilde{X}$ Band System of Acetylene," *J. Mol. Spectrosc.*, vol. 119, pp. 137–143, 1986.

[13] J. D. Tobiason, A. L. Utz, and F. F. Crim, "The direct observation, assignment, and partial deperturbation of ν_5 and $\nu_3 + \nu_5$ in ^1A_u acetylene (C2H2)," *J. Chem. Phys.*, vol. 99, p. 928, 1993.

[14] A. L. Utz, J. D. Tobiason, E. C. M., L. J. Sanders, and F. F. Crim, "The direct observation, assignment, and partial deperturbation of the ν_4 and ν_6 vibrational fundamentals in ^1A_u acetylene (C_2H_2)," *J. Chem. Phys.*, vol. 98, p. 2742, 1993.

[15] A. H. Steeves, A. J. Merer, H. A. Bechtel, A. R. Beck, and R. W. Field, "Direct observation of the symmetric stretching modes of $\tilde{A}^1A_u$ acetylene by pulsed supersonic jet laser induced fluorescence," *Mol. Phys.*, vol. 106, p. 1867, 2008.

[16] J. H. Baraban, J. Stanton, A. J. Merer, and R. W. Field, "Anharmonic force fields of cis- and trans-S_1 C_2H_2," *Mol. Phys.*, vol. 110, p. 2725, 2012.

[17] A. J. Merer, A. H. Steeves, J. H. Baraban, H. A. Bechtel, and R. W. Field, "Cis-trans isomerization in the S_1 state of acetylene: Identification of cis-well vibrational levels," *J. Chem. Phys.*, vol. 134, p. 244310, 2011.

[18] J. H. Baraban, P. B. Changala, A. J. Merer, A. H. Steeves, H. A. Bechtel, and R. W. Field, "The $\tilde{A}^1A_u$ state of acetylene: ungerade vibrational levels in the region 45,800-46,550 cm^{-1}," *Mol. Phys.*, vol. 110, p. 2707, 2012.

[19] B. T. Darling and D. M. Dennison, "The Water Vapor Molecule," *Phys. Rev.*, vol. 57, p. 128, 1940.

[20] A. J. Merer, N. Yamakita, S. Tsuchiya, A. H. Steeves, H. A. Bechtel, and R. W. Field, "Darling-Dennison resonance and Coriolis coupling in the bending overtones of the $\tilde{A}^1A_u$ state of acetylene, C_2H_2," *J. Chem. Phys.*, vol. 129, p. 054304, 2008.

[21] A. H. Steeves, H. A. Bechtel, A. J. Merer, N. Yamakita, S. Tsuchiya, and R. W. Field, "Stretch-bend combination polyads in the $\tilde{A}^1A_u$ state of acetylene, C_2H_2," *J. Mol. Spectrosc.*, vol. 256, pp. 256–278, 2009.

[22] J. H. Baraban, A. R. Beck, A. H. Steeves, J. F. Stanton, and R. W. Field, "Reduced dimension discrete variable representation study of *cis-trans* isomerization in the S_1 state of C_2H_2," *J. Chem. Phys.*, vol. 134, p. 244311, 2011.

[23] W. J. Lafferty and A. S. Pine, "Spectroscopic Constants for the 2.5 and 3.0 μm Bands of Acetylene," *J. Mol. Spectrosc.*, vol. 141, pp. 223–230, 1990.

[24] M. Mizoguchi, N. Yamakita, S. Tsuchiya, A. Iwasaki, K. Hoshina, and K. Yamanouchi, "IR-UV Double Resonance Spectroscopy of Acetylene in the $\tilde{A}^1A_u$ $n\nu_3' + \nu_4'$ and $n\nu_3' + \nu_6'(n = 2, 3)$ *Ungerade* Vibrational States," *J. Phys. Chem. A*, vol. 104, pp. 10212–10219, 2000.

[25] N. Yamakita and S. Tsuchiya, "Zeeman quantum beat observed by IR-UV double resonance LIF spectroscopy of acetylene in the $\tilde{A}^1A_u$ $3\nu_3' + \nu_6'$ and $3\nu_3' + \nu_4'$ *ungerade* vibrational states," *Chem. Phys. Lett.*, vol. 348, p. 53, 2001.

[26] J. T. Hougen, "Multi-valued versus single-valued large-amplitude bending-torsional-rotational coordinate systems for simultaneously treating trans-bent and cis-bent acetylene in its S_1 state," *J. Mol. Spectrosc.*, vol. 278, pp. 41–51, 2012.

[27] P. R. Bunker and P. Jensen, *Molecular Symmetry and Spectroscopy.* NRC Research Press, Ottawa, Ontario, Canada, 2nd ed., 2006.

[28] J. T. Hougen, "Strategies for advanced applications of permutation-inversion groups to the microwave spectra of molecules with large amplitude motions," *Journal of Molecular Spectroscopy*, vol. 256, pp. 170 185, 2009.

[29] E. U. Condon and G. Shortley, *The Theory of Atomic Spectra.* Cambridge University Press, Cambridge, England, 1951.

[30] S. C. Wang, "On The Asymmetrical Top in Quantum Mechanics," *Phys. Rev.*, vol. 34, p. 243, 1929.

[31] A. J. Merer and J. K. G. Watson, "Symmetry Considerations for Internal Rotation in Ethylene-like Molecules," *J. Mol. Spectrosc.*, vol. 47, p. 499, 1973.

[32] J.F. Stanton, J. Gauss, M.E. Harding, P.G. Szalay with contributions from A.A. Auer, R.J. Bartlett, U. Benedikt, C. Berger, D.E. Bernholdt, Y.J. Bomble, L. Cheng, O. Christiansen, M. Heckert, O. Heun, C. Huber, T.-C. Jagau, D. Jonsson, J. Jusélius, K. Klein, W.J. Lauderdale, D.A. Matthews, T. Metzroth, L.A. Mck, D.P. O'Neill, D.R. Price, E. Prochnow, C. Puzzarini, K. Ruud, F. Schiffmann, W. Schwalbach, S. Stopkowicz, A. Tajti, J. Vázquez, F. Wang, J.D. Watts and the integral packages MOLECULE (J. Almlöf and P.R. Taylor), PROPS (P.R. Taylor), ABACUS (T. Helgaker, H.J. Aa. Jensen, P. Jørgensen, and J. Olsen), and ECP routines by A. V. Mitin and C. van Wüllen. For the current version, see http://www.cfour.de.

[33] M. Galassi et al, GNU Scientific Library Reference Manual (3rd Ed.), ISBN 0954612078. See http://www. gnu.org/software/gsl/.

[34] S. Carter and N. C. Handy, "The Variational Method for the Calculation of Ro-Vibrational Energy Levels," *Computer Physics Reports*, vol. 5, pp. 115–172, 1986.

[35] M. J. Bramley, W. H. Green, Jr., and N. C. Handy, "Vibration-rotation coordinates and kinetic energy operators for polyatomic molecules," *Mol. Phys.*, vol. 73, p. 1183, 1991.

[36] E. B. Wilson, Jr., J. C. Decius, and P. C. Cross, *Molecular Vibrations: The Theory of Infrared and Raman Vibrational Spectra.* Dover, New York, 1980.

[37] J. H. Frederick and C. Woywod, "General formulation of the vibrational kinetic energy operator in internal bond-angle coordinates," *J. Chem. Phys.*, vol. 111, p. 7255, 1999.

[38] X. Chapuisat, A. Nauts, and J.-P. Brunet, "Exact quantum molecular Hamiltonians: Part I. Application to the dynamics of three particles," *Mol. Phys.*, vol. 72, pp. 1–31, 1991.

[39] X. Chapuisat, A. Belafhal, and A. Nauts, "N-Body Quantum-Mechanical Hamiltonians: Extrapotential Terms," *J. Mol. Spectrosc.*, vol. 149, p. 274, 1991.

[40] M. Menou and X. Chapsuisat, "Quantum-Mechanical Hamiltonians for Constrained Systems: Application to Four-Body Systems," *J. Mol. Spectrosc.*, vol. 159, pp. 300–328, 1993.

[41] F. Gatti, Y. Justum, M. Menou, A. Nauts, and X. Chapsuisat, "Quantum-Mechanical Description of Rigidly or Adiabatically Constrained Molecular Systems," *J. Mol. Spectrosc.*, vol. 181, pp. 403–423, 1997.

[42] M. J. Bramley and N. C. Handy, "Efficient calculation of rovibrational eigenstates of sequentially bonded four atom molecules," *J. Chem. Phys.*, vol. 98, p. 1378, 1993.

[43] M. Silva, R. Jongma, R. W. Field, and A. M. Wodtke, "The Dynamics of 'Stretched Molecules': Experimental Studies of Highly Vibrationally Excited Molecules with Stimulated Emission Pumping," *Ann. Rev. Phys. Chem.*, vol. 52, p. 811, 2001.

[44] S. A. B. Solina, J. P. O'Brien, R. W. Field, and W. F. Polik, "Dispersed Fluorescence Spectrumo of Acetylene from the $\tilde{A}^1A_u$ Origin: Recognition of Polyads and Test of Multiresonant Effective Hamiltonian Model for the $\tilde{X}$ State," *J. Phys. Chem.*, vol. 100, p. 7797, 1996.

[45] J. P. O'Brien, M. P. Jacobson, J. J. Sokol, S. L. Coy, and R. W. Field, "Numerical Pattern Recognition Analysis of Acetylene Dispersed Fluorescence Spectra," *J. Chem. Phys.*, vol. 108, p. 7100, 1998.

[46] K. Hoshina, A. Iwasaki, K. Yamanouchi, M. P. Jacobson, and R. W. Field, "The IR-UV Dispersed Fluorescence Spectrum of Acetylene: New Classes of Bright States," *J. Chem. Phys.*, vol. 114, p. 7424, 2001.

[47] R. N. Dixon, "Higher vibrational levels of a bent triatomic molecule," *Trans. Faraday Soc.*, vol. 60, pp. 1363–1368, 1964.

[48] H. A. Bechtel, A. H. Steeves, B. M. Wong, and R. W. Field, "Evolution of Chemical Bonding during HCN↔HNC Isomerization as Revealed through Nuclear Quadrupole Hyperfine Structure," *Angew. Chem. Int. Ed.*, vol. 47, pp. 2969–2972, 2008.

[49] M. Herman, A. Campargue, M. I. E. Idrissi, and J. V. Auwera, "Vibrational Spectroscopic Database on Acetylene, $\tilde{X}^1\Sigma_g^+$ ($^{12}C_2H_2$, $^{12}C_2D_2$, and $^{13}C_2H_2$)," *J. Phys. Chem. Ref. Data*, vol. 32(3), p. 921, 2003.

[50] D. H. Mordaunt and M. N. R. Ashfold, "Near ultraviolet photolysis of C_2H_2: A precise determination of D_0(HCC−H)," *J. Chem. Phys.*, vol. 101, p. 2630, 1994.

[51] D. H. Mordaunt, M. N. R. Ashfold, R. N. Dixon, P. Löffler, L. Schnieder, and K. H. Welge, "Near threshold photodissociation of acetylene," *J. Chem. Phys.*, vol. 108, p. 519, 1998.

[52] T. Suzuki and N. Hashimoto, "Predissociation of acetylene from the ^1A_u state studied by absorption, laser-induced fluorescence, and H-atom action spectroscopies," *J. Chem. Phys.*, vol. 110, p. 2042, 1999.

[53] A. T. J. B. Eppink and D. H. Parker, "Velocity map imaging of ions and electrons using electrostatic lenses: Application in photoelectron and photofragment ion imaging of molecular oxygen," *Rev. Sci. Instrum.*, vol. 68, p. 3477, 1997.

[54] N. Yamakita, S. Iwamoto, and S. Tsuchiya, "Predissociation of Excited Acetylene in the $\tilde{A}^1A_u$ State around the Adiabatic Dissociation Threshold as Studied by LIF and H-Atom Action Spectroscopy," *J. Phys. Chem. A*, vol. 107, p. 2597, 2003.

[55] T. Suzuki, Y. Shi, and H. Kohguchi, "Detection of metastable triplet acetylene produced by intersystem crossing from the excited (^1A_u) state," *J. Chem. Phys.*, vol. 106, p. 5292, 1997.